UNIVERSITY OF CALIFORNIA SAN DIEGO

The Broadband, Multi-scale Vorticity Wake Generated by flow past Palau

A dissertation submitted in partial satisfaction of the
requirements for the degree
Doctor of Philosophy

in

Oceanography

by

Kristin L. Zeiden

Committee in charge:

Professor Jennifer MacKinnon, Co-Chair
Professor Daniel Rudnick, Co-Chair
Professor Matthew Alford
Professor Mark Merrifield
Professor Geno Pawlak

2021

The dissertation of Kristin L. Zeiden is approved, and it is acceptable in quality and form for publication on microfilm and electronically:

_____

_____

_____

_____
Co-Chair

_____
Co-Chair

University of California San Diego

2021

DEDICATION

To my Nanna, Portia McKenna,

She will forever hold a special place in my heart. She was quick-witted, determined, educated, compassionate, dedicated to her family, and most importantly ... incredibly posh!

You left us too soon and we miss you every day.

TABLE OF CONTENTS

Signature Page . . . iii

Dedication . . . iv

Table of Contents . . . v

List of Figures . . . viii

Acknowledgements . . . xi

Vita . . . xiv

Abstract of the Dissertation . . . xv

Chapter 1 Introduction . . . 1

Chapter 2 Glider Observations of a Mesoscale Oceanic Island Wake . . . 5
2.1 Introduction . . . 6
2.2 Data and Methods . . . 9
2.2.1 Oceanographic Setting . . . 9
2.2.2 Dataset Description . . . 10
2.2.3 Objective Map . . . 11
2.2.4 Eastward and Westward Flow Definitions . . . 13
2.2.5 OSCAR Surface Currents . . . 14
2.3 Results . . . 14
2.3.1 Mean Currents and Variability . . . 14
2.3.2 Westward Flow . . . 15
2.3.3 Eastward Flow . . . 17
2.3.4 Vorticity . . . 18
2.3.5 Event Driven Variability . . . 19
2.4 Discussion . . . 20
2.4.1 Rossby Number . . . 21
2.4.2 Shedding Frequency . . . 22
2.4.3 Depth Dependence . . . 23
2.4.4 Eddy Viscosity . . . 24
2.4.5 Regional context . . . 25
2.5 Conclusion . . . 26
2.6 Acknowledgments . . . 28

Chapter 3 Broadband Submesoscale Vorticity Generated by Flow Around an Island . 45
3.1 Introduction . . . 46
3.2 Data and Methods . . . 49
3.2.1 Oceanographic Setting . . . 49
3.2.2 Dataset Description . . . 50
3.2.3 Vorticity Calculation . . . 52
3.2.4 Empirical Orthogonal Function Analysis . . . 53
3.3 Results . . . 54
3.3.1 Broad-band Currents around Palau . . . 54
3.3.2 Submesoscale Vorticity Timeseries . . . 58
3.3.3 Dominant Statistical Modes . . . 59
3.3.4 Non-stationary Vorticity Variance . . . 60
3.4 Discussion . . . 63
3.4.1 Non-linear Broadband Eddy Formation . . . 64
3.4.2 Internal Waves and Vorticity Variance . . . 66
3.4.3 Implications for the Palau Wake . . . 67
3.5 Conclusion . . . 68
3.6 Acknowledgments . . . 70

Chapter 4 Lagrangian Observations of the Palau Wake . . . 82
4.1 Introduction . . . 83
4.2 Data and Methods . . . 86
4.2.1 Oceanographic Context . . . 86
4.2.2 Dataset Description . . . 87
4.2.3 Vorticity from Least-Squares Fit to Velocity . . . 89
4.2.4 Angular Frequency from Rotary Wavelet Transformations of Velocity . . . 91
4.2.5 Scale and Diffusivity . . . 92
4.3 Results . . . 93
4.3.1 Vorticity Timeseries . . . 93
4.3.2 Velocity Scalograms . . . 95
4.3.3 Average Wake Vorticity . . . 96
4.3.4 Drifter Dispersion . . . 98
4.4 Discussion . . . 98
4.4.1 Eddy Scale . . . 99
4.4.2 Dynamic balance . . . 102
4.4.3 Downstream Dispersion and Eddy Evolution . . . 104
4.4.4 Relationship to Incident Flow . . . 105
4.5 Summary . . . 107
4.6 Acknowledgments . . . 108

Chapter 5 Conclusion . . . 126

References 129

LIST OF FIGURES

Figure 2.1: OSCAR surface currents (vectors) averaged over the glider observation period and shaded by zonal velocity. 29
Figure 2.2: Glider dives are plotted in white over the local bathymetry. Gliders sampled between 7.75° and 9° N, along 134.25° (Line W) and 135° E (Line E). . . . 30
Figure 2.3: Example glider section along Line E, completed between November 24 and December 2, 2015. 31
Figure 2.4: Autocorrelation of zonal velocity as a function of lag in latitude and time, calculated at each 10 m depth bin and averaged over the water column for Line W (a) and Line E (b). 32
Figure 2.5: Example objectively mapped glider section along Line E, corresponding to Nov 29, 2015. 33
Figure 2.6: Time series of depth-averaged velocity vectors for each section, shaded by the depth-latitude average zonal velocity across each section. 34
Figure 2.7: Mean sections of zonal (a,b) and meridional (c,d) velocity along Line E (b,d) and Line W (a,c), as well as mean depth-average velocity vectors plotted against bathymetry (e). 34
Figure 2.8: Zonal (a,b) and meridional (c,d) velocity variability (standard deviation) along Line W (a,c) and Line E (b,d). 35
Figure 2.9: Mean sections of zonal (a,b) and meridional (c,d) velocity along Line E (b,d) and Line W (a,c) after selecting for westward flow. 36
Figure 2.10: Time-mean depth-average velocity vectors in intervals of 100 m along Line E (a) and Line W (b), after selecting for westward flow. 37
Figure 2.11: Zonal (a,b) and meridional (c,d) velocity variability along Line W (a,c) and Line E (b,d) after selecting for westward flow. 38
Figure 2.12: Mean sections of zonal (a,b) and meridional (c,d) velocity along Line E (b,d) and Line W (a,c) after selecting for eastward flow. Line W is upstream during westward flow, and Line E is downstream. 39
Figure 2.13: Time-mean depth-average velocity vectors in intervals of 100 m along Line E (a) and Line W (b), after selecting for eastward flow. 40
Figure 2.14: Mean sections of normalized vorticity (Rossby number, Ro) calculated from the meridional gradient of zonal velocity ($\zeta = dU/dy$), during westward flow (a,b) and eastward flow (c,d) along Line W (a,c) and Line E (b,d). 41
Figure 2.15: Hovmoller diagrams of shallow (0 - 100 m) zonal velocity along Line E (a) and Line W (b). 42
Figure 2.16: Hovmoller diagrams of shallow (0 - 100 m) normalized vorticity (Rossby number) along Line E (a) and Line W (b). 42
Figure 2.17: Depth-average, section integrated vorticity flux (ζU) along both lines (a), as well as depth-and-latitude average zonal velocity north of 8.2° N along Line E (b). 43

Figure 2.18: OSCAR surface currents averaged over the observational periods corresponding to westward (a,c) and eastward flow (b,d) provide regional context for the asymmetries observed by the glider during flow reversals. 44

Figure 3.1: Mooring locations plotted over regional (a) and local (b),(c) bathymetry. Insets (b),(c) are marked in (a),(b) respectively with dashed black lines. . . 71
Figure 3.2: Example section of (a) zonal and (b) meridional velocity from 0-1400 m at F3 during a strong westward sub-inertial surface current event from November 15, 2016 to January 1, 2017 72
Figure 3.3: Surface (0-100 m depth-averaged) zonal (blue lines) and meridional (red lines) velocity timeseries at M2, M5, F3, F1 and M1 (counterclockwise around the reef). 73
Figure 3.4: As in Fig. 3.3, but for the subsurface (300-400 m depth-averaged). 74
Figure 3.5: Surface (a) and subsurface (b) kinetic energy spectra at F2 (green), F3 (red) and F4 (blue) are red, with strong peaks in the inertial, diurnal and semi-diurnal bands. 75
Figure 3.6: Timeseries of array-mean surface (a) zonal velocity, (b) meridional velocity, (c) kinetic energy and (d) vorticity. 76
Figure 3.7: As in Fig. 3.6, but in the subsurface (300 – 400m). Note the changes in vertical axes from Fig. 3.6. Unlike surface velocities, at depth the current is often dominated by high-frequency variance. 76
Figure 3.8: Empirical orthogonal functions of velocity in the (a) surface layer (0-100 m) and (b) subsurface layer (300-400 m). 77
Figure 3.9: Timeseries of (a),(b) surface and (c),(d) subsurface vorticity calculated using velocity from (a),(c) EOFs characterized by lateral shear and (b),(d) EOFs characterized by eddy motion. 78
Figure 3.10: Timeseries of surface (a) sub-inertial velocity at all three moorings and (b) vorticity, along with (c) the scalogram of vorticity gives time variability of its frequency content. 79
Figure 3.11: As in Fig. 3.10, but for the subsurface layer. High-frequency vorticity variance increases dramatically in September and October during a sub-inertial current event characterized by strong shear. 80
Figure 3.12: An example of surface velocity during (a) flood and (b) ebb tide during strong westward flow. 81

Figure 4.1: Regional bathymetry overlaid with (a) mean OSCAR surface currents over the observational period (October 2016 - December 2018) and (b) drifter trajectories over the first 20 days of each release period. 109
Figure 4.2: Mean OSCAR surface currents averaged over the first 20 deployment days of (a,b) C7 (March 2017) and (c,d) C5 (November 2016). 110
Figure 4.3: (a) MODIS sea-surface temperature averaged over the first 8 days of C7 and (b) vorticity from OSCAR surface currents averaged over the same period. 111

Figure 4.4: Vorticity, KE and scale for C5. (a) Vorticity is estimated using two least-squares fits to the velocity data: (1) fitting a plane to the velocity of each drifter at each time step (blue lines) and (2) fitting solid-body rotation (magenta lines). 112
Figure 4.5: As in Fig. 4, but for C7. 113
Figure 4.6: Example rotary wavelet scalogram for Drifter 5 in C7, showing (a) anticyclonic rotation and (b) cyclonic rotation. 114
Figure 4.7: Cyclonic rotary wavelets for (a-e) all drifters in C7 as well as (f) their average. 115
Figure 4.8: As in Fig. 5, but for C5. 116
Figure 4.9: Averages of (a) vorticity, (b) kinetic energy and (c) cluster scale taken over all drifter clusters which were advected westward. 117
Figure 4.10: Enstrophy (vorticity squared) from all westward clusters binned by wavenumber (inverse scale). 118
Figure 4.11: As in Fig. 6, but averaged over every drifter cluster which was initially advected westward. 119
Figure 4.12: Cluster scale $L(t)$ for each cluster advected westward. 120
Figure 4.13: Diffusivity (rate-of-change of L^2) from all westward clusters binned by wavenumber ($k = L^{-1}$). 121
Figure 4.14: (a) Azimuthal velocity for two eddy models, a Rankine vortex (solid body plus irrotational core) (blue line), and a line vortex smoothed by friction (red line). (b) Corresponding vorticity (solid lines) and angular frequency (dashed lines) for each model. 122
Figure 4.15: (a) Probability density function of number of observations binned by eddy azimuthal velocity (U_e) and translation speed (U_c). The ratio of these values gives a non-linearity parameter which indicates whether eddies are likely to exchange fluid with the exterior region (yes if $U_e/U_c < 1$). 123
Figure 4.16: (a) Initial wake vorticity (0-5 days) for each cluster advected westward, (b) initial OSCAR surface currents at the north end, (c) east side and (d) south end of Palau during each release. 124
Figure 4.17: OSCAR Surface currents averaged over the first 20 deployment days of each drifter cluster entrained into (a,c) wake eddies and (b,d) free shear layers. . 125

ACKNOWLEDGEMENTS

I'd like to thank my advisors, Dan Rudnick and Jen MacKinnon, for their unwavering patience and encouragement over the past five years. Perhaps more importantly, thank you for challenging me along the way. It was a privilege to learn from two talented scientists who are also gifted teachers and mentors. I cannot imagine better advisors. Thank you also to my committee members, Drs. Matthew Alford, Mark Merrifield and Geno Pawlak for their time, insights, thoughtful feedback and support in generating this work. Thank you also to Dr. Janet Sprintall, for her mentorship during my first summer at SIO.

This thesis work would not have been possible without observational data collected by the Instrument Development Group, the Multiscale Ocean Dynamics group and the Lagrangian Drifter Lab at Scripps, as well as the Coastal Oceanographic Research and Analysis Lab at the University of Hawaii. The Instrument Development Group was responsible for the Spray glider operations, the Multiscale Ocean Dynamics group and Coastal Oceanographic lab for mooring deployments, and the Lagrangian Drifter lab for the Surface Velocity Program drifters. Thank you to the large group of talented engineers for their dedication and expertise, both in the labs and at sea. Thank you also to the principle investigators who allowed me to analyze data they worked hard to secure funding for and collect, Drs. Matthew Alford, Gunnar Voet, Hemantha Wijesekera, Mark Merrifield, Luca Centurioni and Verena Hormann. Additional thanks to Derek Vana, who allowed me to tag along on a glider deployment in Palau, as well as Martha Schonau and Kasia Zaba, for providing great mentorship as senior graduate students in the IDG lab.

Thanks to Drs. Hemantha Wijesekera and David Wang at the Naval Research Laboratory (NRL) at the Stennis Space Center, MS, for allowing me to spend a summer with them exploring Navy research and broadening my exposure to different physical oceanography questions. And special thanks to the Office of Naval Research, which funded this work and my salary through grants obtained by my advisors, and through my research internship at NRL. Thank you again to my advisors for supporting my sojourn at NRL, and for encouraging me to pursue my interest

with the Navy.

Thank you to my classmates and cohort at SIO, and the broader SIO community. Thanks to Andre Paloczy and Manuel Gutierrez for allowing me to frequently drag them down with me in classes, only to pull me back up again. Thank you to my office mates Maddie Hamann, Celia Ou, Noel Brizuela and Alice Ren for tolerating my coffee habit and random questions. And thank you to Camille Pagniello and Kelley McBride for braving student council with me. Extra special thanks to Mika Siegelman and Conrad Luecke, for finding me on a quiet ship in the tropical North Pacific and transforming my graduate experience. It would not have been the same without you two. I don't make friends quickly, so now you're stuck with me for the long haul.

And thank you to my best friends of many, many years, Eva, Keito, Marie, Caitlin, Kerry, Sami, Brittany, Jenni, Sprouse, and Lindsay. You have all been like sisters to me, starting in Kindergarten and through graduate school. You're also stuck with me!

Thanks to my brothers, Kevin and Scott, for supporting their sometimes scary big sister. Thank you to all my grandparents, who provided second homes to me while I was at UCLA. Thank you to my godparents, Drs. Renee and Chris Glass for supporting me in all my pursuits and providing council over the years. And extra special thanks to my parents, to whom I am indebted for all things I have accomplished in my life. I deserve little-to-no credit for these feats, and would have been lost without your unconditional love, guidance, support and nagging (yes Mom, even the nagging). I am not an original person, but rather an amalgamation of you. I hope I can live up to the example you have set.

Finally, I cannot begin to express my thanks to my rock, my husband, Edward. I am humbled by your commitment, and the sacrifices you so readily have made for me. Thank you for making my dreams your dreams, and for your patience. Thank you for being the steady one, the visionary, the hopeful one. Thank you for believing in me more than I believe in myself. I only hope I will have the opportunity in our long life together to return the favor.

Chapter 2, in full, is a reprint of the material as it appears in Zeiden, K.L, D.L. Rudnick and J.A. MacKinnon (2019). Glider Observations of a Mesoscale Oceanic Island Wake. Journal of Physical Oceanography, 49, 2217– 2235, doi: 10.1175/JPO-D-18-0233.1. Used with permission from ©American Meteorological Society. The dissertation author was the primary investigator and author of this paper.

Chapter 3, in full, is a reprint of the material as it appears in Zeiden, K.L., J.A. MacKinnon, D.L. Rudnick, M.H. Alford, H. Wijesekera and G. Voet (2021). Broadband Submesoscale Vorticity Generated by Flow Around an Island. doi:10.1175/JPO-D-20-0161.1. Used with permission from ©American Meteorological Society. The dissertation author was the primary investigator and author of this paper.

Chapter 4, in full, consists of material that is being prepared for submission for publication in the Journal of Physical Oceanography, Zeiden, K.L., D.L. Rudnick, J.A. MacKinnon, V. Hormann and L. Centurioni (In Preparation) Lagrangian Observations of the Palau Wake. The dissertation author was the primary investigator and author of this paper.

VITA

2011 B. S. in Astrophysics, University of California, Los Angeles

2021 Ph. D. in Oceanography, University of California San Diego

PUBLICATIONS

Zeiden, K.L., D.L. Rudnick, J.A. MacKinnon, V. Hormann and L. Centurioni "Lagrangian Observations of the Palau Wake", In preparation for *Journal of Physical Oceanography*

Zeiden, K.L., J.A. MacKinnon, D.L. Rudnick, M.H. Alford, H. Wijesekera and G. Voet (In Revision) "Broadband Sumesoscale Vorticity Generated by Flow Around an Island", *Journal of Physical Oceanography*.

Zeiden, K.L., D.L. Rudnick and J.A. MacKinnon (2019) "Glider Observations of a Mesoscale Oceanic Island Wake", *Journal of Physical Oceanography*, doi: 10.1175/jpo-d-18-0233.1.

Andres, M., R. Musgrave, D.L. Rudnick, **K.L. Zeiden**, T. Peacock, and J.H. Park (2020): "On the predictability of sea surface height around Palau". *Journal of Physical Oceanography*. doi:10.1175/JPO-D-19-0310

Rudnick, D. L., **K.L. Zeiden**, C. Ou, T.M. Johnston, J.A. MacKinnon, M.H. Alford, and G. Voet (2019): "Understanding Vorticity Caused by Flow Passing an Island". *Oceanography*. 32, 4: 66 – 73, doi:10.5670/oceanog.2019.412

Siegelman, M., M. Merrifield, E. Firing, J.A. Mackinnon, M.H. Alford, G. Voet, H.W. Wijesekera, **K.L. Zeiden**, and E. Terrill. (2019) "Observations of Near-inertial Surface Currents at Palau". *Oceanography*. 32, 4: 74-83, doi:10.5670/oceanog.2019.413.

MacKinnon, J.A., M.H. Alford, G. Voet, **K.L. Zeiden**, T.M Shaun Johnston, M. Siegelman, S. Merrifield, and M. Merrifield (2019). "Eddy Wake Generation from Broadband Currents Near Pala". *Journal of Geophysical Research, Oceans*, doi: 10.1029/2019JC014945.

ABSTRACT OF THE DISSERTATION

The Broadband, Multi-scale Vorticity Wake Generated by flow past Palau

by

Kristin L. Zeiden

Doctor of Philosophy in Oceanography

University of California San Diego, 2021

Professor Jennifer MacKinnon, Co-Chair
Professor Daniel Rudnick, Co-Chair

Island wakes often have a significant influence on regional current variability and they can be a strong source of vorticity far from the boundaries of major ocean basins. Historically they have been difficult to characterize due to the wide range of flow scales which contribute to their variance. In this thesis work, observations from gliders, moorings, and surface drifters are combined to investigate the vorticity wake behind Palau, a $\sim$200 km long island in the deep tropical North Pacific.

First, the island-scale ($>$30 km) flow is characterized using velocity data obtained with underwater gliders which profiled along two parallel meridional sections upstream and down-

stream of the island. On average, westward flow is topographically blocked, accelerates around the island, and there is recirculation in the lee with vertical vorticity up to $0.3f$. Here f is the local Coriolis frequency. However, vorticity variance is high and instantaneous values can exceed f when the incident flow is strongest.

Then, a triangular array of moorings (7 km) deployed within a few km of the north end of the island is used to capture submesoscale vorticity as it is injected into the wake. At this scale, vorticity can exceed $6f$ during strong westward flow. This vorticity is associated with the formation of strong wake eddies. We find that tidal and inertial currents heavily modulate the frequency of eddy formation, even during strong low-frequency flow.

Finally, vorticity downstream of Palau is investigated with clusters of surface drifters deployed in the same location as the mooring array. Drifters were often entrained in submesoscale wake eddies with vorticity up to $6f$, consistent with observations from the moorings. Outside the eddy cores, vorticity is inversely proportional to cluster scale and we conclude the growth of wake eddies is controlled by large-scale shear in the regional currents.

Chapter 1

Introduction

The generation of wakes behind topographic features, such as headlands, islands and seamounts, is of general interest to the oceanographic community due to the potential for significant kinematic changes to the incident flow. Broadly, these include momentum loss due to the drag induced by viscous and pressure forces, outwards momentum flux via the generation of internal waves, and the generation of vorticity. 'Vorticity wakes' occur when the latter is the dominant response. In most geophysical vorticity wakes, coherent structures known as eddies are formed leeward which dominate the current variability downstream. Wake eddies may contribute to increased vertical mixing and lateral stirring, transport isolated water masses far from their generation source, modulate the propagation of internal waves, and catalyze momentum transfer between large-scale flows. The focus of this thesis is the generation of a vorticity wake by flow around the island Palau, located in the tropical North Pacific. Data from moorings, underwater gliders, surface drifters and satellite data collected between 2015 and 2019 are used to calculate vorticity around the island over a broad range of spatial and temporal scales, using a variety of methodologies.

A fundamental understanding of vorticity wakes has come from extensive study of the idealized model of homogeneous steady flow past a cylinder (Zdravkovich, 2000). Vorticity

is generated in the boundary layer due to the viscous no-slip condition at its surface. An adverse pressure gradient along the downstream side of the cylinder forces the incident flow to separate. Return flow in the lee develops to satisfy continuity, also fed by vorticity from the detached boundary layer. Two identical, counter-rotating eddies form and remain attached until perturbations in the flow causes one of the eddies to separate. Afterwards, eddies shed at a natural frequency dictated by the strength of flow and scale of the cylinder. Observational studies have shown that real island wakes are often well explained by this simple model (Barkley, 1972; Bowman et al., 1996; Heywood et al., 1990; Sangra et al., 2007). However, geophysical forcing introduces additional variability. For example, sloping boundaries and shallow bottoms can also produce torque (Wolanski et al., 1984; Pattiaratchi et al., 1986). Oscillatory currents may modify the period of eddy formation and separation (Callendar et al., 2011; Neill and Elliott, 2004; Wolanski et al., 1984). Downstream, the earth's rotation can introduce asymmetries between cyclonic and anticyclonic eddies (Caldeira and Sangra, 2012a; Dong et al., 2007).

The goal of this thesis is to understand the physical mechanisms governing the generation of vorticity, the formation of wake eddies and their downstream evolution around Palau. Therefore, calculating vorticity is a central focus of each study. Estimating spatial gradients from coarse observations is a long-standing challenge in the field because real geophysical flows are broadband in space and time (Bretherton et al., 1976; Davies-Jones, 1993; Okubo and Ebbesmeyer, 1976; Lilly et al., 2011). High resolution spatial (i.e., 'synoptic') sampling can provide valuable detail about isolated wake structures, but it is difficult to ascertain whether such observations are representative of the mean. To address this problem, this thesis work combines sustained observations of currents around Palau from different instruments with a wide range of temporal and spatial resolutions. Each measurement technique facilities the calculation of vorticity using a different methodology. These fall into two main categories, (1) the calculation of velocity spatial gradients at fixed times and (2) spectral analysis of velocity timeseries. The first is a direct measurement, as the vorticity is given by $\zeta = \nabla \times \vec{u}$. The second is an indirect measurement

where periodicity in the currents is used to estimate the vorticity of wake eddies. Additional analysis methods are used to minimize the impact of aliasing the different scales of motion into each vorticity estimate. These include least-squares fitting simple models of vorticity to velocity data, Empirical Orthogonal Function (EOF) Analysis to elucidate the dominant spatial modes of variability in a flow, and objective analysis in space and time to smooth unresolved fine-scale variance.

A major strength of this work is the opportunity to compare vorticity estimates across these different instruments and methods. Concurrent studies offer further comparison points. Observations utilized in this work are part of a broader Office of Naval Research field campaign, Flow Encountering Abrupt Topography (FLEAT). The goal of FLEAT is to characterize the Palau wake generally and understand the physical processes responsible for its development. Palau is a flat-topped, steep-sided $\sim$200 km meridionally elongated island in the deep ocean lying in the path of strong geostrophic surface currents. Complex topographic detail, significant regional current variability and energetic local tides mean both the incident flow and wake are highly broadband. A conclusion of this work is that each of these sources of variability has a significant impact on the structure of the wake and the generation of vorticity. For example, we find that fine-scale topographic detail often controls the lateral extent of the island-scale wake, and strong tidal currents can both increase the strength of vorticity generated and lead to the formation of submesoscale eddies at a tidal frequency. Vorticity around Palau has an inverse dependence on scale, ranging from an island scale wake with Rossby numbers O(0.1), to submesoscale eddies with Rossby numbers O(1). Here the Rossby number is the ratio of relative to planetary vorticity.

This thesis is structured as follows. In Chapter 1, two years of repeat glider sections both upstream and downstream of the island are used to characterize the mean incident island-scale flow and wake, as well as variability on timescales from weeks to months. In Chapter 2, ADCP data from an array of moorings is used to calculate submesoscale vorticity at the north end of the island in a region of anticipated flow separation on timescales of hours to months. In

Chapter 3, drifters deployed in the same location as the mooring array are used to characterize the downstream wake under a variety of incident flow conditions. Each chapter is a self-contained study, and so this thesis is presented in manuscript form. Finally, a brief conclusion connects the observations from each study and suggests further questions for investigation.

Chapter 2

Glider Observations of a Mesoscale Oceanic Island Wake

In this study, a two-year time series of velocity profiles to 1000 m from meridional glider surveys is used to characterize the wake in the lee of a large island in the western tropical North Pacific, Palau. Surveys were completed along sections to the east and west of the island to capture both upstream and downstream conditions. Objectively mapped in time and space, mean sections of velocity show the incident westward North Equatorial Current accelerating around the island of Palau, increasing from 0.1 to 0.2 m s^{-1} at the surface. Downstream of the island, elevated velocity variability and return flow in the lee are indicative of boundary layer separation. Isolating for periods of depth-average westward flow reveals a length scale in the wake that reflects local details of the topography. Eastward flow is shown to produce an asymmetric wake. Depth-average velocity time series indicate that energetic events (on timescales of weeks to months) are prevalent. These events are associated with mean vorticity values in the wake up to $0.3f$ near the surface, and instantaneous values that can exceed f during periods of sustained, anomalously strong westward flow. Thus ageostrophic effects become important to first order.

2.1 Introduction

Island wakes may be a significant sink of momentum for ocean currents and a source of vorticity in the interior, thus transforming incident currents. Islands in the path of energetic flows are often observed to have leeward flow reversals that are associated with the separation of a topographic boundary current (Heywood et al., 1990). This recirculation may detach in the form of wake eddies, which can transport trapped water mass properties and vorticity up to hundreds of kilometers downstream (Barkley, 1972; Caldeira et al., 2014). In the case of the Hawaiian Islands, the combination of wind-stress generated by the island mountains and the flow of swift geostrophic currents generates an ocean-wind wake that can extend thousands of kilometers (Xie et al., 2001). These island wakes have also been shown to impact biological processes. The domed isopycnals of cyclonic eddies can increase nutrient supply to the euphotic zone and promote biological productivity in otherwise low-productivity regions of the ocean (e.g Dickey et al., 2008; Andrade et al., 2013), and anticyclonic eddies have been shown to concentrate organic matter far downstream (Sangra et al., 2007; Aristegui and Montero, 2005). While numerous laboratory and numerical studies have addressed the physics governing wakes, oceanic observations of currents around islands are rarer. The observational challenge lies in the temporal and spatial variability of flow past islands. In this study, two years of sustained glider observations (Rudnick and Cole, 2011) provide the mean current patterns and their variability around the island of Palau in the tropical north pacific on horizontal scales of 10 – 100 km, vertical scales of 10 m, and temporal scales as short as a week.

For flows with rotation, a reasonable measure of eddy intensity is the Rossby number, here defined as the ratio of relative to planetary vorticity, $\mathrm{Ro} = \zeta/f$. Here Ro is a signed quantity, as used in e.g. Whitt and Thomas (2012) and (Rudnick, 2001). Because the lateral growth of these eddies is limited by the island cross section, they have a Ro that is the same order of magnitude as the "island" Rossby number, $\mathrm{Ro}_I = U/Lf$, where U is a characteristic velocity scale and L is

the island cross-section (Teinturier et al., 2010; Dong et al., 2007). This relationship has also been observed in the real ocean (Caldeira et al., 2014; Aristegui et al., 1994; Andrade et al., 2013; Heywood et al., 1990; Chang et al., 2013). In modeling and laboratory studies, there is evidence that rotation tends to inhibit the shedding of eddies as well as produce an asymmetry between anticyclonic and cyclonic eddies, when compared to flows with no background rotation (Heywood et al., 1996; Dong et al., 2007; Teinturier et al., 2010). Furthermore, for islands with strong variation in the Coriolis parameter (i.e. $f = f_0 + \beta y$ cannot be reasonably approximated as a constant, f_0), eastward flows have been shown to generate stationary Rossby waves which are believed to inhibit boundary layer separation (Boyer and Davies, 1982). Because these asymmetric effects of background rotation are difficult to observe directly in the real ocean, knowledge of the signed Ro is necessary for making comparisons to these idealized studies. This study quantifies Ro both upstream and downstream of Palau, as well as compares average properties of the currents over instances of eastward and westward flow.

Island wakes are also known to be highly variable, as demonstrated by satellite and in situ observations. Synoptic surveys of island wakes often capture significantly different wakes when sampled at different times. Heywood et al. (1990) demonstrated this variability using two rapid ship surveys around the island of Aldabra. They initially observed moderate currents and weak leeward return flow, but later found stronger flows and an associated shed vortex. Bowman et al. (1996) obtained similar observations between two surveys completed one year apart near Barbados. Island wakes have been shown to have significant spatial variability as well. Aristegui et al. (1994) used XBT and CTD data to describe the spatial structure of individual eddies in the vicinity of Gran Canaria. These eddies had horizontal length scales similar to the island diameter, but with different vertical length scales. These and other synoptic surveys produce high resolution "snap-shots" of coherent structures. To better understand island wake variance, authors have increasingly incorporated satellite data into their analysis. Hsu et al. (2017) used a six-month record of satellite sea-surface height (SSH) to calculate the statistics of island wake

spatial scales in the Kuroshio, as well as quantify mean values of incident velocity during times with and without vortex shedding. They found that velocities were on average twice as strong during periods of vortex shedding. Andrade et al. (2013) used 10 years of satellite data to track eddies near the Juan Fernandez islands using chlorophyll-a data from satellites, and discovered a seasonality in vortex shedding rates related to changes in wind stress and current direction. Caldeira et al. (2014) combined satellite observations with in-situ Lagrangian observations to follow the evolution of a single anticyclonic eddy in the lee of Madeira Island for three months, with a core Ro magnitude of up to 0.7. While satellite observations enable longer time series, the decreased resolution and dependence on sea-surface height anomalies to estimate surface currents limits observations to large, mesoscale eddies in quasi-geostrophic balance. Here mesoscale is defined as length scales greater than the first baroclinic Rossby radius of deformation (Chelton et al., 1998), often estimated as Rd = NH/f, where N and H are characteristic stratification and surface layer thickness. Sub-mesoscale eddies with potentially high Rossby numbers are not likely to be well characterized by satellite observations. This limitation underscores the need for obtaining sustained observations of absolute velocities in the vicinity of islands. In one of the few studies to do so, (Teague et al., 2002) used a 10-month record of ADCP velocities up- and downstream of Tsushima island to quantify mean properties of the wake and its variability. They observed elevated variance downstream, which they attributed in part to eddy shedding in a later study (Teague et al., 2005). They concluded that this variability leads to poorly-defined mean velocities downstream, thus demonstrating how synoptic measurements of island wakes may not be well representative of the mean. There is a clear need for more sustained in situ observations to improve our understanding of island wake variability, and how they relate to the mean properties of island wakes.

To help address this gap, we present observations from repeat glider sections to the east and west of the northern end of Palau, a large archipelago in the tropical north Pacific situated in the path of the westward North Equatorial Current. Directionally dependent mean sections of

velocity and vorticity are used to demonstrate that there is a recirculation in the lee of the island during periods of strong westward flow. This recirculation is accompanied by flow acceleration and strong vorticity with correspondingly high Rossby numbers (up to $|\mathrm{Ro}| = 0.3$ near the surface) for an island this size ($L \sim O(200\ \mathrm{km})$) with moderate incident current speeds ($U \sim O(0.1\ \mathrm{m\ s^{-1}})$). We will show that these high Ro are related to a wake length scale that reflects local details in the topography, and that energetic events can induce Ro exceeding $O(1)$. In contrast, the wake generated during during eastward flow does not generate comparably large Ro. This study is part of a larger field campaign (an Office of Naval Research (ONR) Departmental Research Initiative (DRI) 'Flow Encountering Abrupt Topography' (FLEAT)), which broadly aims to describe the Palau island wake at a variety of scales and increase our understanding of how island wakes are generated and how they impact regional circulation.

This paper is organized as follows: section 2.2 details the data and methods utilized in this study; section 2.3 presents results characterizing the mean flow around Palau and its variability; section 2.4 presents a discussion; section 2.5 is a summary of our conclusions.

2.2 Data and Methods

2.2.1 Oceanographic Setting

Palau is an archipelago oriented normally to two major zonal geostrophic currents in the western tropical Pacific – the North Equatorial Current (NEC) and North Equatorial Counter Current (NECC). The regional circulation around Palau has been studied in detail (Schönau and Rudnick, 2015; Qiu and Lukas, 1996; Qiu et al., 2013; Heron et al., 2006; Kashino et al., 2008), and the major surface features are identifiable in OSCAR surface currents (described below in section 2.2.4) averaged over the observational period (Figure 2.1). They are the NEC to the north of Palau, the NECC to the south, and the Mindanao Eddy (ME) to the west. Glider surveys conducted by Schönau and Rudnick (2015) from 2009 to 2014 show the NEC is made up of

a series of surface intensified cores between 8° and 20° N that migrate north to south with a seasonal cycle. The core velocities can reach up to 0.5 m s^{-1}. Underlying the NEC are a series of eastward subthermocline jets, the North Equatorial Undercurrents (NEUCs), which Qiu et al. (2013) suggest are generated by Rossby wave instability.

The main island of Palau is centered around 134.5° E, 7.5° N (Figure 2.2). Although most of the archipelago is subsurface, the 50 m isobath extends almost 200 km between 6.9° and 8.5° N (Smith and Sandwell, 1997). Beyond this isobath, gradients in the bathymetry can reach slopes of up to 45 degrees. Our survey was designed to capture the upstream and downstream conditions of the NEC as it circumvents Palau to the north. The glider lines are located on either side of Velasco, an atoll primarily composed of a sunken reef. Although the reef is entirely subsurface it can be as shallow as 20 m around the rim. To the south of Velasco is a deep channel reaching just under 1000 m at the sill. The glider lines were centered around the anticipated topographic separation point at the northernmost extent of the reef.

2.2.2 Dataset Description

Spray gliders are autonomous underwater vehicles that change buoyancy to profile from the surface down to as far as 1000 m (Sherman et al., 2001). The gliders carry a SeaBird Conductivity Temperature Depth sensor (CTD), a Seapoint Fluorometer and a 1 MHz Nortek Acoustic Doppler Current Profiler (AD2CP). The glider moves through the water at an average rate of 0.25 m s^{-1} in the horizontal and 0.1 m s^{-1} in the vertical, and data are collected during ascent. The processing of AD2CP data follows Todd et al. (2017) combining the relative velocity from the AD2CP with the depth-average velocity measured by the glider (Rudnick et al., 2018). Data are transmitted via satellite each time a glider surfaces, while raw data are stored on a flash drive and collected upon recovery.

The glider data in this study were collected between October 28, 2015 and January 13, 2018, along two parallel meridional sections 82 km apart on either side of Velasco reef. The

sections each run between 7.75° N and 9.00° N, one at 134.25° E and 135.00° E (hereafter 'Line W' and 'Line E' respectively) (Fig. 2.2). A total of 106 sections were completed on Line W and 85 on Line E. Each section took an average of 7 days to complete, and each mission completed an average of 14 sections. The gliders collectively achieved an average profile-to-profile horizontal resolution of 4.7 km and temporal resolution of 6 hours. The profiles are down to 1000 m and are vertically averaged into 10 m bins after quality controlling the CTD data and computing velocity with the AD2CP data.

A few gaps in the time series were caused by operational issues. The second glider mission along Line W returned with a corrupted flash drive. Binned CTD data from the satellite communications are available, but there is no AD2CP data from this run, spanning February 16, 2016 through June 6, 2016. Coincidentally, during the same period the other glider (running Line E) was swept north in an anomalously strong northward current. As a result there is no ADCP data on either line during this period. Shorter gaps in the ADCP data are due to deployment and recovery.

2.2.3 Objective Map

Figure 2.3 shows an example zonal velocity section along Line E. Internal wave motions and tides appear in the section as isopycnal heaving and velocity variability on spatial scales shorter than 30 km (Rudnick and Cole, 2011). To filter out high frequency variability, AD2CP data were objectively mapped onto a regular grid (3 km by 3.5 day) using a Gaussian autocovariance. Statistics are assumed to be stationary and homogeneous. To determine the appropriate time and length scales for the Gaussian function, the autocorrelation of each variable was calculated as a function of lag in space and time. Anomalies were calculated at each depth with respect to a linear trend in latitude and averaged into bins of 14 days and 5.6 km, and then again in depth. These bins correspond to twice the average separation between sections in time, and the average horizontal resolution along the section. The autocorrelation of zonal velocity along Line E and

Line W are shown in Figure 2.4. Zonal velocity is shown as we are interested primarily in flow past the island. Additionally, zonal velocity exhibits the shortest time and length scales of all variables and so places a lower limit on them. Distance north is taken to be positive, and so the slope in autocorrelation along Line E corresponds to anomalies propagating northward at a velocity of 0.05 m s^{-1}. This is the average meridional velocity down to 200 m along Line E (the average base of the pycnocline, not shown), where there is also significant mesoscale eddy activity (Schönau and Rudnick, 2015). This suggests that the slope in autocorrelation is due to the meridional advection of mesoscale eddies in the NEC. The decorrelation length scale along Line W is less than 50 km, in sharp contrast to Line E which demonstrates almost total meridional coherence. The significance of this disparity is discussed in the results section (2.3). The decorrelation time scale for both lines is no more than two weeks. We choose 30 km and 14 days for decorrelation length and time scales to preserve the variability on the shortest reasonable scales attainable by the glider data. We do not resolve all scales that may be energetic, and it is possible that there are higher Rossby number motions than those observed in this study occurring on scales less than 30 km and 14 days.

Variables were mapped individually on levels separated by 10 m in the vertical. The ratio of noise to signal variance was taken to be 0.1, and points in the map with error to signal variance greater than 0.1 are masked. The result is a regular grid in latitude, depth, and time for each variable, with respective resolutions of 3 km, 10 m and 3.5 days and overall spans of 140 km, 1000 m, and 807 days. The total number of objectively mapped ADCP sections along Line W and Line E are 191 and 154 respectively. All mapped sections on Line E correspond to a mapped section along Line W, however there are sections where there is only mapped data along Line W, meaning there are 154 total sections with data mapped along both lines. Each section corresponds to a single date and time, compared to the glider surveys which span about a week. Figure 2.5 shows a section of the objective map that is concurrent with the survey period of the original example section in Fig. 2.3. The large-scale structure has been preserved, while the smaller scale

fluctuations have been filtered. All subsequent calculations use the objectively mapped data.

2.2.4 Eastward and Westward Flow Definitions

The zonal component of the currents moving past Palau dictate whether the vorticity produced is cyclonic or anticyclonic, with the potential to generate asymmetric wakes (e.g Heywood et al., 1996). Further, strong variability of the flow direction can make interpreting an absolute mean difficult (e.g Teague et al., 2005). To quantify this asymmetry and mitigate the impact of flow variability on interpreting the mean we calculated direction-dependent mean velocity sections. Time series of depth-average velocity vectors along each section demonstrate that velocity is largely coherent across Line E but exhibits latitudinal variance along Line W, consistent with autocorrelations of zonal velocity (Figure 2.6). Qualitative inspection reveals that the westward incident flow tends to split upstream at about 8.2° N, with flow typically heading northward around the island when it is incident north of this latitude. Therefore, we use velocities north of 8.2° N to characterize the flow direction. We calculate the depth-and-latitude averaged velocity along each section and designate the flow as "westward" ("eastward") if the direction is +/- 60° from west (east) along Line E (Line W). Because each line is treated independently, a small portion of sections fell into both categories. Visual inspection of these sections suggested that they were most like the westward sections and are included in that mean. However, this inclusion did not change the results markedly. There were 90 (42) sections with westward (eastward) flow. This number corresponds to 58% (27%) of sections that have mapped data along both Line E and Line W. We therefore expect averages taken over all westward sections to resemble the total mean. No sections in which there was data only along Line E or Line W are included.

2.2.5 OSCAR Surface Currents

Ocean Surface Current Analysis (OSCAR) Third Degree near-surface currents are used in this study to provide regional context for the glider data close to Palau. The OSCAR data were obtained from the Jet Propulsion Laboratory (JPL) Physical Oceanography Distributed Active Archive Center (PO.DAAC) and developed by Earth & Space Research (ESR, 2009). Horizontal velocities are computed using sea surface height (SSH), surface wind and sea surface temperature (SST) by combining geostrophic, Ekman and Stommel dynamics (Bonjean and Lagerloef, 2002). Each component (i.e. SSH, SST and wind vector) is derived from a combination of satellite and in-situ instruments, and the final product is mapped onto a 5 day by 1/3° (both in latitude and longitude) grid. The OSCAR product does not represent local acceleration and non-linearities. As such it is best used to describe the large-scale circulation, as in this study. As a result of this, surface currents are mapped across Palau, as evident in Fig. 2.1. Further information about the processing methods for OSCAR surface currents can be found in Bonjean and Lagerloef (2002).

2.3 Results

2.3.1 Mean Currents and Variability

Mean sections of velocity show that on average, the incident westward NEC accelerates around the northern end of Palau and experiences flow separation which induces a reversal of the currents in the lee (Figure 2.7). Because zonal velocity is primarily westward, Line E is upstream in the mean and Line W is downstream.

Upstream, incident currents are north-westward and both components of velocity are surface intensified (Fig. 2.7b and 2.7d). Despite this vertical shear, the flow direction is relatively uniform with depth. Depth-average velocity is strongest near the northernmost extent of the reef (grey dashed lines) and diminishes south of 8.2° N. At the northern end of the section there is

subthermocline eastward flow, between about 300 and 600 m depth. This may be an eastward flowing NEUC that typically lies to the north, migrating south (Schönau and Rudnick, 2015).

Downstream the flow develops latitudinal structure (Fig. 2.7a and 2.7c). North of the reef, zonal velocity is westward and sheared, similar to the current upstream. However, the magnitude of the current increases substantially, from about 0.1 to 0.2 m s^{-1} near the surface. This strongly suggests that the flow accelerates as it passes the island. Zonal velocity decays to zero close to the edge of the reef and changes sign in the lee, indicative of flow separation. Currents are eastward almost everywhere in the lee of the island. There is some westward flow shallower than 200 m, between 8° and 8.2° N. Below this westward flow, the eastward flow is weakest. Meridional velocity is northward, surface intensified, and weakest where the zonal flow goes to zero. Depth-averaged velocity vectors illustrate the resulting meander of the wake (Fig. 2.7e).

Velocity variability similarly has features induced by the island (Figure 2.8). Variability, measured as the standard deviation of velocity between sections (both zonal and meridional), is surface intensified and elevated to the north of the reef along both lines. Absolute differences between Line E and Line W (not shown) indicate that zonal velocity variability increases downstream and north of the reef by about 30% near the surface, and decreases by up to 50% in the lee (in the subthermocline). Meridional velocity variability has minimal lateral structure (Fig. 2.8c and 2.8d). Teague et. al. (2002) found similar elevated variance downstream of Tsushima island, which they attributed in part to eddy shedding in a later study (Teague et al., 2005).

2.3.2 Westward Flow

Selecting for westward flow produces sections of mean velocity that closely resemble the total mean, but with a few differences that have significant dynamic implications (Figure 2.9). As with the total mean, upstream zonal velocity is primarily north-westward and highly surface intensified. However the maximum surface zonal velocity exceeds 0.2 m s^{-1} near the northern end of Line E, and the subthermocline flow diverges near 8.2° N. The latter is strong evidence of

topographic blocking, i.e. upstream influence of the island. This feature did not appear in velocity sections averaged over the entire time series (Fig. 2.7).

Downstream, changes to the mean are more striking. North of the reef the mean surface zonal velocity accelerates to over 0.3 m s^{-1}, and in the lee of the island the return flow is confined to a 40 km region from 8.2° N to the reef edge (Fig. 2.9a). Plotting the bathymetric cross section of Velasco over zonal velocity (dashed black line) suggests a forcing for this length scale. The sill of the channel separating Velasco reef from the rest of Palau is deep enough to allow westward flow through to the lee. This channel flow was observed to reach values exceeding 0.5 m s^{-1} as part of another FLEAT study using SeaSoar towed profilers (Ou and Johnston, personal communication). This strong current appears to limit the return flow to the area directly behind the reef.

The wake during westward flow has a more complex depth structure than the total mean wake. Depth-average velocity vectors for westward flow are plotted in intervals of 100 m in Figure 2.10. These vectors highlight the strength of the vertical shear in the incident current, which may alter the flow dynamics significantly with depth. Downstream (Fig. 2.10b), acceleration is apparent north of the ridge. Westward flow through the channel is so strong in the upper 200 m that it almost completely overpowers the shallow eastward return flow. As the channel flow weakens with depth the magnitude of the return flow increases, suggesting that changes in the topography have a first-order impact on the strength of the wake. Near the surface, the meridional component of velocity is northward, but as the flow weakens with depth it turns southward. As a result the mean lateral position of the return flow moves south with depth.

The primary features of velocity variability that appear in the mean (i.e. surface intensification, patterns of downstream increased/decreased variability north/south of the reef) are apparent during westward flow as well, although overall the standard deviation is lower due to selection of similar flow configurations (Figure 2.11). However in the total mean, variability across each line is elevated north of the reef. This feature no longer appears upstream (along Line

E) after selecting for westward flow, leading to a relative increase in the standard deviation north of the ridge of over 100% as the flow accelerates. This suggests that elevated variability north of the ridge is a downstream phenomenon, tied to the flow acceleration and separation. Thus, we expect this pattern to be reversed for eastward flow.

2.3.3 Eastward Flow

Mean sections of velocity during eastward flow reveal a striking asymmetry in both the wake and incident current (Figure 2.12). For eastward flow, Line W is upstream and Line E is downstream. Although the depth-averaged flow is eastward across the reef (by definition), westward flow persists near the surface. In the upper 50 m zonal velocity is westward along Line E as well as the northern and southern ends of Line W, similar to the incident flow and wake generated during westward flow. The location of the return flow is more northward, likely due to the stronger incident meridional velocities along Line E. This persistence of westward flow at the surface suggests that eastward flow may be a waning of the sheared westward flow rather than a total flow reversal, in which eastward flow would be similarly surface intensified in the eastward direction and coherent along Line W.

Nonetheless, the subthermocline upstream zonal velocity is entirely eastward. Meridional velocity diverges near 8° N, suggestive of topographic blocking. Downstream, there is westward flow in the lee of the island south of $\sim$ 8.3° N. However, meridional velocity in the lee is northward and greater in magnitude than zonal velocity, suggesting that the flow along Line E may instead be coming from the south, rather than from the west and across the reef. If this is so, it is unlikely that the westward flow along line E (south of 8.2° N) is return flow resulting from boundary layer separation. Velocity variability (not shown) is lower overall during eastward flow, but is elevated to the north of the reef and downstream. Depth-average velocity vectors (over 100 m intervals) highlight the persistence of westward flow at the surface, as well as the strength of the northward component of the flow downstream (Figure 2.13). Although the incident

subthermocline velocity is very similar to that of westward flow (reversed zonally), the wake structure is quite different for reasons suggested above. To better understand these asymmetries, OSCAR surface currents averaged over each flow regime are examined in section 2.4. If eastward flow cannot be considered a simple flow reversal, it is difficult to draw meaningful comparisons with any asymmetries predicted by quasi-geostrophic theory (Boyer and Davies, 1982; Musgrave et al., 2018).

2.3.4 Vorticity

The source of vorticity in the wake is thought to be the velocity gradient over the width of the frictional boundary layer (Kundu and Cohen, 1990). Any attempt to characterize the wake behind Palau must therefore involve an estimate of the vorticity generated. Because the sections are meridional, we approximate vorticity using the meridional gradient in zonal velocity alone ($\zeta = -dU/dy$). To estimate our error, we consider two plausible extremes. In the case of solid body rotation (i.e. $-dU/dy = dV/dx$), this may be an underestimate of the magnitude of the vorticity up to a factor of two. On the other hand, if the flow is entirely zonal then we have measured the total vorticity. Because there are strong jets through the channel and around the reef, it is implausible that zonal gradients are larger than meridional gradients. This suggests our approximation is valid, and at most an underestimate of the total vorticity. Further discussion of this approximation may be found in Rudnick (2001) and Shcherbina et al. (2013).

Mean vorticity during westward and eastward flow emphasizes the directional asymmetries previously identified in mean sections of velocity (Figure 2.14). Here vorticity has been normalized by the local Coriolis parameter, giving the Rossby number (Ro = ζ/f, with $f = 2.17 \times 10^{-5}$ s^{-1}). Downstream during depth-average westward flow (Fig.2.14a), mean Ro exceed 0.3 near the surface. During depth-average eastward flow this feature appears upstream (Fig.2.14c) and downstream Ro are weak (Fig.2.14d), due to the persistence of westward flow at the surface. Ro variability along both lines (not shown) is high: ~ 0.1 in the subthermocline and

up to 0.3 in the surface layer. Therefore the lack of a strong vorticity signature upstream during westward flow (Fig.2.14b) implies that there is no preferred sense (cyclonic or anticyclonic) to the incident vorticity field, and the lateral structure downstream in the mean is due to the presence of the island.

2.3.5 Event Driven Variability

Hovmoller diagrams of depth-average shallow (0–100 m) zonal velocity and normalized vorticity demonstrate that the return flow and large Ro downstream are consistent features throughout the time series, and that the high Ro variability is in large part due to energetic low-frequency events (Figures 2.15 and 2.16). This depth interval was selected to isolate the surface currents characterized by elevated variability. It is roughly equivalent to an isopycnal of 26 kg m^{-3} in the mean, which Schönau and Rudnick (2015) used to distinguish between the NEC and NEUCs.

Along Line E (upstream in the mean), zonal velocity is mostly westward and coherent across the section (Fig. 2.15a). Along Line W (downstream in the mean), return flow appears as a band of intermittent eastward velocity centered around 8.4° N. This intermittency supports an interpretation of the wake as eddying but may also be explained by fluctuations in the strength of the incident current on time scales of days-weeks. Although this higher frequency variability persists across the entire time series, there are a few low frequency events that dominate the signal. Particularly energetic periods include strong eastward flow in July of 2016 and January of 2017, and strong westward flow in July of 2017. The latter occurred during the longest period of westward flow captured in the time series. Although gaps in the sampling along Line E partially obscure the upstream velocity, the persistent pattern of westward currents and recirculation along Line W starting in March 2017 and through the end of the time series suggests that this event lasted at least 7 months. The strength of the shallow current fluctuates between 0.1 and 0.3 m s^{-1} for most of this period but exceeds 0.5 m s^{-1} during the summer of 2017.

These events have significant implications for the wake Ro over time, as demonstrated by similar Hovmoller diagrams of vorticity (Figure 2.16). Along Line E there is no preferred sense to the vorticity, leading to low Ro in the mean ($|\text{Ro}| < 0.1$, Fig. 2.14). Along Line W however, the intrinsic background vorticity fluctuations are transformed into persistent features of elevated positive and negative vorticity. This is especially true during periods of sustained westward flow. Strong currents during July 2017 correspond to downstream vorticity values exceeding the local Coriolis frequency, f (i.e. $\text{Ro} > 1$). By comparison, periods with strong eastward currents do not produce similarly strong negative vorticity downstream. This disparity is emphasized in a time series of section-integrated, depth-average vorticity flux (Fig. 2.17a). There is a moderate peak in the vorticity flux along Line W in December of 2015 and substantial one in July 2017, both corresponding to periods of strong westward flow (Fig. 2.17b). Three shorter periods of eastward flow with similar intensities (January 2016, July 2016, January 2017) have no vorticity flux signature. These low-frequency, high Ro events are confined to the surface. Subthermocline $|\text{Ro}|$ only briefly exceeds 0.2, and predominantly stays near 0.1 (not shown). The Ro of the surface wake is therefore up to an order of magnitude greater than the subthermocline.

2.4 Discussion

In this paper, glider observations are used to characterize the mean mesoscale flow around the northern end of Palau. On average, surface intensified westward flow encounters the meridionally elongated island normally, is topographically blocked and accelerates to pass the island. As the current flows around the reef it separates, leading to a region of return flow in the lee of the island. Velocity variability is elevated downstream in the intensified surface layer as well as throughout the water column and north of the reef. While on average there is return flow everywhere directly downstream of Palau, during westward flow the length scales in the wake reflect the local topography (i.e. Velasco reef). This may be caused by strong currents

through a deep and narrow channel separating the reef from the rest of the archipelago. Mean depth-average eastward flow is accompanied by persistent westward flow at the surface and strong northward currents in the lee. While westward flow produces a distinctive vorticity signature downstream with average absolute Rossby numbers at the surface exceeding 0.3, eastward flow does not produce comparably strong vorticity. Hovmoller diagrams of zonal velocity and normalized vorticity reveal significant variability of the wake on timescales greater than a month, and especially energetic events that induce vorticity that can exceed the local Coriolis frequency (i.e. Ro > 1).

2.4.1 Rossby Number

The high Ro observed in the wake of Palau has important implications. Large islands ($O(100$ km$)$) often induce wakes with low Ro due to the inverse dependence on length. These wakes, with Ro = $O(10^{-1})$ or smaller, are often in geostrophic balance (Caldeira and Sangra, 2012b; Dong et al., 2007; Aristegui et al., 1994), and can remain coherent for hundreds of kilometers downstream (Caldeira et al., 2014). For smaller islands with much higher absolute Ro ($\rightarrow O(1)$) ageostrophic effects become important. Numerical studies have shown that wake eddies with large Ro are susceptible to destabilizing instabilities and can quickly lose their integrity downstream (a detailed treatment of these instabilities can be found in (Dong et al., 2007). Caldeira and Sangra (2012b) demonstrated a case where changes in the incident flow direction reduced the cross section of an oblong island, which then went from producing robust, large, geostrophic eddies to smaller, ageostrophic eddies that dissipated within a few island lengths downstream. It might be reasonable to hypothesize that Palau would have a small Ro, and subsequently produce large, geostrophic eddies. The large-scale cross section as seen by east-west flows is ~ 200 km, mean surface velocities of the NEC are ~ 0.2 ms^{-1} (Schönau and Rudnick, 2015), and the local Coriolis parameter is $\sim 2 \times 10^{-5}$ s^{-1}, giving Ro = $O(10^{-2})$. However, we have observed a mean Ro that is an order of magnitude higher ($O(10^{-1})$), as well

as instantaneous values that can exceed 1. This suggests that it is unlikely these eddies are in geostrophic balance and therefore may lose their integrity within a few island lengths. If so, the wake produced by Palau may have an exclusively local impact. This interpretation is supported by the mean OSCAR surface currents around Palau, which show that the wake extends no more than 100 km on average to the west (Fig. 2.1).

2.4.2 Shedding Frequency

It is useful to estimate how often wake eddies are shed from Palau. In laboratory flows, the Reynolds number, Re, controls the frequency of eddy shedding through an empirical relationship with the Strouhal number, St (Zdravkovich, 2000). Here Re = UL/ν and St = $U/\omega_e L$, where U and L are characteristic velocity and length scales, ν is the molecular viscosity and ω_e is the shedding frequency. It is common practice to replace the molecular viscosity with a turbulent eddy viscosity, ν_e, in the ocean. This parameterization, which introduces an effective Reynolds number (Re_e), is supported by observations showing that the large-scale structure of island wakes with Re of up to $O(10^{10})$ are often qualitatively similar to laminar wakes with Re of $O(10-10^2)$ (Barkley, 1972). A common choice of ν_e is $O(10^2)$ m^2 s^{-1}, which agrees reasonably well with direct measurements in the open ocean (Ledwell et al., 1998; Heywood et al., 1990; Chang et al., 2013; Caldiera et al., 2005; Herandez-Leon, 1991). Here we assume $\nu_e = 100$, keeping in mind that our estimate of the Re_e is dependent on this choice. The eddy viscosity is explored further in section 2.4.4. We take U to be the incident shallow current far north of topographic blocking during westward flow, ~ 0.2 m s^{-1} (Fig. 2.9). While L is typically defined as the island cross section, our observations suggest this is not the relevant scale here. We instead take L to be the along-stream extent of the boundary layer, as this is the source of wake vorticity. Assuming the boundary layer develops near the blocking latitude, $L \sim 70$ km (Fig. 2.9). This gives a $\mathrm{Re}_e \sim 140$ for the shallow surface layer during westward flow. For $40 < \mathrm{Re} < 400$, St is given by $0.212(1-21.2/\mathrm{Re})$ (Roshko, 1954). This gives St = 0.18 for our estimate of Re_e, which

corresponds to an eddy shedding period of about 23 days. We have observed at least two periods of westward flow sustained for more than a month (November 2017 through February 2016, and June through October 2017), which would suggest that eddies are shed at least a few times a year. However, velocity and vorticity variability are high, and we may expect a wide range of behavior. When the flow is weakest and $\mathrm{Re}_e < 1$, it is likely there is no wake (Roshko, 1954). At its strongest, the incident velocity can exceed 0.5 m s^{-1} in the shallow surface layer (Fig. 2.16 and 2.17), with correspondingly high Rossby numbers ($\mathrm{Ro} \to 1$). For these swift flows, Re_e can exceed 300. This corresponds to an eddy shedding period of about 10 days. In other words, while the mean Re_e of Palau suggests that eddies are shed roughly monthly, in light of the observed variability it is more likely that the flow around the island oscillates between a mode of vigorous eddy shedding for sustained periods of swift westward flow, and no developed wake for periods of weak flow.

2.4.3 Depth Dependence

A similar calculation of Re_e below the surface layer suggests that the dynamics in the subthermocline are possibly quite different. $\mathrm{Re}_e \sim 28$, which is below the cutoff value for vortex shedding ($U \sim 0.07$ m s^{-1}, $L \sim 40$ km). While eddies may be shed in the shallow surface layer on average, it is possible that they remain attached to the island in the subthermocline. One way to evaluate the dynamic link between the surface and subthermocline current is to look at their relative transport variability. Schönau and Rudnick (2015) found the section integrated zonal transport across the NEC in the surface layer to be strongly correlated with transport in the NEUCs. They report a transport correlation value of R = 0.87. In this study there is a similarly high correlation between the surface and subsurface flow along Line E (upstream in the mean), R = 0.71 across the total time series. However, along Line W (downstream in the mean) it drops to R = 0.45. This is consistent with the inference that the surface and the subsurface flow become decoupled due to their different dynamic responses to the island. It is worth noting that when

considering the depth structure of the wake we must acknowledge an additional length scale, the deformation radius. An estimate of Rd using mean shear and stratification near Palau gives Rd = $O(100$ km), on par with the island length scale. This suggests that the effects of stratification in determining the wake dynamics are non-negligible, further complicating the relationship between the surface and subthermocline wake.

2.4.4 Eddy Viscosity

There are physical reasons that $\nu_e = O(100)$ may be an appropriate estimate of the turbulent eddy viscosity around Palau. In a numerical study of idealized turbulent island wakes, (Dong et al., 2007) found that the boundary layer obeyed a similar power law to that of a viscous boundary layer ($\delta \sim \mathrm{Re}^{1/4}$, where δ is the width of the boundary layer (Walker and Stewartson, 1972)). Motivated by this and the broad similarities between island wakes and laminar flows, we will apply laminar boundary layer theory to estimate the eddy viscosity. The width of a laminar boundary layer is given by $\delta(L) = 5\sqrt{\nu L/U}$ (Blasius, 1908), and the vorticity across the boundary layer at separation is given by $\zeta = U/\delta(L)$. The eddy viscosity can thus be written in terms of the velocity, vorticity and length scales as $\nu_e \sim \delta^2 U/25L \rightarrow U^3/25L\zeta^2$. We can estimate the scale of the boundary layer vorticity from the values observed downstream near the surface during westward flow ($\zeta \sim 7 \times 10^{-6}$ s^{-1} (Fig. 2.14)). With our length and velocity scales defined above, this gives $\nu_e \sim 90$ m^2 s^{-1}, in good agreement with values typically assumed in other island wake studies. There is further evidence to suggest that this value is physically meaningful. As part of another study in the FLEAT program, a ship survey was conducted around Velasco in June 2016. Strong tidal currents ($O(10^{-1})$ m s^{-1}) were observed to generate eddies about 1 km in scale. If these types of eddies are the dominant process responsible for transferring momentum within the mesoscale boundary layer, we can estimate an associated eddy viscosity as the product of their speed and path length, i.e. $\nu_e \sim 100$ m^2 s^{-1} (Vallis, 2006). This value is consistent with both our boundary layer estimate and the literature. These arguments are speculative, but their

agreement with the literature supports our choice of eddy viscosity and the subsequent inferences about wake behavior.

2.4.5 Regional context

Mean velocity and vorticity sections are fundamentally different during eastward and westward flow (Fig. 2.9, Fig. 2.12, Fig. 2.14). OSCAR surface currents and normalized surface vorticity (Ro) averaged over westward and eastward flow reveal that the regional context for the two flow regimes differs substantially (Fig. 2.18). On average during westward flow a strong south-eastward NECC passes closely to the southern tip of Palau and a steady broad westward NEC extends from the north to just south of the island. There is a strong negative vorticity signature directly to the west of the southern end of Palau, and a weaker positive one west of the northern end. This is the wake induced by flow around Palau. During eastward flow, the NECC moves southward and increases in intensity. This shift is accompanied by the development of a strong north-westward current directly south of Palau that further intensifies the negative vorticity signature in the lee of the island. This feature dominates the wake, and the northern end of Palau is consumed by return flow from the south. However, the NEC persists and the surface currents converge around Velasco, as evident in surface depth-average velocity (Fig. 2.13). This shift in the regional circulation is consistent with the seasonal variability in the region identified by Hsin and Qiu (2012). Using OSCAR surface currents averaged over an 18-year period they show that the NECC west of 140° E moves southward in the winter/spring and northward in the summer/fall , driven by the westward propagation of downwelling Rossby waves. Out of three major eastward events observed, two occur in the winter (2016 and 2017, not shown) consistent with this seasonal migration. They are characterized by persistent westward flow at the surface and eastward flow in the subthermocline. The third event occurred in July 2016 and was characterized by a weak NECC and increased eddy activity throughout the entire region. It was also the only period in the glider time series with strong eastward flow at the surface. This

disruption of the regional circulation was likely caused by relaxation of the 2015-2016 El Nino event (Lim, 2017). One of the motivations for this paper was examining potential asymmetries between wakes generated by otherwise symmetric eastward and westward flow, as predicted by quasi-geostrophic theory (Boyer and Davies, 1982; Musgrave et al., 2018). However, the seasonal and interannual variability of the regional circulation detailed here indicates that eastward flow is not a simple current reversal of the NEC. Instead it is the result of complicated interactions between the NEC, NECC and Palau, obscuring such inferences.

2.5 Conclusion

In this paper we have presented sustained (two year) observations of a large island wake using autonomous underwater gliders. On average flow impinges on the island from the east, accelerates around the topography and separates, leading to return flow in the lee of the island. We have demonstrated that this return flow is confined to a region that is much smaller than the total cross section of the island due to details of the topography, and have linked this reduced length scale to high Rossby numbers in the wake.

As with most island wake studies the incident flow and wake around Palau were shown to be highly variable. This is in part due to energetic low-frequency, large-scale events in which the flow direction often reverses. We have shown that the extremes (energetic eastward and westward flow) exist under different regional current conditions. It is suggested here that for the weakest incident currents there may be no flow separation, whereas the swiftest flows develop eddies with high Ro that shed on the order of days. Further, we have suggested that the dynamic link between the surface currents (the NEC) and the undercurrents (the NEUCs) found by Schönau and Rudnick (2015) is likely decoupled as a result of the interaction with the island. This may be due to shear of the incident current and the subsequent order of magnitude difference in the Rossby number of the surface and subthermocline wakes we have observed.

Knowledge of such non-dimensional parameters enables comparisons between islands across a wide range of scales, as well as with idealized numerical studies and theory. However they are often inferred indirectly from sparse observations. The time-dependent Ro measured in this study is up to an order of magnitude larger than what might be inferred from a reasonable back of the envelope estimate based on knowledge of the velocity alone. This suggests that ageostrophic effects may often be important to first order in the wake of Palau, and subsequent destabilizing instabilities may limit its zonal extent. This finding underscores the need for sustained island wake observations, as limited synoptic surveys may not capture such strong vorticity.

In sum, a primary conclusion of this study is that the variability of the flow around Palau leads to a wide range of dynamics in its wake. Estimates of the vorticity generated by islands which fail to account for this variability will likely misrepresent the net vorticity flux into the interior over time. An improved understanding of how intrinsic flow variability influences vorticity production is necessary to continue building on the significant insights provided by idealized studies (e.g Dong and McWilliams, 2007; Heywood et al., 1996; Jimenez et al., 2008). For example, as is common practice with geophysical flows we have used an assumed eddy viscosity to determine the Reynolds number. We have hypothesized that the value obtained may be physically meaningful by linking it to the size and velocity of small-scale, high-frequency tidal eddies observed around Velasco. Further work is required to test the validity of this speculation, and explore the relationship between small-scale processes near topography and large-scale wakes. While the parameterization of momentum diffusivity using an eddy viscosity is founded on physical principles that are well understood, the dependence of this value on the larger scale flow has not been explored in great detail. This is in no small part due to the difficulty in observing a wide range of scales at once. A more complete understanding of the wake produced around Palau will hinge on elucidating the vorticity generated across a wide range of scales. This is the subject of future FLEAT studies.

2.6 Acknowledgments

Spray underwater glider data used in this paper are available at spraydata.ucsd.edu. OSCAR surface currents referenced in this paper were obtained from JPL Physical Oceanography DAAC and developed by ESR (ESR, 2009). Glider observations and analysis were funded by the Office of Naval Research as part of the Flow Encountering Abrupt Topography (FLEAT) project through grant N00014-15-1-2488. We thank the Instrument Development Group at Scripps Institution of Oceanography for all facets of the operations of Spray underwater gliders. We thank Pat and Lori Colin at the Coral Reef Research Foundation for their support in Palau.

Chapter 2, in full, is a reprint of the material as it appears in Zeiden, K.L, D.L. Rudnick and J.A. MacKinnon (2019). Glider Observations of a Mesoscale Oceanic Island Wake. Journal of Physical Oceanography, 49, 2217– 2235, doi: 10.1175/JPO-D-18-0233.1. Used with permission from ©American Meteorological Society. The dissertation author was the primary investigator and author of this paper.

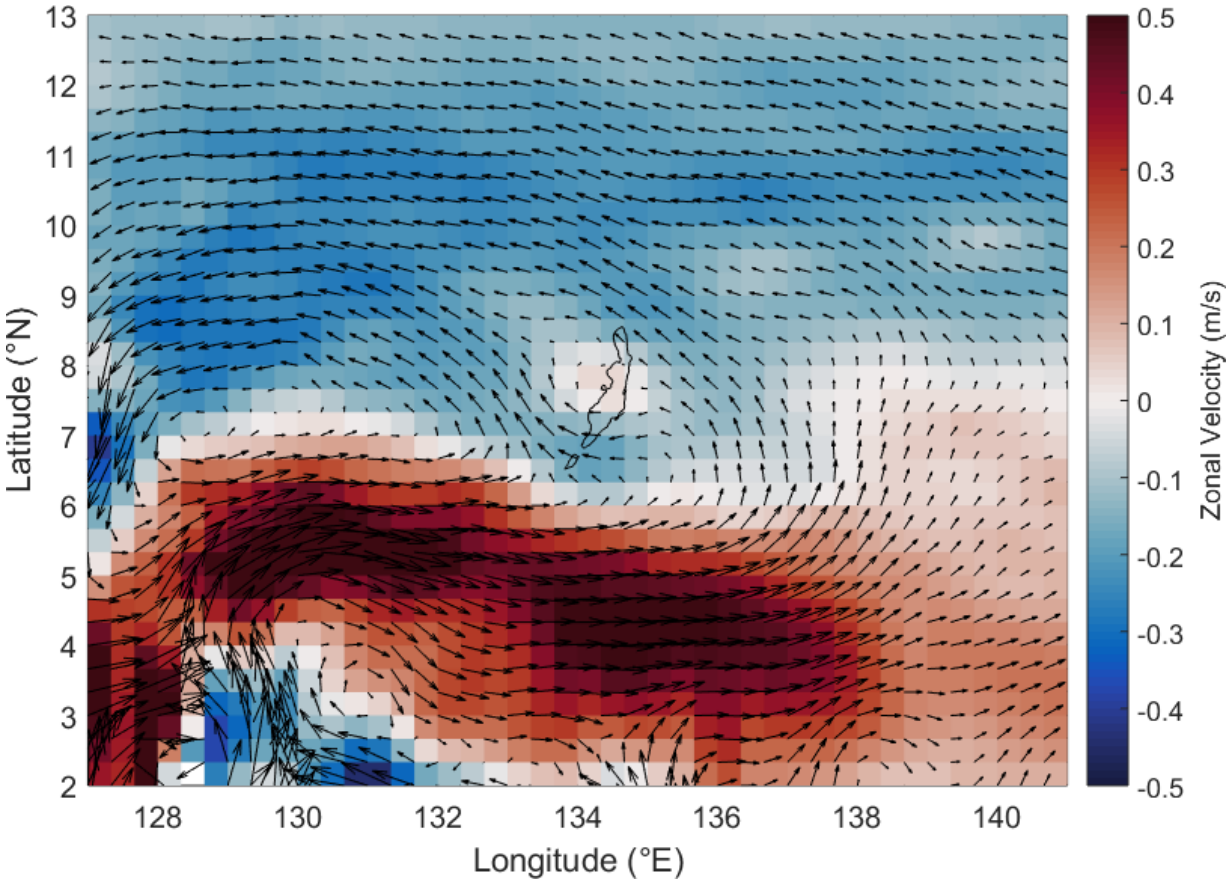

Figure 2.1: OSCAR surface currents (vectors) averaged over the glider observation period and shaded by zonal velocity. The weak, broad westward current to the north of Palau (black contour) is the North Equatorial Current (NEC), and the strong eastward current to the south is the North Equatorial Counter Current (NECC). The Mindanao Eddy (ME) lies to the west. The variability of these three major regional circulation features has a major impact on the local circulation around Palau (Heron et al., 2006).

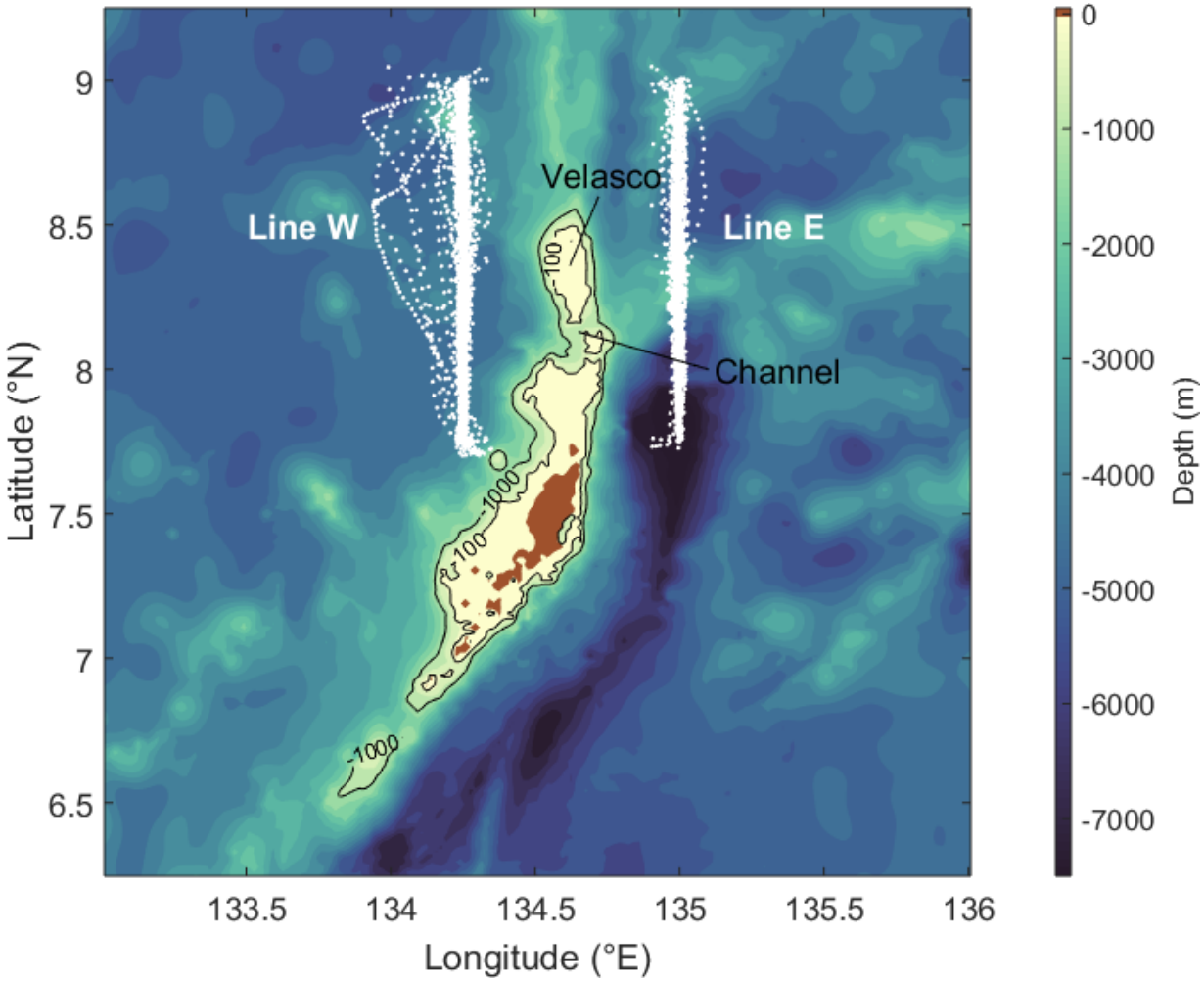

Figure 2.2: Glider dives are plotted in white over the local bathymetry. Gliders sampled between 7.75° and 9° N, along 134.25° (Line W) and 135° E (Line E). Over 5500 dives were completed between October 2015 and January 2018. The 100 and 1000 m isobaths are contoured in black to emphasize the steepness of the topography around Palau. Centered between the glider lines is a sunken reef called Velasco which is 20 m deep around the rim. Between Velasco and Palau is a narrow, deep channel with a sill reaching just under 1000 m.

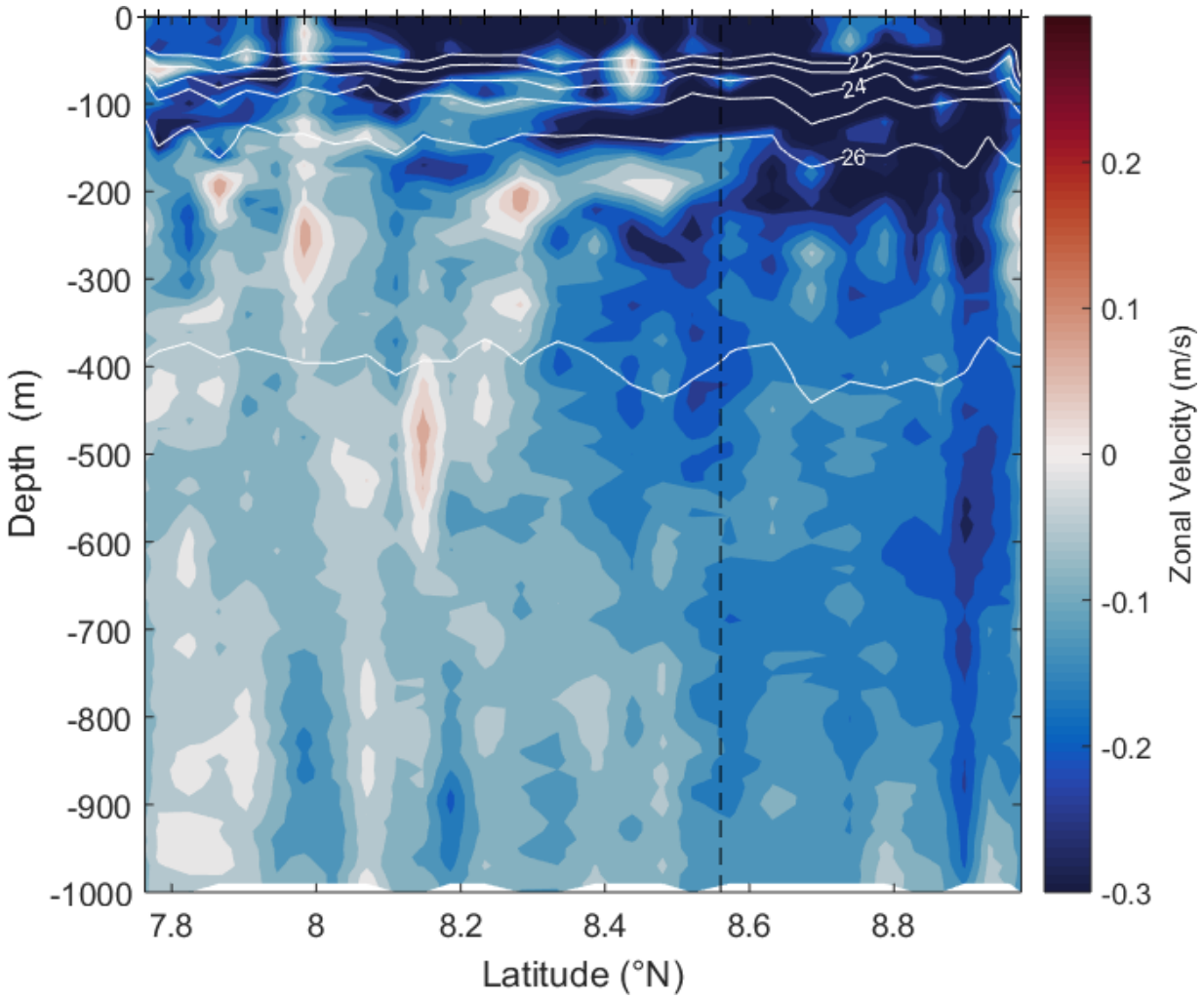

Figure 2.3: Example glider section along Line E, completed between November 24 and December 2, 2015. Filled contours display zonal velocity, with blue indicating westward velocity. Isopycnals (white contours) exhibit heaving in part due to aliased internal wave motions. Density interval is 1 kg m^{-3}. Line E is upstream in the mean, capturing the surface-intensified westward NEC as shown here.

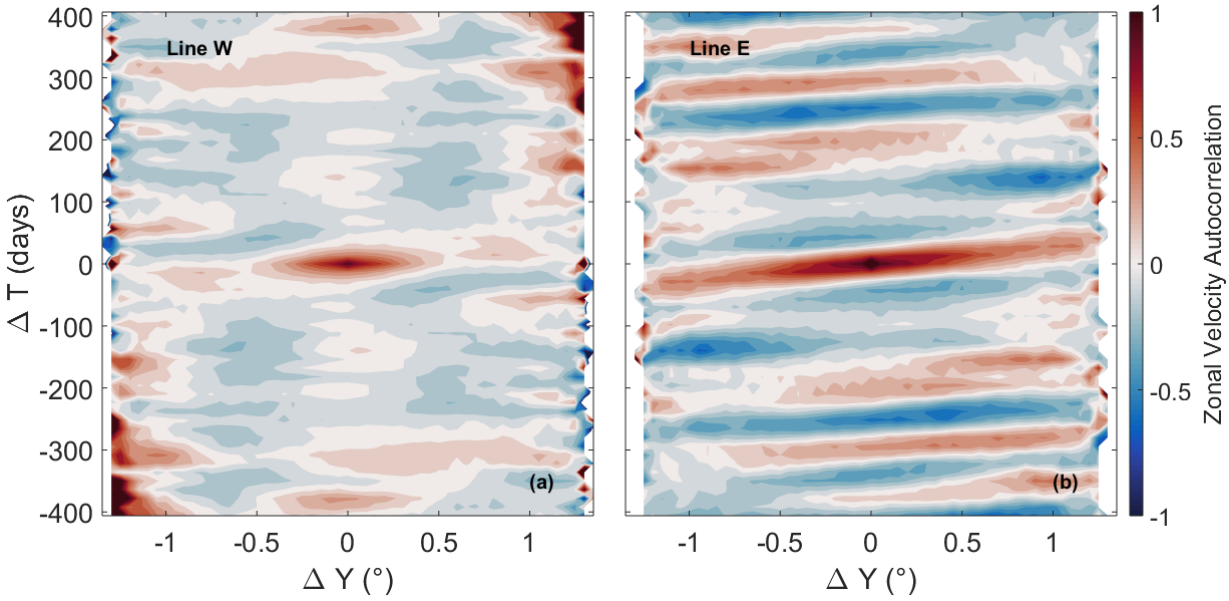

Figure 2.4: Autocorrelation of zonal velocity as a function of lag in latitude and time, calculated at each 10 m depth bin and averaged over the water column for Line W (a) and Line E (b). Both lines exhibit a decorrelation timescale of no more than two weeks, and while zonal velocity is coherent across the line on Line E, the decorrelation length scale along Line W is less than 50 km. These limiting time and length scales inform the choices made in creating an objective map.

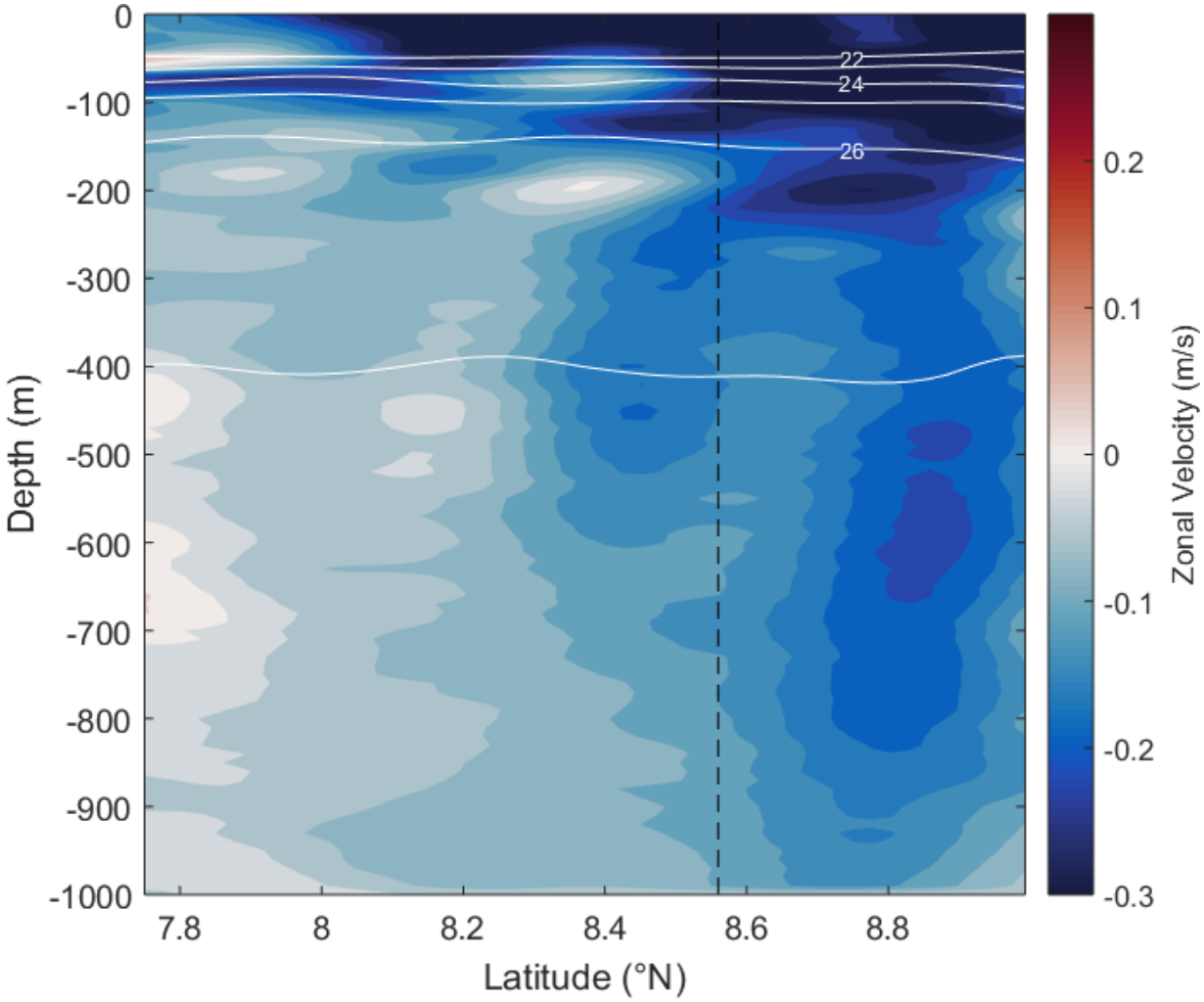

Figure 2.5: Example objectively mapped glider section along Line E, corresponding to Nov 29, 2015. Plotting scheme is the same as Figure 3, and the section is roughly concurrent in order to demonstrate the smoothing achieved by the objective map. Map length and time scales of 30 km and 14 days respectively were informed by the autocorrelation of zonal velocity (Fig. 2.4).

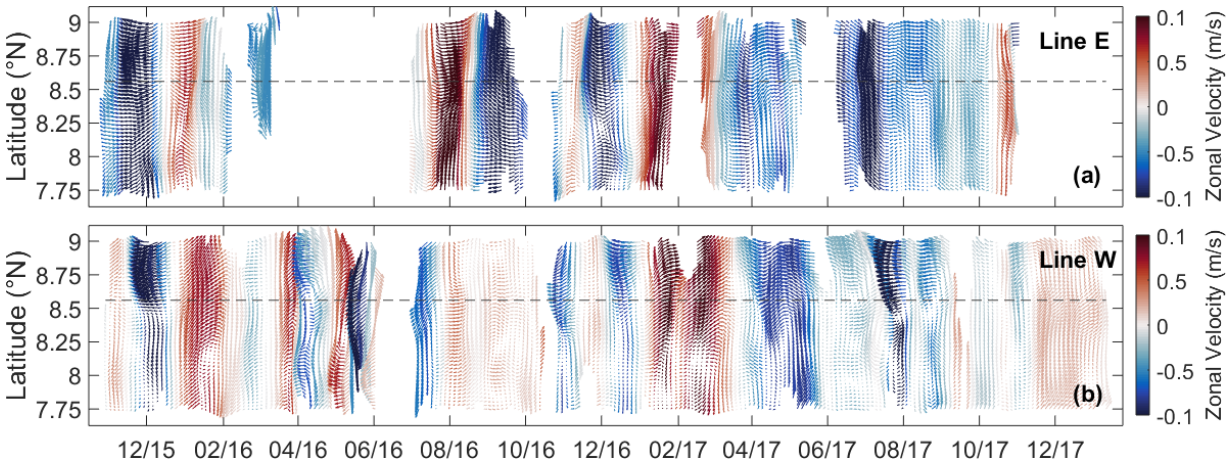

Figure 2.6: Time series of depth-averaged velocity vectors for each section, shaded by the depth-latitude average zonal velocity across each section. The northernmost extent of Velasco reef is marked with a horizontal dashed grey line. Velocity is mostly coherent along Line E (a), and exhibits greater latitudinal variance along Line W (b), especially south of the reef.

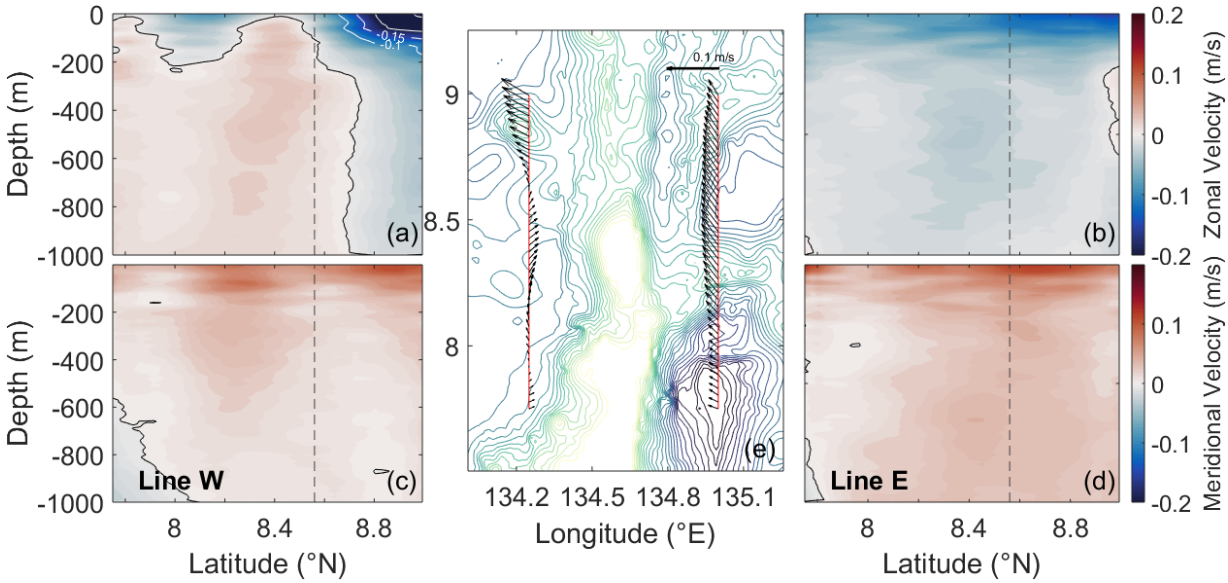

Figure 2.7: Mean sections of zonal (a,b) and meridional (c,d) velocity along Line E (b,d) and Line W (a,c), as well as mean depth-average velocity vectors plotted against bathymetry (e). The northernmost extent of Velasco reef is indicated with vertical dashed grey lines (a,b,c,d). Negative (positive) indicates eastward and southward (westward and northward) currents. Black contour lines are zero velocity. Velocities stronger than -0.1 are contoured in white, with .05 m s^{-1} contour interval. The flow is surface intensified and incident along Line E (westward, NEC). Therefore, Line E is upstream in the mean and Line W is downstream. The incident flow is strongest close to the reef extent and weakest to the south, indicative of topographic blocking. Downstream along Line W, there is acceleration north of the ridge and return flow in the lee of Velasco reef.

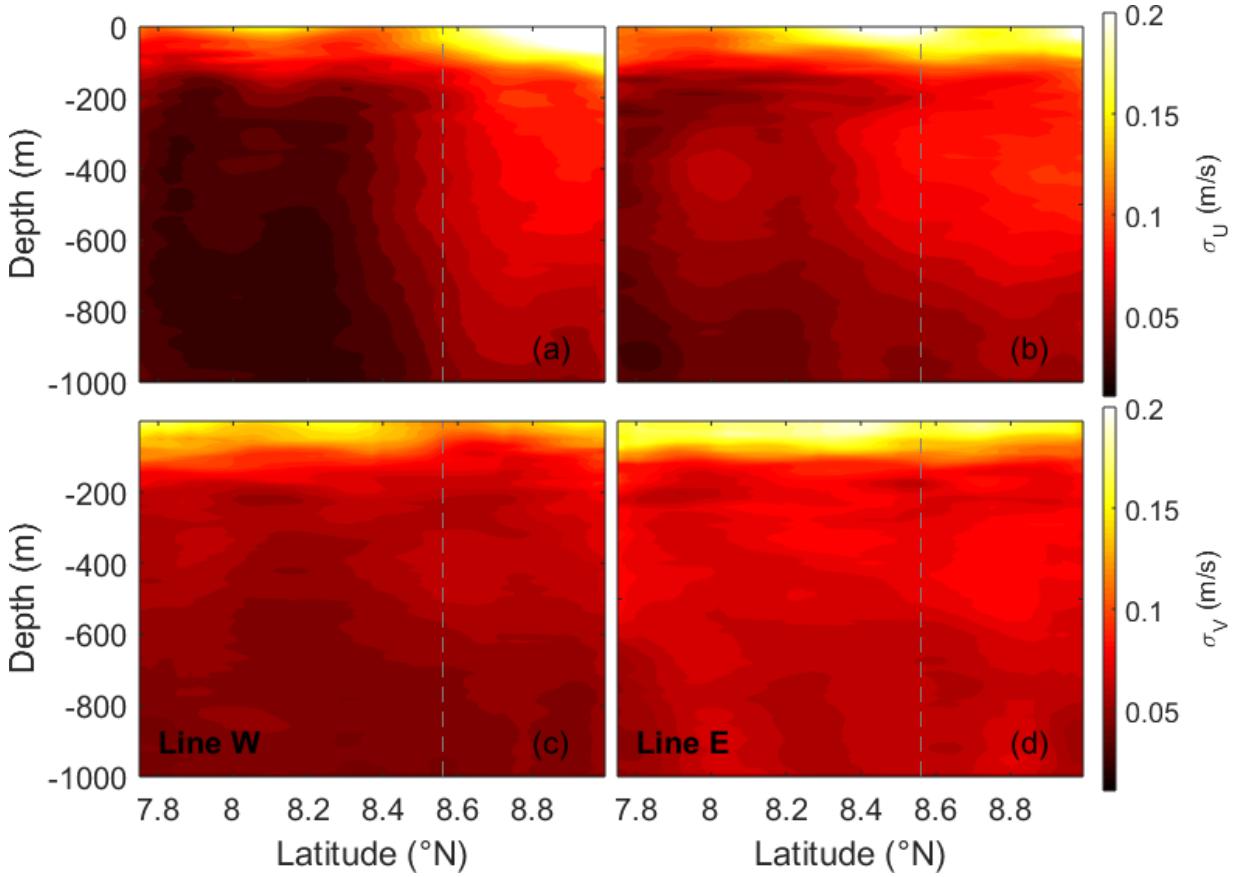

Figure 2.8: Zonal (a,b) and meridional (c,d) velocity variability (standard deviation) along Line W (a,c) and Line E (b,d). Line E is upstream in the mean, and Line W is downstream. The northernmost extent of Velasco reef is indicated (a,b,c,d) with vertical dashed grey lines. Variability is elevated in the surface, as well as north of Velasco reef in zonal velocity along both lines. Variability decreases in the lee.

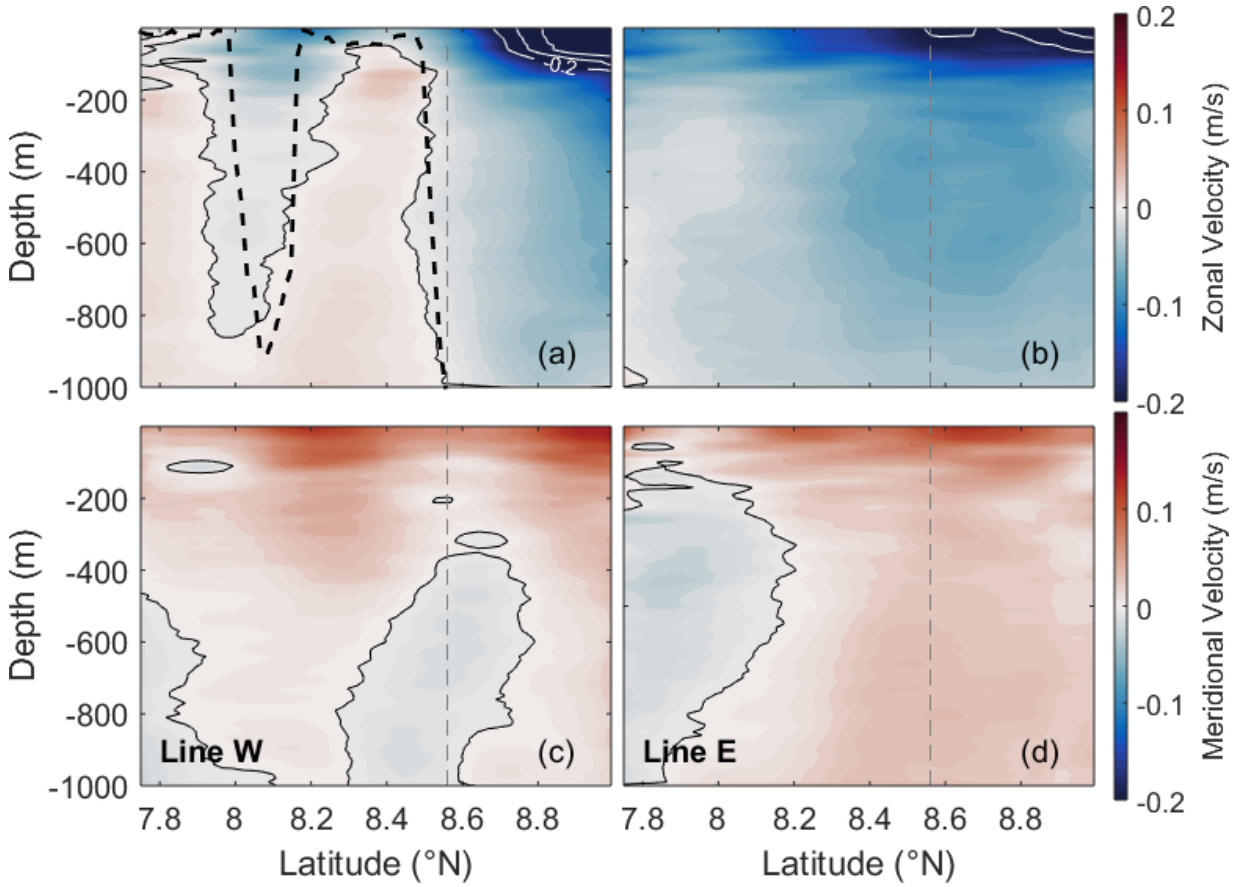

Figure 2.9: Mean sections of zonal (a,b) and meridional (c,d) velocity along Line E (b,d) and Line W (a,c) after selecting for westward flow. The color scheme and contour lines are as in Fig. 2.7. Line E is upstream during westward flow, and Line W is downstream. The dashed black line in (a) shows the bathymetry along 134.5° E, down the center of Velasco reef. Selecting for westward flow emphasizes topographic blocking upstream (d) and reveals a length scale in the wake that reflects the size of Velasco reef rather than the entire island of Palau, likely due to flow through the narrow channel at 8° N.

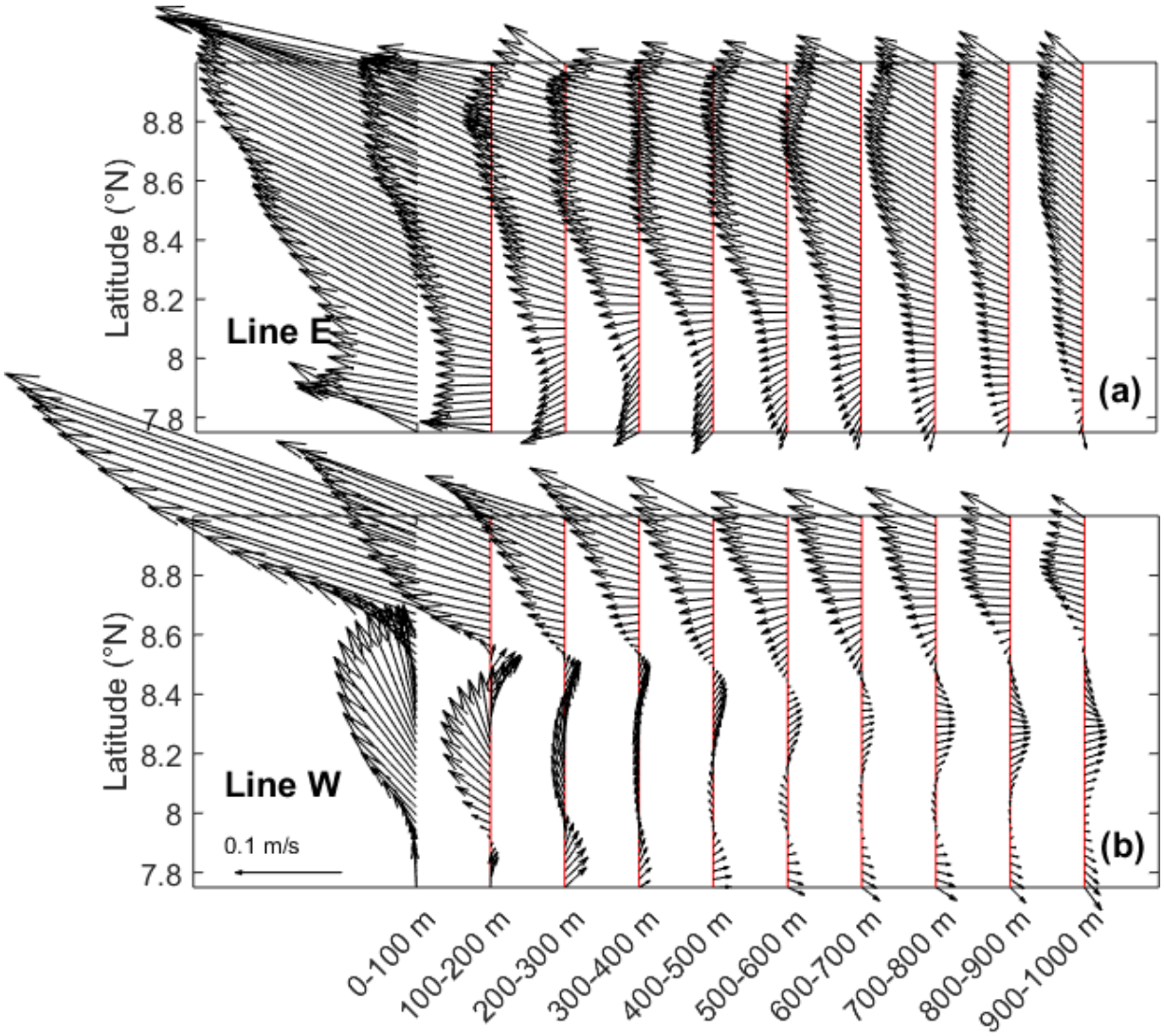

Figure 2.10: Time-mean depth-average velocity vectors in intervals of 100 m along Line E (a) and Line W (b), after selecting for westward flow. Line E is upstream during westward flow, and Line W is downstream. The wake exhibits a depth structure influenced by the topography as well as by the incident vertical shear.

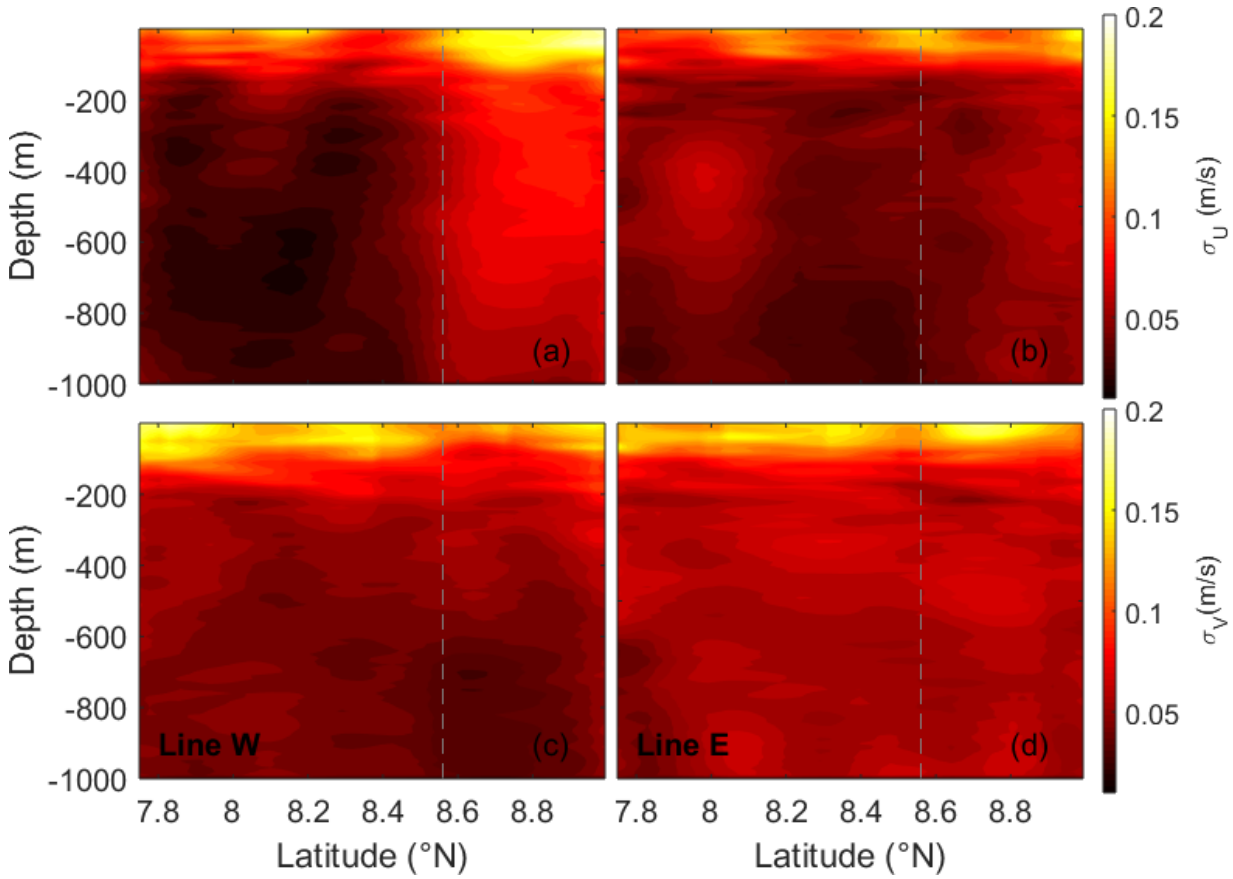

Figure 2.11: Zonal (a,b) and meridional (c,d) velocity variability along Line W (a,c) and Line E (b,d) after selecting for westward flow. Line E is upstream during westward flow, and Line W is downstream. The patterns in variability are similar to the total mean (Fig. 2.8), however subthermocline zonal velocity variability is only elevated downstream and north of the reef (grey dashed line).

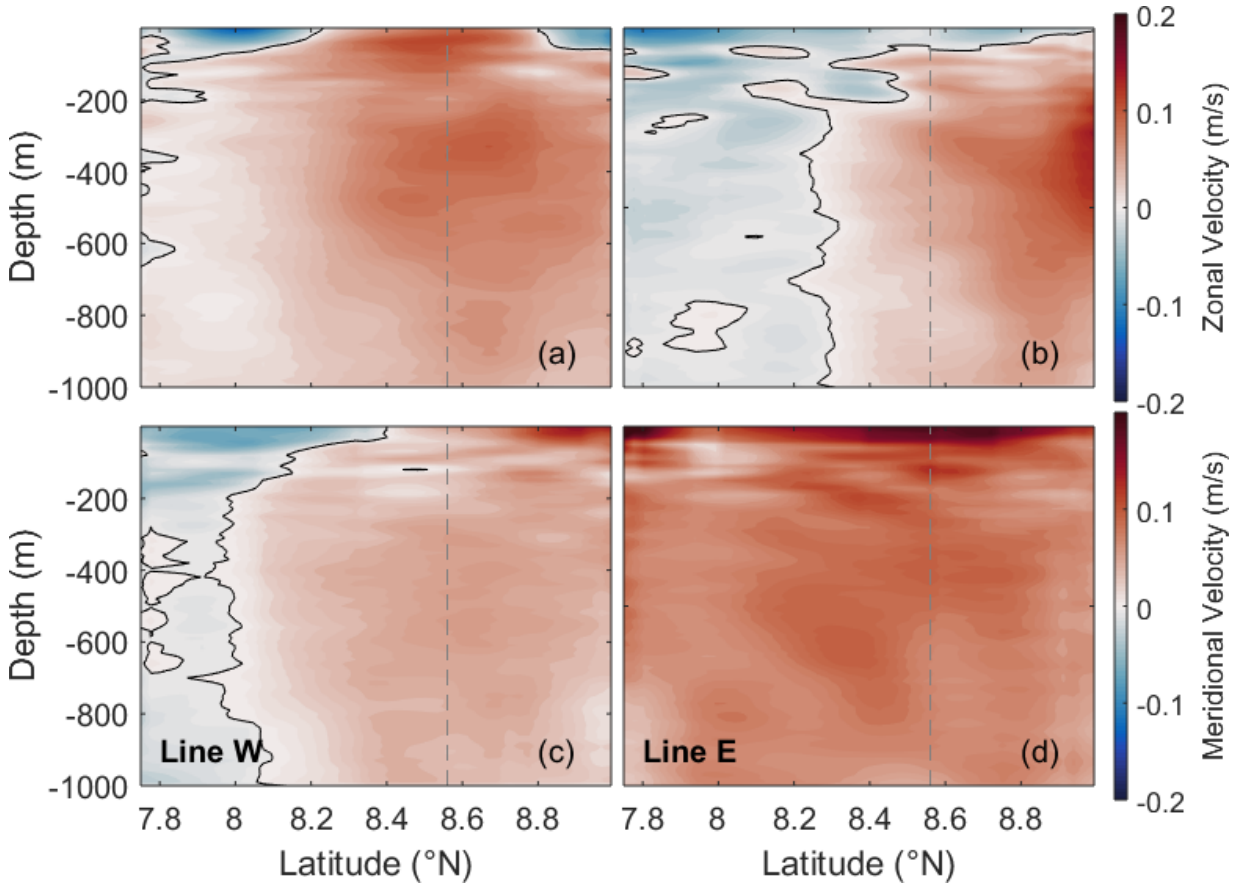

Figure 2.12: Mean sections of zonal (a,b) and meridional (c,d) velocity along Line E (b,d) and Line W (a,c) after selecting for eastward flow. Line W is upstream during westward flow, and Line E is downstream. The color scheme and contour lines are as in Fig. 2.7. Both the incident flow and wake are asymmetric to westward flow. Despite selecting for depth-averaged eastward flow, westward currents persist at the surface (a,b). While zonal velocity downstream (b) seems to suggest return flow, the strong northward component of velocity (d) suggests that the flow along Line E may originate from the south instead of the west.

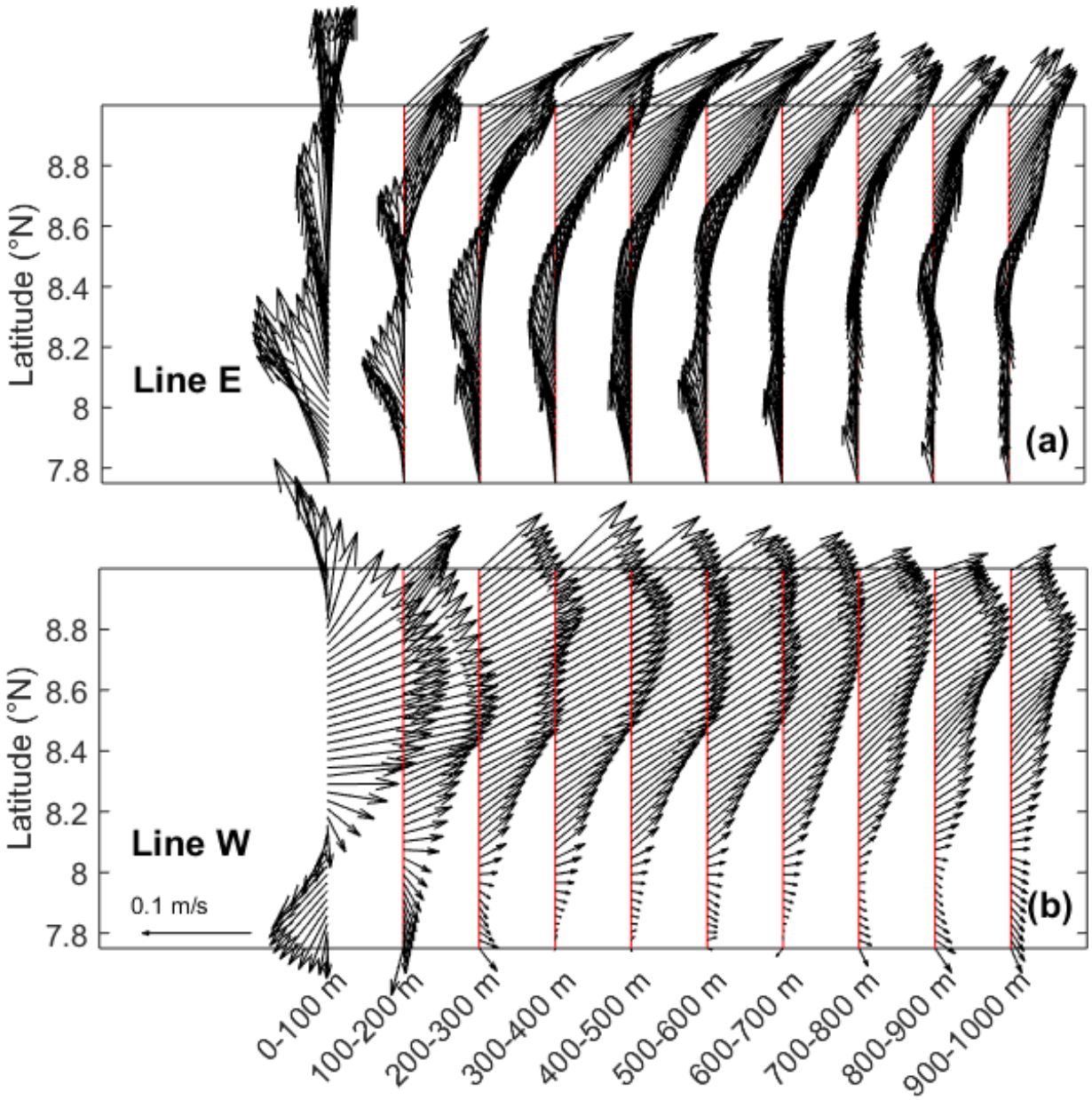

Figure 2.13: Time-mean depth-average velocity vectors in intervals of 100 m along Line E (a) and Line W (b), after selecting for eastward flow. Line W is upstream during westward flow, and Line E is downstream. The surface 200 m emphasize the convergence of flow from the south-east along Line E and from the west along Line W, resulting in the persistent signature of westward flow in the mean.

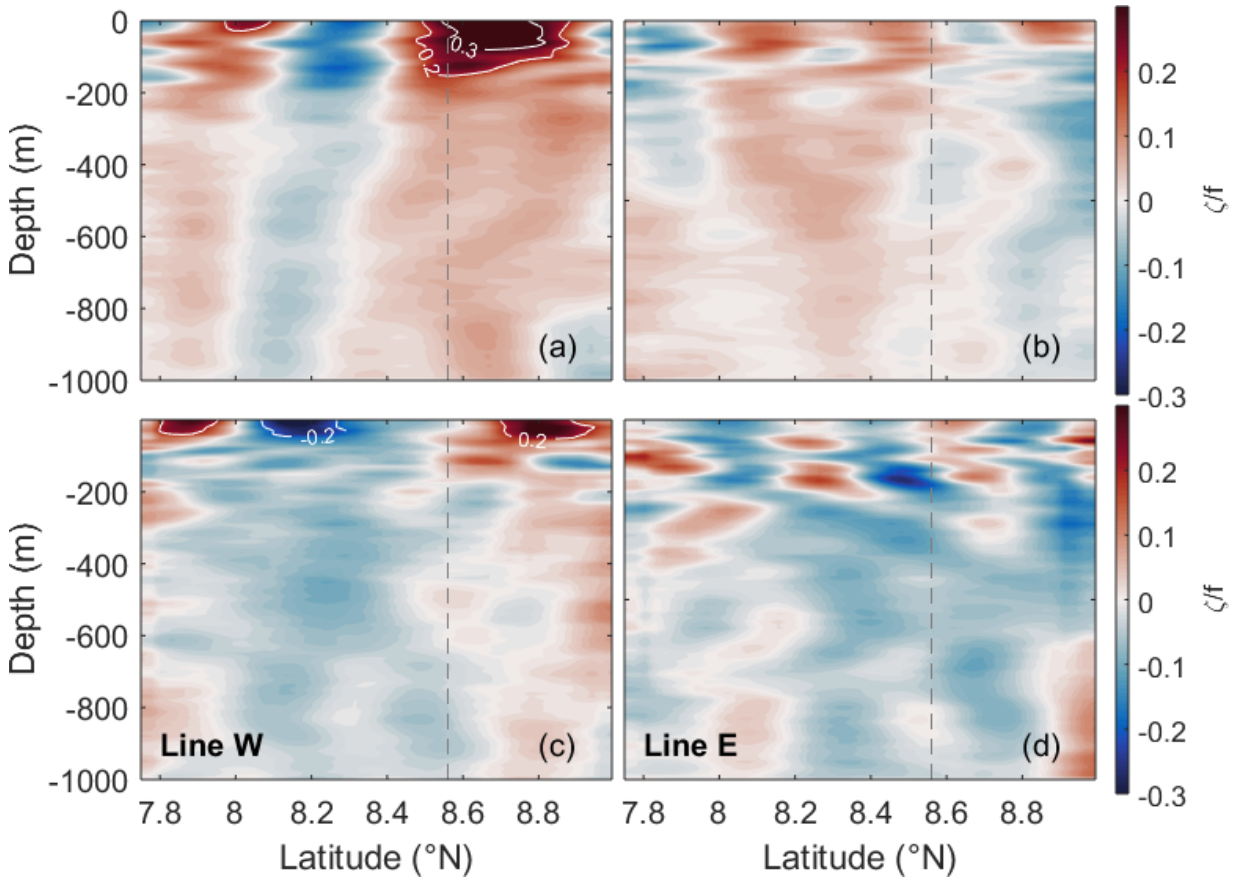

Figure 2.14: Mean sections of normalized vorticity (Rossby number, Ro) calculated from the meridional gradient of zonal velocity ($\zeta = dU/dy$), during westward flow (a,b) and eastward flow (c,d) along Line W (a,c) and Line E (b,d). |Ro| greater than 0.2 have been contoured in white, with an interval of 0.1. The grey dashed line is the maximum latitude of Velasco reef. During westward flow, Line E is upstream and Line W is downstream. During eastward flow this is reversed. Ro upstream during westward flow (b) are on average less than ± 0.1. Downstream of the reef, Ro increases substantially to over $0.3f$ in the surface (a), suggesting there are times when ageostrophic effects are important. During westward flow vorticity has latitudinal structure throughout the water column. During eastward flow the Ro in the wake is low (< 0.1 on average) and there is no symmetric vorticity signature, except in the surface (c) where westward flow persists.

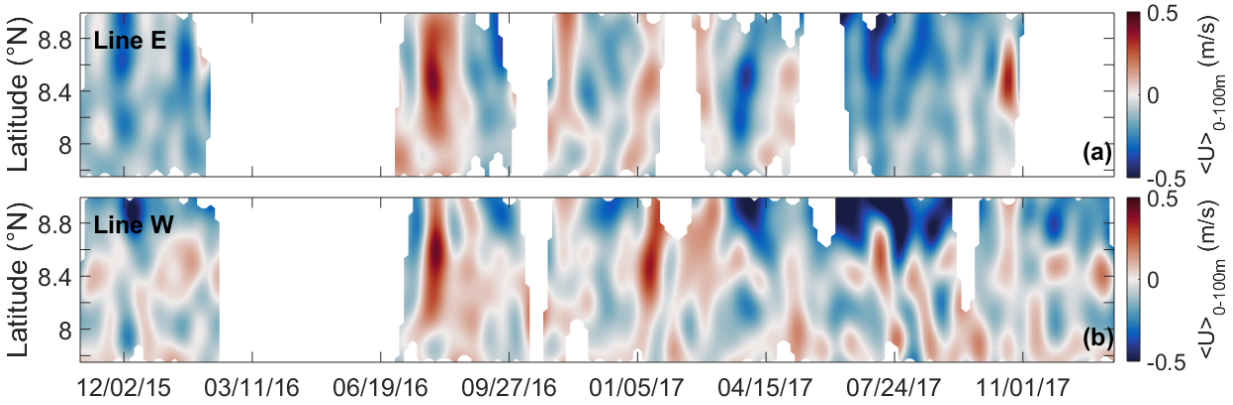

Figure 2.15: Hovmoller diagrams of shallow (0 - 100 m) zonal velocity along Line E (a) and Line W (b). Return flow in the lee of the reef appears as an intermittent band of eastward velocity around 8.4° N along Line W. While there is high frequency (i.e. days) fluctuations in the current of moderate magnitude, the time series is dominated by low-frequency (i.e. weeks-months), highly energetic events.

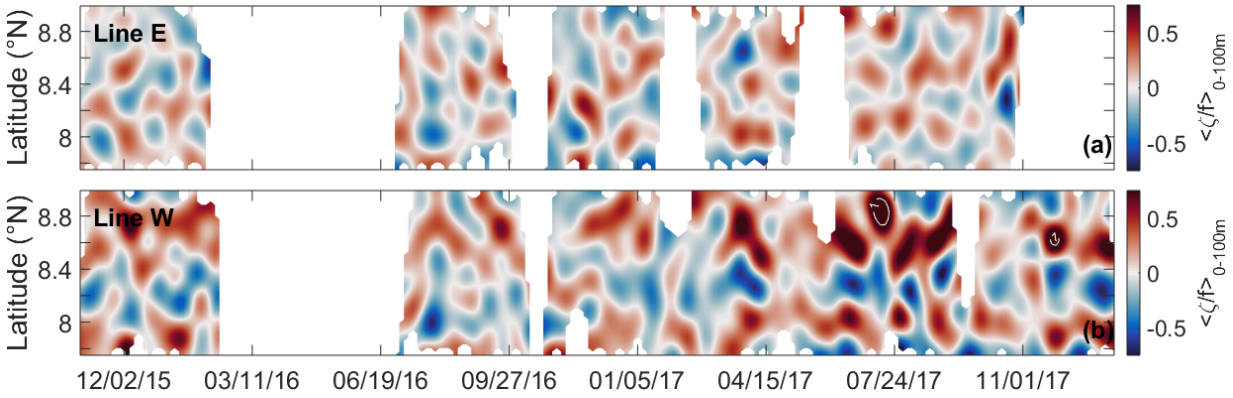

Figure 2.16: Hovmoller diagrams of shallow (0 - 100 m) normalized vorticity (Rossby number) along Line E (a) and Line W (b). The low frequency, energetic events in zonal velocity (Fig. 2.15) have important implications for the vorticity. For example, anomalously strong westward flow in July 2017 corresponds to Ro exceeding 1 in the surface wake (b, white contour).

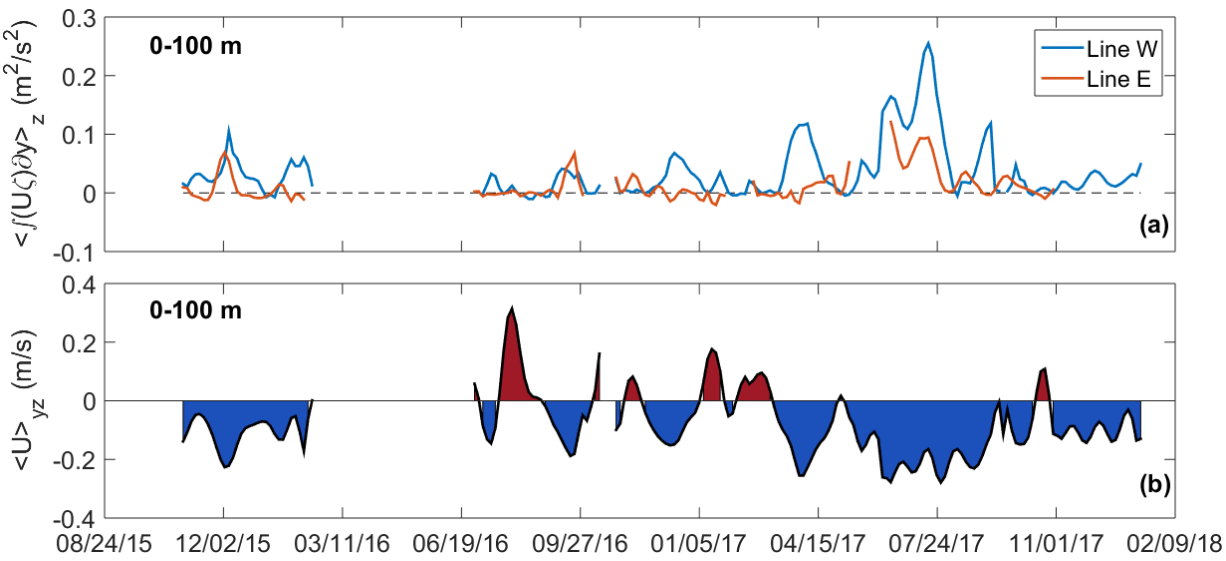

Figure 2.17: Depth-average, section integrated vorticity flux (ζU) along both lines (a), as well as depth-and-latitude average zonal velocity north of 8.2° N along Line E (b). Periods of sustained westward flow correspond to elevated vorticity flux downstream, emphasizing the role the island plays in vorticity production. However, periods of weak and intermittent westward flow fail to contribute substantially to the vorticity production.

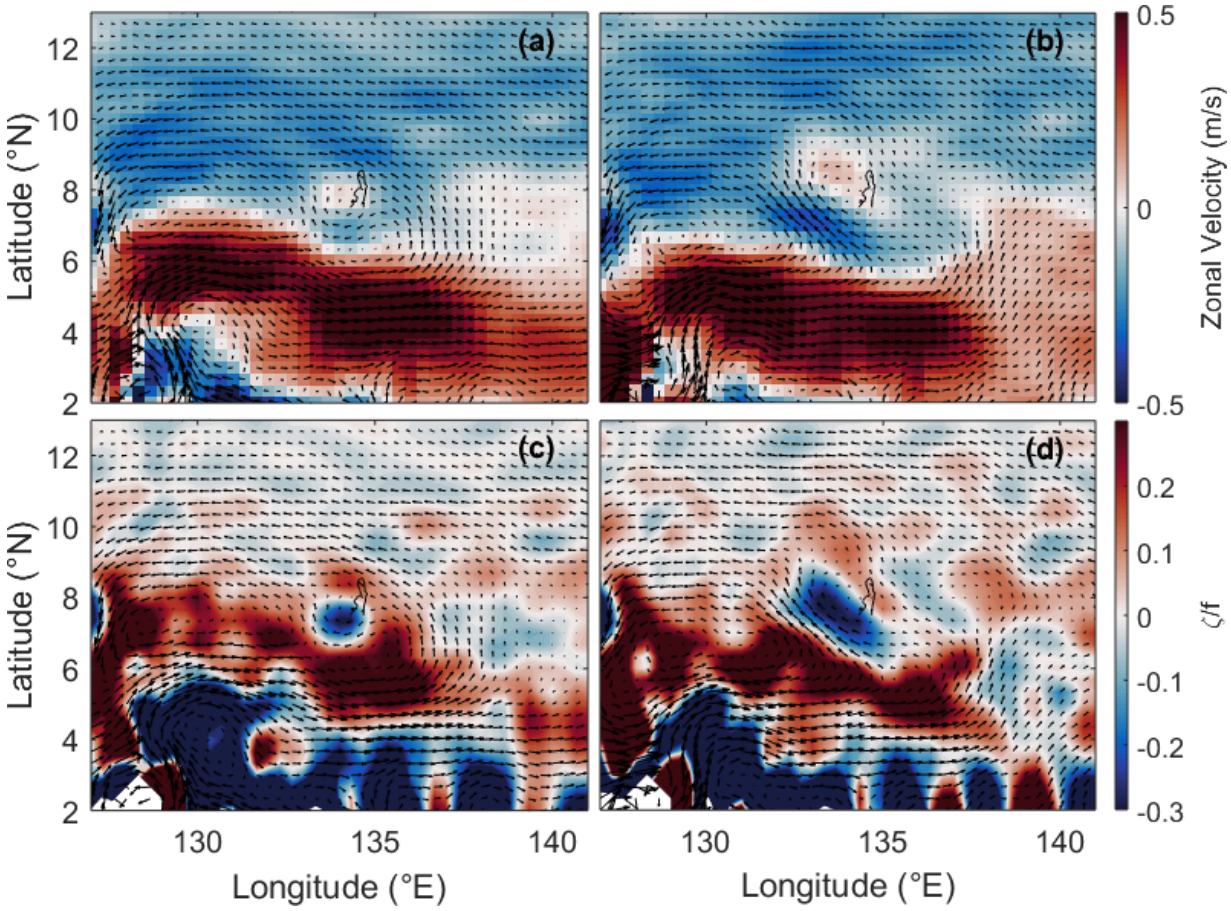

Figure 2.18: OSCAR surface currents averaged over the observational periods corresponding to westward (a,c) and eastward flow (b,d) provide regional context for the asymmetries observed by the glider during flow reversals. Black arrows are surface current vectors, plotted over filled contours of zonal velocity (a,b) and normalized vorticity, or Rossby number (c,d). Depth-average westward (eastward) flow as seen by the glider is characterized by a more northward (southward) NECC in the vicinity of Palau. These regional differences impact the local flow around Velasco, likely contributing to the observed asymmetries.

Chapter 3

Broadband Submesoscale Vorticity Generated by Flow Around an Island

An array of moorings deployed off the coast of Palau is used to characterize submesoscale vorticity generated by broadband upper ocean flows around the island. Palau is a steep-sided archipelago lying in the path of strong zonal geostrophic currents, but tides and inertial oscillations are energetic as well. Vorticity is correspondingly broadband, with both mean and variance $O(f)$ in a surface and subsurface layer (where f is the local Coriolis frequency). However, while sub-inertial vorticity is linearly related to the incident sub-inertial current, the relationship between super-inertial velocity and super-inertial vorticity is weak. Instead, there is a strong non-linear relationship between sub-inertial velocity and super-inertial vorticity. A key observation of this study is that during periods of strong westward flow, vorticity in the tidal bands increases by an order of magnitude. Empirical orthogonal functions (EOFs) of velocity show this non-stationary, super-inertial vorticity variance is due to eddy motion at the scale of the array. Comparison of kinetic energy and vorticity timeseries suggest that lateral shear against the island varies with the sub-inertial flow, while tidal currents lead to flow reversals inshore of the recirculating wake and possibly eddy shedding. This is a departure from the idealized analog typically drawn on in

island wake studies: a cylinder in a steady flow. In that case eddy formation occurs at a frequency dependent on the scale of the obstacle and strength of the flow alone. The observed tidal formation frequency likely modulates the strength of submesoscale wake eddies and thus their dynamic relationship to the mesoscale wake downstream of Palau.

3.1 Introduction

Vorticity wakes are often generated by energetic ocean currents flowing past islands. These wakes are of interest to the oceanographic community because they can extract momentum from the incident flow and modify water masses on short time and spatial scales. For sufficiently strong currents, eddies form and separate from the island (Heywood et al., 1990). Energetic, unstable wake eddies may dissipate locally and increase mixing close to the island (Chang et al., 2013). More stable eddies can transport isolated water masses hundreds to thousands of kilometers downstream (Caldeira et al., 2014). This variability is not well constrained in part due to non-linearities associated with the production of vorticity. The broadband frequency content of geophysical flows introduces additional variability and presents a challenge in characterizing island wakes. In this study, a year of moored current data is used to calculate submesoscale vorticity near the northern end of Palau, where flow separation has been observed (MacKinnon et al., 2019; Wijesekera et al., 2020). The high temporal resolution of the data enables quantification of vorticity on timescales of hours to months, and insight into the physical processes of wake generation due to broadband flows.

The classic paradigm for vorticity wakes is a circular cylinder in steady, unidirectional flow (Kundu and Cohen, 1990). Vorticity is generated by a no-slip boundary condition and flow separation leads to recirculation in the wake. Eddies are shed when oppositely signed shear layers across the wake interact, interrupting the supply of vorticity (Bearman, 1984). Downstream the wake is non-linear and analytic solutions are not available. However, two characteristics are

remarkably predictable: the frequency of eddy shedding and their downstream configuration. The former is given by the Strouhal number, St = $f_e(L/U)$, a non-dimensional parameter with an empirically determined dependence on the Reynolds number, Re = UL/ν (Roshko, 1954). Here f_e is the (non-angular) eddy shedding frequency, U is the unperturbed upstream velocity, L is the diameter of the cylinder and ν is the kinematic viscosity. The configuration of wake eddies satisfies a constant spacing ratio similar to a von Karman Vortex Street (VKVS), (von Karman, 1912). These characteristics persist even for turbulent wakes with high Reynolds numbers (Bearman, 1969).

Observational studies have routinely found eddies in the wakes of islands resembling idealized VKVS wakes (e.g. Barkley, 1972; White, 1973; Heywood et al., 1990; Bowman et al., 1996; Herandez-Leon, 1991; Aristegui et al., 1994; Zheng et al., 2008; Chang et al., 2013; Caldeira et al., 2014). This similarity has motivated oceanographers to use the cylinder paradigm to extrapolate observations with limited temporal and spatial resolution to a more complete picture of the wake (e.g. Heywood et al., 1990; Teague et al., 2002). However, the broadband content of real geophysical flows challenges the utility of this comparison. Basin-scale geostrophic flows are often considered quasi-steady, but typically advect mesoscale features with significantly shorter timescales. Tides and inertial currents can also be energetic, especially in shallow coastal regions. Many studies examining oscillatory flows past small-scale headlands have shown that the relative strengths of different flow components, as well as the geometry of the headland, dictate the dynamics in the wake (Pawlak et al., 2003; Pattiaratchi et al., 1986; Signell and Geyer, 1991). How these fine scale, high-frequency processes relate to larger scale island wakes is an outstanding question in the field.

This study is part of a large field campaign designed to address this gap by observing the wake generated by an island over a wide range of spatial and temporal scales. The Office of Naval Research department research initiative 'Flow Encountering Abrupt Topography' (FLEAT) combines current observations from ship surveys, moorings, autonomous vehicles and remote

sensing to characterize the wake generated by Palau, a steep sided, meridionally elongated mesoscale archipelago lying in the path of two major geostrophic currents in the tropical North Pacific. Here 'mesoscale' means on the order of the Rossby radius of deformation, which is $O(100)$ km in the region (Chelton et al., 1998). A panoply of synoptic observations has captured wake eddies around the island from topographic to mesoscales. Rapid repeat ship surveys around the northern and southernmost ends of Palau observed flow separation around small-scale headlands and the subsequent generation of energetic eddies $O(1)$ km during strong tidal flows with Ro up to $O(10^2)$ (MacKinnon et al., 2019; Johnston et al., 2019). Here and throughout this manuscript, Ro is the Rossby number, a non-dimensional ratio of relative to planetary vorticity (Ro = ζ/f). At $O(10)$ km, repeat box-surveys around the northern end of Palau sampled larger scale recirculation with Ro $O(1)$ during strong north-westward flow (Wijesekera et al., 2020). In another study, ship surveys revealed the presence of eddies 20-40 km in scale and with Ro $\sim O(1)$ downstream of the island concurrent with strong eastward flow (Rudnick et al., 2019). Additional larger scale wake eddies were observed with HF radar to the east of Palau with similar vorticity during a different period of eastward flow (Merrifield et al., 2019). Finally, repeat glider sections over 2.5 years show persistent island-scale ($0(100)$ km) recirculation to the west of the island with Ro $\sim O(0.1–1)$ which develops in response to westward low-frequency geostrophic flow (Zeiden et al., 2019).

The goal of this study is to expand upon these synoptic observations by quantifying the temporal variability of vorticity close to the generation point at the northern end of Palau. While a few of the studies cited above included timeseries of vorticity, these have predominantly been estimates over limited time periods concurrent with the surveys. In this study, 11-months of sustained current observations from moorings enables characterization of vorticity on super-tidal to sub-inertial timescales. The moorings were deployed at variable distances within 40 km of the northern end of the island. The full array is used to characterize the flow field, while a $\sim$7 km triangular array close to the topographic separation point gives the vorticity at that scale. A

key observation of this study is that periods of strong low-frequency flow coincide with elevated high-frequency vorticity variance, particularly in the tidal bands. This tidal band vorticity is not simply related to tidal band kinetic energy, which suggests a degree of non-linearity in the vorticity generation process.

This paper is organized as follows: section 3.2 provides details on the oceanographic context, data collection and analysis methods in this study, section 3.3 presents results characterizing first the flow field around the island, followed by vorticity, section 3.4 discusses the vorticity generation process and implications for the wake, and section 3.5 provides a summary and conclusion.

3.2 Data and Methods

3.2.1 Oceanographic Setting

Palau is a meridionally elongated archipelago in the western North Pacific. The archipelago is comprised of over 300 small islands which are connected by a submerged reef extending ~ 200 km from its northern to southern end. In this manuscript, when we refer to the 'island' of Palau we mean this submerged reef. Palau lies in the path of two opposing geostrophic currents. At the northern end, the North Equatorial Current (NEC) flows between 8 – 17 $^{\circ}$N with maximum speeds of 0.5 ms^{-1} (Qiu and Lukas, 1996; Schönau and Rudnick, 2015). On average, the NEC is westward and surface intensified, but extends down to the pycnocline centered at about 150 m depth close to Palau (Schönau and Rudnick, 2015). Below the pycnocline there are weak eastward undercurrents, the North Equatorial Undercurrents (NEUCs), with average current speeds less than 0.1 m/s (Qiu et al., 2013). Transport in these undercurrents is correlated with transport of the NEC (Schönau and Rudnick, 2015), although this relationship weakens downstream of Palau (Zeiden et al., 2019). At the southern end, the North Equatorial Counter-Current (NECC) flows eastward at variable latitude between the equator and 7 $^{\circ}$N with maximum currents that can

exceed 1 ms^{-1} (Hsin and Qiu, 2012).

Data presented in this manuscript were collected at the northern end of Palau, where on average the NEC and southernmost NEUC are incident on the archipelago. Here the steep-sided island boasts bathymetric gradients up to 45°, culminating in a 40 km wide subsurface reef called Velasco. The reef rises to just under 20 m around the rim and blocks the incident flow almost completely to the surface. A concurrent FLEAT study quantified the mean mesoscale currents around Velasco and their variability using repeat glider surveys (Zeiden et al., 2019). Mean incident currents were westward and surface intensified (~ 0.2 ms^{-1} within the upper 200 m) with eastward return flow in the lee of Velasco. Significant variability on sub-inertial timescales was likely due to the mesoscale eddy field advected westward by the NEC (Schönau and Rudnick, 2015; Hsin and Qiu, 2012). Strong northward currents occurred on occasion due to recirculation of the NECC, likely spurred by westward propagating Rossby waves (Heron et al., 2006).

3.2.2 Dataset Description

Fourteen moorings were deployed around Velasco over an 11 month period from April 2016 – May 2017 (Figure 3.1). The array was designed to sample high-frequency currents with adequate spatial resolution to resolve their sub-mesoscale structure around the island. A sub-selection of these moorings were used in this study. Four far-field (greater than 10 km from the reef) deep-water moorings were used to characterize the ambient flow field (F1, M1, M2 and M5 deployed in 3390, 2600, 2610 and 3690 m, respectively). Three near-field (within 10 km) moorings were used to calculate vorticity, F2, F3 and F4. These moorings were deployed in 1515, 1666 and 880 m, respectively. Each had two ADCPs mounted around 60 m depth; an upwards looking 300 kHz RDI Work Horse Monitor and downwards looking 75 kHz Work Horse Long Ranger. F2 had an additional upwards looking Long Ranger deployed at 770 m and a downwards looking Work Horse at 1470 m. F3 had a downwards looking Long Ranger at 760 m, and a downwards looking Work Horse at 1570 m. F4 had one additional upwards looking

Long Ranger at 880 m. These moorings form an equilateral triangle $\sim$7 km scale and centered 5 km from the northernmost promontory of Velasco (Fig. 3.1c). Moorings were each equipped with a series of thermistors, CTDs and ADCPs. In this study we examine the ADCP data. F moorings each have ADCP coverage of over 80% of the water column at their respective depths and M moorings have coverage from the surface to 700 m. For all deep-water moorings, upwards looking ADCPs deployed near the surface achieved a vertical resolution of 4 m and a minimum temporal resolution of 16 minutes, enough to resolve tidal motions. Velocities were smoothed and interpolated to a 10-m by 1-hour grid.

To examine the depth-dependence of vorticity around Palau we perform a layer-average in the surface (0–100 m) and sub-pycnocline (hereafter subsurface, 300–400 m). The surface layer was chosen to capture the variability of the NEC, which extends through the base of the pycnocline but decays substantially below 100 m (Schönau and Rudnick, 2015). The subsurface layer similarly corresponds to the mean depth of the peak NEUCs velocities at this latitude, well below the pycnocline. An example of zonal and meridional velocity in the upper 1400 m during a period of westward surface flow at F3 gives an idea of the temporal and vertical scales included in these averages (Figure 3.2). Vertically sheared geostrophic currents have length scales of $O(100)$ m in the surface (NEC) and hundreds of meters in the subsurface (NEUCs). Energetic tides can lead to flow reversals despite the strong geostrophic westward flow. There is likely additional vertical variability on finer scales which has been filtered by our gridding process. The surface layer encompasses the mixed layer and the upper half of the pycnocline, although ADCP data in the surface 10 m were often discarded due to side lobe contamination. The mean mixed layer depth (MLD) during the observation period was 40 m, with a standard deviation of 12 m (obtained with CTD data from concurrent glider surveys). Correlation values between velocity at any two depths across the MLD are no less than 0.5, and mostly greater than 0.8, despite a potential dynamic shift across the base of the mixed layer. Correlation values are highest in the semi-diurnal band ($R \geq 0.7$), but also strong in the diurnal band ($R \geq 0.6$). Correlation values are

lowest in the inertial band, most likely due to inertial oscillations confined to the mixed layer (R = 0.5). Nonetheless, the main results of our analysis are not sensitive to varying the base of the surface layer from 50 to 150 m. The subsurface layer is well below the pycnocline and above the bottom boundary. Correlation values within this layer are above 0.8 in all bands due to the large vertical length scales of the NEUC and tide, and absence of energetic mixed layer currents. Correlation values between velocity at any depth level in the surface and subsurface layer are less than 0.3, which supports treating them independently.

In this manuscript we often refer to sub-inertial low passes of each timeseries (bold lines overlaying each timeseries in all figures). These low passes are obtained by convolving a 10-day Hanning window with the timeseries. Although not plotted, we also refer to super-inertial timeseries. These are obtained by subtracting a 2-day Hanning window filtered timeseries from the full timeseries.

3.2.3 Vorticity Calculation

The spatial gradients necessary to compute the vertical component of relative vorticity at the center of a triangular array can be approximated by fitting a plane to zonal and meridional velocity at each time-step and calculating their slopes (i.e. $\zeta = v_x - u_y$). Equilateral triangles provide the lowest error estimate of spatial gradients via this method (Davies-Jones, 1993). This is intuitive because acute/obtuse triangles sample spatial gradients over different length scales in each direction and therefore give an over/under-estimate of the magnitude of vorticity at the average scale of the array. The triangle formed by F2, F3 and F4 is nearly equilateral, with side lengths of 5.87, 5.82 and 5.87 km (in the clockwise direction starting at F2, Fig.3.1). Together they inscribe a circle 6.8 km in diameter.

The implicit assumption when using a plane-fit to calculate vorticity is that the observed velocity variability is due to spatial gradients which are near the scale of the array. The error associated with this assumption is dependent on the relative energy at spatial scales smaller

than the triangle. Without knowing the actual velocity field, it is difficult to estimate this error (Davies-Jones, 1993). While KE spectra in the open ocean are typically red, it is unclear how proximity to Palau may impact this distribution. For example, MacKinnon et al. (2019) observed the generation of tidal eddies $\sim$1 km in scale during ship surveys around the northern tip of Velasco. If these eddies were to propagate away from their generation site and cross a single mooring in the array, it would be aliased as vorticity variance at the scale sampled by the triangle. To better understand the spatial structure of currents included in our vorticity estimate, we perform an Empirical Orthogonal Function (EOF) analysis of the velocity timeseries in each layer.

3.2.4 Empirical Orthogonal Function Analysis

Previous studies have used empirical orthogonal functions (EOFs) to identify the statistical modes with maximum covariance across an array (Rudnick and Davis, 1988; Rudnick and Weller, 1993; Fischer et al., 2002). In this study we calculate EOFs of velocity across the triangular array. The EOFs are orthogonal eigenvectors of the data covariance matrix. Each describe a certain percentage of the total variance, given by their eigenvalues. The projection of each EOF back onto the data gives its time-dependent amplitude. While EOFs should not automatically be interpreted as real physical modes, there is no more efficient way to describe the velocity variance. Typically, velocity time series are reconstructed using only the most energetic EOFs. In this study we are specifically concerned with calculating vorticity, so we also consider the Okubo-Weiss value (OW) of each EOF. OW is a measure of the relative magnitude of strain and vorticity and is given by $\sigma^2 - \zeta^2$, where σ^2 is the magnitude of horizontal strain given by $(u_x - v_y)^2 + (v_x + u_y)^2$ and ζ^2 is the enstrophy (Okubo, 1970; Weiss, 1991). This value springs from approximating the horizontal flow field around a singular point as a power series, where the first order terms are a function of local linear velocity gradients. The sign of OW determines whether the flow field follows spiral trajectories (negative OW) or nodal/saddle trajectories (positive OW). Regions of negative OW are frequently used to identify coherent vortices in modeling and satellite data (e.g.

D'Addezio et al., 2020).

To minimize the impact of fine-scale features on the vorticity calculation, we select for currents with spatial scales close to that of the array. First we identify the EOFs in each layer which describe either currents in phase across the array (i.e. in the same direction), or with vortical structure near the array scale (i.e. currents out of phase, but with a clear sense of rotation characterized by negative OW). We then 'reconstruct' the velocity timeseries by multiplying these EOFs by their respective amplitudes and adding those timeseries. We find that the subsequent reconstructed velocity timeseries retain 94% and 89% of the total velocity variance in the surface and subsurface layers, respectively. We then proceed to analyze the vorticity obtained via plane-fit to these velocity timeseries with confidence that our estimates are not significantly aliased by fine-scale motions. Further details of the EOFs are examined in the following section, as well as their individual contributions to the vorticity.

3.3 Results

We begin by describing the broad-band flow around Velasco using the full array of moorings. We follow with a detailed analysis of the vorticity generated at the northernmost promontory where flow separation has been both predicted and observed (Simmons et al., 2019; MacKinnon et al., 2019; Wijesekera et al., 2020). The focus of this analysis is a $\sim$7 km triangular array. We examine the vorticity timeseries and compare them with the velocity timeseries. We then examine the EOFs in an effort to understand the structure of currents which contribute to the vorticity. Finally, we present scalograms of vorticity to quantify its time-varying spectral content.

3.3.1 Broad-band Currents around Palau

Surface currents around Velasco are broadband in frequency, as seen in timeseries of surface velocity (0–100 m) from a selection of the moorings counterclockwise around the reef;

M2, M5, F3, F1 and M1 (Figure 3.3). In the mean, M2 is upstream of Velasco and M1 is downstream. Four strong sub-inertial current events dominate the variance with velocities of $\sim$0.5 ms^{-1}. Here and throughout the text, we will often refer to e.g. 'eastward flow' when discussing sub-inertial currents. Strong eastward flow occurs in late July and strong westward flow in September and December. Note that the strong northward component which accompanies westward flow is the result of topographic blocking. Using repeat glider surveys east and west of Palau, Zeiden et al. (2019) found the time-mean incident westward flow diverges at $\sim$ 8.2 $^{\circ}$N. The current above that latitude gains a strong northward component as it circumvents the island. This effect can be seen clearly in average surface velocity vectors during the westward flow event in December (Fig.3.1b). A fourth event in early March begins as strong northward flow on the eastern side of the island (at M2 and M5) and then transitions to westward flow. Sub-inertial velocities are well correlated across the array (e.g. R $\geq$ 0.6 between F3 and the other moorings), suggesting they have spatial scales of at least 60 km. This is consistent with glider observations which indicate that sub-inertial currents often have spatial scales exceeding 100 km. Weak downstream currents are further evidence of topographic blocking. For example, the strong eastward current in July appears in velocity data at M1, F1, F3 and M5 but does not appear downstream of Velasco at M2 (orange shaded boxes in Fig. 3.3). Similarly, currents are negligible downstream at M1 during westward flow (blue shaded boxes in Fig. 3.3). Thus, topographic blocking reduces the strength of large-scale, sub-inertial currents by almost an order of magnitude.

Sub-inertial currents are weaker in the subsurface layer (300–400 m), with strong events reaching $\sim$ 0.25 ms^{-1} (Figure 3.4). One sustained westward flow event spanning August and September 2016 stands out in the timeseries of M2 and M5 (orange shaded boxes in Fig. 3.4), but otherwise high-frequency currents dominate the variance. Note that although the northward current is actually stronger than the zonal component here, concurrent glider observations show the incident large-scale sub-inertial flow is westward during this time (not shown). None of the

five sub-inertial current events observed in the surface layer have a signature at depth, consistent with a weakened relationship between the NEC and NEUC close to the island (Zeiden et al., 2019). Correlation in space is divided between moorings to the east and west of Velasco (Fig. 3.4). For example, sub-inertial zonal currents at M5 are strongly correlated with those at M2 (both east of Velasco, R = 0.7) but are uncorrelated with those at F1 (west of Velasco). Interestingly, sub-inertial subsurface velocity at the tip of the reef is correlated with currents both to the east and west of Velasco ($R > 0.6$ between F3 and all other moorings).

In both layers, high-frequency currents are energetic enough to induce flow reversals except during the strongest sub-inertial current events. Their contribution to the total velocity variance is quantified with surface and subsurface kinetic energy spectra at the moorings in the triangular array (Figure 3.5a and 3.5b). Subsurface KE variance is higher at F4 because it is shallower and therefore has stronger depth-mean stratification. Spectra are red with broad peaks around the local inertial (f) frequency, and sharp peaks at the diurnal (D1) and semi-diurnal (D2) frequencies. These bands account for 10%, 9% and 12% of the total variance in the surface layer, and 12%, 14% and 32% in the subsurface layer. The greater percentage of KE variance contained in these bands at depth ($> 50\%$) reflects the weak sub-inertial currents there.

At the surface, tidal currents are highly irregular. A scalogram of array-mean surface KE shows sharp increases in tidal variance which occur on timescales of about a week (Fig. 3.5d). The most energetic tidal event occurs in late July, coincident with strong sub-inertial eastward flow. In the subsurface, tidal KE variance is comparatively stationary (Fig. 3.5f). A strong spring-neap cycle is apparent in the semi-diurnal band, and there is weak intermittency in the diurnal band. This spring-neap cycle reflects the barotropic tide (i.e. depth-average, not shown). It is likely internal waves contribute more to the irregularity in surface tidal KE. In another FLEAT study, Voet et al. (2020) observe the formation of lee waves from a combination of sub-inertial and tidal flows over the ridge north of Velasco. However their observations suggest it is unlikely these waves contribute appreciably to upper ocean velocity. In an earlier study of

Palau, Wolanski et al. (2004) observed isotherm shoaling at tidal periods. These internal tides were synchronous the local spring-neap cycle, suggesting they were locally generated. In our observations, strong peaks in tidal surface KE are not synchronous with the local spring tide (seen in Fig. 3.5f). Changes in the local stratification could cause detuning between the barotropic tide and locally generated internal tides, but remotely generated internal tides may better explain the observed variance. To the west of Palau, the Luzon Strait is a known generation site of strong internal tide beams which may encounter Palau during favorable current conditions (Zhao et al., 2013). Propagation speeds of mode-1 internal waves in the tropical western North Pacific are $\sim$ 3 ms^{-1} (Rainville and Pinkel, 2005), which corresponds to a lag between the Luzon Strait and Palau on the order of 1 week. The arrival of such remote internal tides would not likely have a regular pattern that corresponds with the local spring-neap cycle.

There are similar irregular peaks in the inertial band at the surface, most notably twice in November and once in early March. This intermittency is consistent with wind forced inertial oscillations, which are sporadic by nature. In another FLEAT study, Siegelman et. al. (2019) characterize the inertial currents around Palau using moorings from both the northern and southern ends of the island. Although only one inertial event is easily explained using local wind data, they argue that the large decorrelation length scales of the other inertial events suggest they are wind generated. At depth, near-inertial internal waves likely contribute to the variance as well. In early November there is a weak peak around $\sim$ 2 days, as well as a smattering of energy in the super-inertial, sub-tidal band in September and October. Andres et al. (2020) observed a similar signal in acoustic travel time records from pressure-sensor equipped inverted echo sounders (PIES) around the island. This signal propagated through their array in the south-east direction, and they concluded near-inertial internal waves likely propagate into the region from higher latitudes.

3.3.2 Submesoscale Vorticity Timeseries

Here we present timeseries of submesoscale ($\sim$ 7 km) vorticity obtained via plane fit to the EOF filtered velocity timeseries from the triangular array (see section 3.2 for methodology). Because the reconstructed timeseries retain over 94% (89%) of the total velocity variance in the surface (subsurface) layer, we present the timeseries first and then the EOFs to help interpret the signals in them. Here and throughout the manuscript we often refer to 'shear', by which we mean lateral shear. When discussing vertically sheared currents, we use 'vertical shear'.

Vorticity in the surface layer has a clear relationship to the sub-inertial flow. Magnitudes are $O(1)$, reaching up to Ro $\sim$ 6 during westward flow events (Figures 3.6d and 3.7d). This is consistent with synoptic observations in the same region obtained by Wijesekera et al. (2020) during the period of strong westward flow in early December. Over the course of a week they conducted repeat ship surveys in box patterns $O(10)$ km around the northern end of Velasco. These surveys captured the flow accelerating and separating near F4, with strong recirculation immediately to the west. The recirculation was $\sim$ 5-10 km in scale and had vorticity $O(1)$ (see their Figures 3.10 and 3.11). This suggests that vorticity here also reflects flow separation and recirculation at the scale of the array. We will show this interpretation is supported by the EOFs (section 3.3.3). Sub-inertial vorticity is highly correlated with sub-inertial velocity, especially meridional velocity at F3 (R = 0.9). During the periods of energetic westward flow, vorticity increases from zero to Ro $\sim$ 5. An ~ 0.1 ms^{-1} increase in velocity corresponds to an increase in vorticity of Ro $\sim$ 1. It is noteworthy that the flow event with greatest total kinetic energy does not have a strong vorticity signature (eastward flow in late July). The reason for this is evident in the relative lack of array-scale shear, which distinguishes it from the other events.

Surface vorticity is highly broadband, and a novel observation of this study is that high-frequency vorticity variance increases substantially during strong westward flow. This can be seen by comparing the range of high-frequency vorticity prior-to and during the westward event in December (Fig. 3.6d). Initially, values range from $|\text{Ro}| \lesssim 1$. At maximum flow, this increases

to $|\mathrm{Ro}| \lesssim 4$. We define a low-frequency envelope for this variance by 10-day low-passing the magnitude of super-inertial vorticity (not shown). This envelope is strongly correlated with sub-inertial velocity, especially meridional velocity at F3 and F4 (R = 0.8). The relationship between high-frequency vorticity and corresponding low-frequency envelopes of high-frequency velocity is weaker, with $R \leq 0.5$ at all moorings other than F3, where R = 0.6.

Similar relationships between the sub-inertial current and vorticity exist in the subsurface layer as well (Figure 3.7). Sub-inertial vorticity is strongest during the westward flow event in September and October, and high-frequency vorticity variance is non-stationary. Recall that close to the topography, currents become rectilinear and the meridional component dominates during westward flow (Fig. 3.4). For most of the timeseries, sub-inertial vorticity is negligible and high-frequency vorticity is $|\mathrm{Ro}| \lesssim 1$. During the westward flow event this increases to $|\mathrm{Ro}| \lesssim 4$. The correlation between high-frequency vorticity and sub-inertial velocity is weaker than at the surface. The strongest correlation is with meridional velocity at F4 (R = 0.7), but otherwise less than 0.5. It is clear that the strength of the current is not the distinguishing factor leading to elevated vorticity. Instead, strong shear in the meridional component across the array separates this period from the rest. As with the surface layer, the period with greatest kinetic energy (here January) does not have a vorticity signature due to a lack of array-scale shear.

3.3.3 Dominant Statistical Modes

The EOFs of velocity used to filter out unresolved spatial variability give the horizontal structure of currents around Velasco and their contributions to the vorticity (Figure 3.8). At the surface, the most energetic EOF accounts for 72% of the total velocity variance and reflects large-scale flow around the island (Fig. 3.8a). Current vectors are in phase with similar magnitude. Velocities are strongest at F4 where the flow is forced to accelerate around the promontory, and weakest in the lee at F2 where it must decelerate. Because its vorticity is the result of shear rather than a coherent vortex, the OW value of the first EOF is weakly positive (Fig. 3.8b). The second

most energetic EOF contains 17% of the total velocity variance and is similar in character to the first EOF. Together these EOFs describe large-scale currents forced to circumvent the island from either direction, producing shear at the array scale. This shear contains 36% and 13% of the total vorticity variance, respectively. The third most energetic EOF contains just 5% of the total velocity variance, but nearly half (45%) of the total vorticity variance. Current vectors rotate counterclockwise around the center of the triangle with similar magnitudes, and the OW value is strongly negative. This suggests the third EOF describes vortex motion at the scale of the array, which likely reflects a combination of attached recirculating flow and fully separated eddies.

The EOFs of subsurface velocity have a similar variance distribution and similar structures (Figure 3.8e-h). The two most energetic EOFs account for 64% and 18% of the total velocity variance and describe large-scale flow around the island. The third EOF accounts for only 7% of the velocity variance and describes eddying motions at the scale of the triangle. This EOF is responsible for a bulk of the vorticity variance. While the first two EOFs account for only 5% and 4% of the total vorticity variance, the third EOF accounts for 75% of the total vorticity variance. An important difference between the surface and subsurface EOFs is that vectors of the first subsurface EOF follow the topography. Additionally, the second EOF describes flow from the east but has a westward component at F4 and therefore significant convergence. These two dissimilarities suggest that the large-scale subsurface flow often does not separate, reflected in the negligible vorticity of the first two EOFs.

Both in the surface and subsurface layers, the three least energetic EOFs are dominated by strain and divergence. We interpret these EOFs as currents which are not properly resolved by the triangle and they were not included in the reconstruction of velocity as a means of scale filtering.

3.3.4 Non-stationary Vorticity Variance

The EOFs enable us to decompose vorticity into contributions from 1) currents in phase across the array and 2) eddy motion at the scale of the array (Figure 3.9). Our goal in this section

is to gain physical insight into the processes leading to vorticity generation around Palau, i.e. to understand which motions are responsible for the observed non-stationary vorticity variance. For both layers, we define a 'shear' component of vorticity as due to the first two EOFs (in phase) and an 'eddy' component of vorticity as due to the third EOF (eddy motion). However, it is important to keep in mind that these are statistical modes, not true physical modes, and the real currents are a linear superposition of them (plus a mean).

In the surface layer, shear and eddy components contribute 49% and 45% to the total vorticity variance, respectively. This equitable distribution is reflected in their individual timeseries (Figure 3.9a and 3.9b). Both components range up to $|\mathrm{Ro}| \lesssim 4$. However, their frequency content differs substantially. Shear vorticity contains greater relative sub-inertial variance, while eddy vorticity has greater relative super-inertial variance. This is evident from the timeseries but is quantified in their corresponding power spectral densities (Figure 3.9e). The spectrum of shear vorticity closely resembles kinetic energy, with strong inertial and tidal peaks (gray line in Fig 3.9e). Eddy vorticity has similarly strong tidal peaks, but they are less prominent due to the broadband elevation in high-frequency variance. It is clear from the surface timeseries that non-stationary high-frequency variance is primarily due to the eddy component of vorticity (Fig.3.9a). The range of values increases abruptly from $|\mathrm{Ro}| \lesssim 1$ up to $\lesssim 4$ at the end of November, concurrent with the onset of strong westward flow. There is a corresponding low-frequency increase in the shear component of vorticity. High-frequency variance in the shear component is comparatively steady.

In the subsurface layer, the shear component contributes only 9% to the total vorticity variance while the eddy component contributes 75%. As a result, the eddy vorticity timeseries closely resembles the full vorticity timeseries (Fig.3.7d). The eddy component ranges up to $|\mathrm{Ro}| \lesssim 1$ for most of the record but increases up to $|\mathrm{Ro}| \lesssim 4$ in September and October during westward flow. Shear component vorticity is characterized by a weak spring-neap cycle and strong peaks in the tidal bands, with close adherence to the spectrum of KE. As in the surface

layer, eddy vorticity has greater relative variance at super-inertial frequencies and as a result its tidal peaks are less prominent.

As with KE, we examine the spectral distribution of total vorticity as a function of time using scalograms (Figure 3.10 and 3.11). We do not show scalograms of each component because our goal is to quantify the temporal variability of the true vorticity around Palau. However, we note that the scalogram of shear vorticity nearly mirrors KE. Differences between the scalograms of total vorticity and KE reflect non-stationary variance in the eddy component (as noted above). At the surface, the scalogram reveals that elevated variance during westward flow is the result of strong peaks in both tidal bands, especially the diurnal band in December and March (Fig.3.10c). Energy increases at super-tidal frequencies as well. Peaks in near-inertial variance appear to loosely coincide with the waxing and waning of the sub-inertial current. At depth, there are clear peaks in the tidal and inertial bands, but the increase in high-frequency variance is more broadband than at the surface. This is predominantly due to elevated variance in the super-inertial, sub-tidal band, especially a strong peak at a period of ~ 2 days in early November. As mentioned in section 3.3.1, this may be related to super-inertial waves observed by Andres et al. (2020).

These vorticity scalograms differ substantially from corresponding KE scalograms (described in section 3.3.1, see Fig. 3.5). Surface tidal KE is irregular, and its low-frequency modulation only loosely coincides with westward flow. For example, KE in both bands increases in mid-October, over a month before the onset of westward flow in late November. In contrast, tidal vorticity variance only increases during strong westward flow. Also, peaks in tidal band KE mostly do not coincide with peaks in tidal band vorticity. At depth these differences are starker. Super-inertial KE is dominated by a steady spring-neap cycle in the semi-diurnal band, but vorticity is entirely event driven. These differences reflect the asymmetric distribution of velocity and vorticity variance between the shear and eddy components. The statistical modes which are responsible for most of the KE variance contain vorticity in the form of lateral shear. Therefore, the relationship between shear vorticity and KE is approximately linear across all

frequencies. However, most of the vorticity is due to eddy motions, which increase non-linearly in the tidal bands during strong westward flow events.

3.4 Discussion

In this study we have used velocity data from moored ADCPs to characterize the broadband current as well as submesoscale vorticity ($\sim$7 km scale) around the northern end of Palau . We have examined properties of the flow in both the shallow surface layer (0–100 m) and a subsurface layer (300–400 m). We find that flow in the surface layer is broadband, comprised of large-scale sub-inertial currents and strong tidal and inertial currents (Fig. 3.3 and 3.5). Sub-inertial currents are topographically blocked and downstream currents are weak. Oscillatory flows are highly intermittent, likely in part due to internal tides as well as wind-forced near inertial currents. At depth, sub-inertial currents are weaker and a single north-westward flow event dominates the variance (Fig. 3.4 and 3.5). For most of the record however, high-frequency currents are stronger than the sub-inertial flow. Tidal kinetic energy is steady, dominated by a clear spring-neap cycle in the semi-diurnal band.

A novel observation of this study is that vorticity variance increases by up to an order of magnitude in the tidal bands during periods of strong westward flow (Fig. 3.10 and Fig. 3.11). Intermittency in tidal band KE does not easily explain this variance, pointing to non-linearity in the wake generation process. Empirical orthogonal functions (EOFs) of velocity reveal that although 80-90% of the velocity variance is due to large-scale currents in phase as they flow past the island, 45-75% of the vorticity variance is contained in eddying motions which contribute only minimally to the total velocity variance ($\sim$ 4-7%). Spectra of vorticity due to these eddy motions are characterized by strong peaks in the tidal bands, and scalograms show this variance increases during strong westward flow (Fig. 3.10c and 3.11c). These observations suggest that eddies are formed (and possibly shed) at tidal frequencies, but that the strength of their vorticity

varies with the sub-inertial current.

In this section we discuss the physical mechanism likely responsible for this non-linearity. We argue that the broadband content of the flow modulates the strength of vorticity as well as the rate at which eddies are formed. In light of significant intermittency of tidal KE at the surface, we also consider the potential contribution of internal waves to the observed vorticity. Finally, we speculate on the relationship between submesoscale eddies and the island scale wake.

3.4.1 Non-linear Broadband Eddy Formation

The observations detailed above are consistent with wake eddies generated by a combination of oscillatory and steady flows past a headland. The source of vorticity in the recirculating wake is shear across the upstream boundary layer, which is a function of total incident flow strength. We see this dependence reflected in the EOFs with shear in the cross-shore direction (Fig. 3.8). These EOFs contain most of the KE variance and thus shear vorticity is strongly correlated with the total velocity (R = 0.7 in both layers, Fig. 3.9a and 3.9c). This attached recirculating flow forms eddies if the flow reverses and generates an opposing shear layer inshore of the wake which disrupts the upstream supply of vorticity (Signell and Geyer, 1991; Pawlak et al., 2003). In our observations, tidal currents are often strong enough to either arrest or reverse the low-frequency flow (Fig. 3.3 and 3.4). Thus oscillatory currents force the formation of eddies, while low-frequency currents modulate their vorticity. An example snapshot of surface velocity vectors at both flood and ebb tide during strong westward flow encapsulates this process (Figure 3.12). The velocity is decomposed into the shear and eddy components as discussed in section 3.3.4. At flood tide, shear is generated by the superposition of strong sub-inertial and tidal currents. Later at ebb tide, the zonal component of velocity close to the reef at F2 has reversed, introducing oppositely signed shear and generating an eddy near the scale of the array. We note that elevated tidal vorticity variance occurs in this study when the free-stream flow does not fully reverse, but is substantially weakened by the opposing tide (Fig. 3.6). Weakened or slack currents

may be sufficient to allow an inshore shear layer to grow due to friction between the attached recirculation and the headland (Davies et al., 1990).

Two recent synoptic observational studies off the coast of Taiwan provide further support for this interpretation. Using a combination of drifter and satellite data Cheng et al. (2020) captured the evolution of three successive submesoscale eddies generated by strong northward flow past the southern cape of Taiwan. These eddies appeared to be generated at a diurnal frequency with similar scales and vorticity to those observed in this study. Using a realistic model of the region, the authors show that eddies are indeed likely shed at tidal frequencies with vorticity modulated by the tide and sub-inertial current strength (see their Fig. 3.6). At smaller scales, synoptic surveys by Chang et al. (2019) captured the generation of eddies by the flow of the Kuroshio past Green Island, a 7-km island north-east of the cape. These synoptic observations suggest eddies shed close to a diurnal period, and they observed strong tidal peaks in measurements of velocity from two downstream moorings. However they estimate that the natural shedding frequency of the island (i.e. the Strouhal period) was also close to a tidal period, and so there was a high degree of uncertainty in their estimate of the wake period.

In our case, the observations are inconsistent with eddy shedding at a natural frequency. Although difficult to predict due to its dependence on the Reynolds number, we can estimate an upper limit for this frequency. Maximum values of St are 0.45 for $\mathrm{Re} > 10^5$ (Bearman, 1969). Mean length scales in the wake on these longer timescales reflect the width of Velasco, so L $\sim$70 km (Zeiden et al., 2019). Peak velocities observed during westward flow are 0.5 ms^{-1} (Fig. 3.3). This gives a maximum shedding period of 86 hours, many times either the diurnal or semi-diurnal tidal period. We also consider the possibility that eddy-eddy interactions could modulate the near-field vorticity, as in Callendar et al. (2011). However this modulation would likely reflect a spring-neap cycle (see their Fig. 3.6). In our observations tidal vorticity is not modulated by a spring-neap cycle, even at depth where the spring-neap forcing is strong.

3.4.2 Internal Waves and Vorticity Variance

In the simple case of regular tides (i.e. barotropic) plus sub-inertial currents, the latter is responsible for modulating the eddy strength. At depth this explains most of the vorticity and velocity variance. Subsurface semi-diurnal tidal currents dominate tidal KE variance with a clear spring-neap cycle (Fig. 3.5f). Tidal band vorticity is weak and steady, except during a period of sub-inertial westward flow which generates array scale shear (Fig. 3.7). This simple relationship is reflected in the scalogram of subsurface vorticity (Fig. 3.10e). At the surface however, there is significant intermittency in tidal band KE (Fig. 3.5d). This is likely due to internal waves which are not steady in time. Here we consider how internal waves may contribute to non-stationary tidal vorticity variance, whether directly via aliasing or indirectly via modulation.

First, we consider remotely generated internal tides which may propagate into the region. The horizontal length-scales of freely propagating mode-1 internal tides in the tropical North Pacific are $O(100$ km) (Zhao et al., 2013). At these scales remote internal tides would likely appear at the array as currents in phase with almost uniform magnitude. Our EOF analysis has shown that tidal band vorticity is mostly due to rotational eddy motion across the scale of this triangle. Therefore, remote internal tides with these characteristics do not likely contribute directly to eddy vorticity. However, they may modulate the strength of boundary layer shear in a manner analogous to the sub-inertial current. There are a few instances which match this description for internal tides. For example, in late December/early January KE variance increases sharply in the diurnal band (Fig. 3.5d). Tidal velocities increase simultaneously at far-field moorings F1 and M5, suggesting large length scales (Fig. 3.3). This is one of the few times when tidal band vorticity variance increases in both the shear and eddy component (not shown). The diurnal KE event in mid-March has similar characteristics, and notably both events occurred during strong westward flow. Two additional tidal KE events fit the description of an internal tide (abrupt increases in KE variance, large length scales), but neither have strong vorticity signatures. The first occurred in July during strong eastward flow, and the second in November when the sub-inertial current was

weak. This may suggest the combination of tidal and westward flow is essential to generating eddies, or this may reflect the location of the array just west of the separation point (Fig. 3.1c).

Locally generated, high-mode internal waves with small horizontal scales have the potential to alias directly into the observed eddy vorticity. These waves might be perceived to contain vorticity, but only if they have a wavelength close to the scale of the array. Another FLEAT study observed the generation of internal waves over the ridge extending north of Velasco, at the same latitude as F3 (Voet et al., 2020). These waves were dependent on the combined strength of the sub-inertial current and the semi-diurnal tide, which is the dominant component of the local barotropic tide (Fig. 3.5f). However, the observations of Voet et. al. (2020) suggest it is unlikely the waves propagate through the strong vertical shear at the base of the surface layer. Further, high-mode internal waves do not typically contain much energy (Pinkel, 1984). Finally, as previously noted, the observed variance in tidal band KE is weakly modulated on sub-inertial timescales but does not align closely with the local flow. Thus, it seems unlikely that local internal waves contribute significantly to the observed eddy vorticity.

3.4.3 Implications for the Palau Wake

Here we speculate on implications for the Palau wake. Submesoscale eddies observed in this and other FLEAT studies are O(10 km). This is consistent with advective length scales estimated from typical velocities over a tidal period during strong westward flow (Fig 3.5c). Given U $\sim$ 0.25 ms^{-1}, eddy length scales are $L \sim$10 and 20 km for the semi-diurnal and diurnal tidal period, respectively. If vorticity is similarly approximated as $\zeta \sim U/L$, these eddies have Ro $\sim O(1)$. This is consistent with vorticity observed in this and the synoptic study by Wijesekera et al. (2020). In the case of steady flow, wake eddies are proportional to the island scale (Heywood et al., 1990; Dong et al., 2007). Were eddies to develop on sub-inertial timescales to this scale (O(100 km)) they would have Ro $\sim O(10^{-1})$. Thus, when tidal currents control the formation rate they likely reduce the scale and increase the vorticity of wake eddies by an order of magnitude.

FLEAT observations suggest both an island scale wake and submesoscale eddies are generated around Palau. Mean currents downstream of Velasco show island scale recirculation with Ro $\sim O(10^{-1})$ at the surface (Zeiden et al., 2019). This wake pattern is often visible on timescales as short as a few days, but there is significant variance. Wake vorticity occasionally reaches Ro $\sim O(1)$ with 10 km scales and smaller, possibly the result of smoothing over many smaller eddies.

Submesoscale eddies likely relate dynamically to the island scale wake in one of two ways. First, they may act as agents of momentum transfer. This is the process which motivates the use of an 'eddy' viscosity in lieu of molecular viscosity when comparing island wakes to idealized wakes (e.g. Teague et al., 2005). For example, Delandmeter et al. (2017) observed the development of fine-scale eddies in the wakes of shallow islands in the Great Barrier reef. They argued these eddies control momentum transfer between the outer flow and the wake by enhancing the viscosity of the shear layer. Second, submesoscale eddies may behave like two-dimensional turbulence and merge, undergoing an inverse cascade to larger scales. A numerical study by Molemaker et al. (2015) depicts submesoscale anticyclones in the California undercurrent coalescing until stabilizing near the local Rossby radius of deformation. In another study by Callendar et al. (2011), eddies generated by tidal flows coalesce on spring-neap timescales to larger scales. In these scenarios, submesoscale eddies are a direct source of island-scale wake vorticity. To what degree either (or both) of these processes influences the development of an island scale wake behind Palau is an open question.

3.5 Conclusion

In this study we have used 11-months of velocity observations from moorings deployed around a steep-sided mesoscale island, Palau, to quantify submesoscale vorticity generated by broadband currents circumventing the topography. In the energetic surface layer there is commensurate energy in tidal, inertial and low-frequency flows. Vorticity as measured by the

Rossby number is $O(1)$ and similarly broadband, but its relationship to the flow is non-linear. During strong westward flow vorticity increases by almost an order of magnitude in both the sub-inertial and tidal bands. Empirical orthogonal functions (EOFs) of velocity reveal that this increase in tidal vorticity during strong low-frequency flows is due to eddying motions at the array scale ($\sim$ 7 km). In contrast, lateral shear across the array is linearly related to velocity. We argue this reflects the linear superposition of currents which generates shear in the boundary layer. This shear is the source of eddy vorticity in the wake, but high-frequency oscillatory currents control the rate of eddy formation. Thus, eddies likely increase in strength during strong sub-inertial flow, but are formed at a tidal frequency and so contribute to vorticity variance in the tidal band. This is unlike the case of steady flow, in which eddies are formed at a frequency dependent on the island scale and current strength alone.

The results of this study contribute to a growing body of research aimed at understanding how the broadband content of real geophysical flows influences the development of wakes. We have shown that energetic oscillatory currents modulate the formation of submesoscale eddies, but it is unclear how this impacts the island scale wake. We have discussed momentum transfer and an inverse cascade as two possible mechanisms by which submesoscale eddies may modulate or contribute directly to large scale vorticity. These processes require eddies to be stable downstream of the separation point. However, eddies with $|\mathrm{Ro}| >> 1$ and strong baroclinicity may decay in the near field. Anticyclonic eddies with $|\mathrm{Ro}| > 1$ are susceptible to centrifugal instability and may diffuse significantly within a few turnover timescales (Dong et al., 2007). Tilted eddies generated around headlands with sufficient vertical shear may overturn and generate strong vertical mixing (Pawlak et al., 2003; Farmer et al., 2002). The submesoscale eddies around Palau are preferentially cyclonic due to the mean westward flow, but anticyclonic eddies can be generated if oscillatory flow reversals are strong enough (Fig. 3.9). Although steep compared to typical topography, the 45° slope around Velasco has the potential to generate tilted eddies. Strong vertical shear in the upper few hundred meters likely enhances any baroclinicity (Fig. 3.2). Finally, fine-scale eddies

may influence the life cycle of submesoscale eddies. In another FLEAT study, MacKinnon et. al. (2019) observed the generation of 1-km wide eddies on tidal timescales immediately in the lee of the northernmost promontory of Velasco (Fig 3.1c). A full understanding of the Palau wake will hinge on understanding how eddies across this wide range of scales interact.

3.6 Acknowledgments

This work was funded by Office of Naval Research under Grants N00014-16-WX01186, N00014-15-1-2488, N00014-15-1-2592, N00014-15-1-2264, N00014-15-1-2302, and N00014-16-1-3070, and N00014-18-1-2406. We would like to thank Captain Murline and his crew on the R/V *Roger Revelle* for their assistance and support in the successful deployment and retrieval of moorings. We also thank the engineers of the Multiscale Ocean Dynamics group at the Scripps Institution of Oceanography who were instrumental in the preparation and deployment of the moorings. We are very grateful to Pat and Lori Colin from the Coral Reef Research Foundation in Palau for their community engagement and onshore logistical support.

Chapter 3, in full, is a reprint of the material as it appears in Zeiden, K.L., J.A. MacKinnon, D.L. Rudnick, M.H. Alford, H. Wijesekera and G. Voet (2021). Broadband Submesoscale Vorticity Generated by Flow Around an Island. doi:10.1175/JPO-D-20-0161.1. Used with permission from ©American Meteorological Society. The dissertation author was the primary investigator and author of this paper.

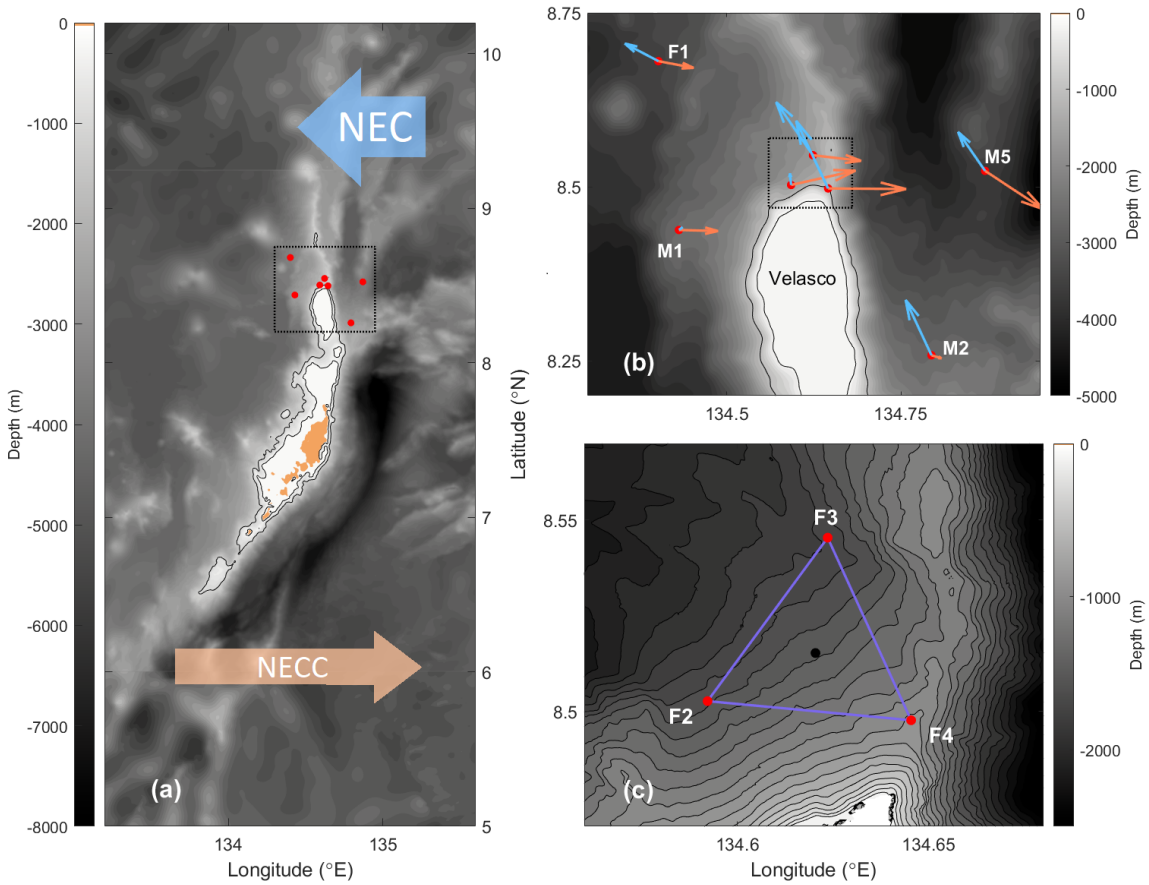

Figure 3.1: Mooring locations plotted over regional (a) and local (b),(c) bathymetry. Insets (b),(c) are marked in (a),(b) respectively with dashed black lines. Filled tan contour in (a) is land above sea-level. Black contours in (a),(b) are 100- and 1000-m isobaths, and 100-m intervals in (c). Mooring locations are in red. Blue and orange vectors in (b) are mean surface currents during strong eastward (August, orange boxes in Fig.3.3) and westward (December, blue boxes in Fig.3.3) flow. Topographic steering is apparent during westward flow. Moorings were deployed for 11 months between May 2016 and April 2017 around the northern end of Palau, where the NEC encounters the island on average. Moorings F1, F2, F3, F4, M1, M2 and M5 are used to characterize the flow field, while moorings F2, F3 and F4 are used for a detailed vorticity analysis.

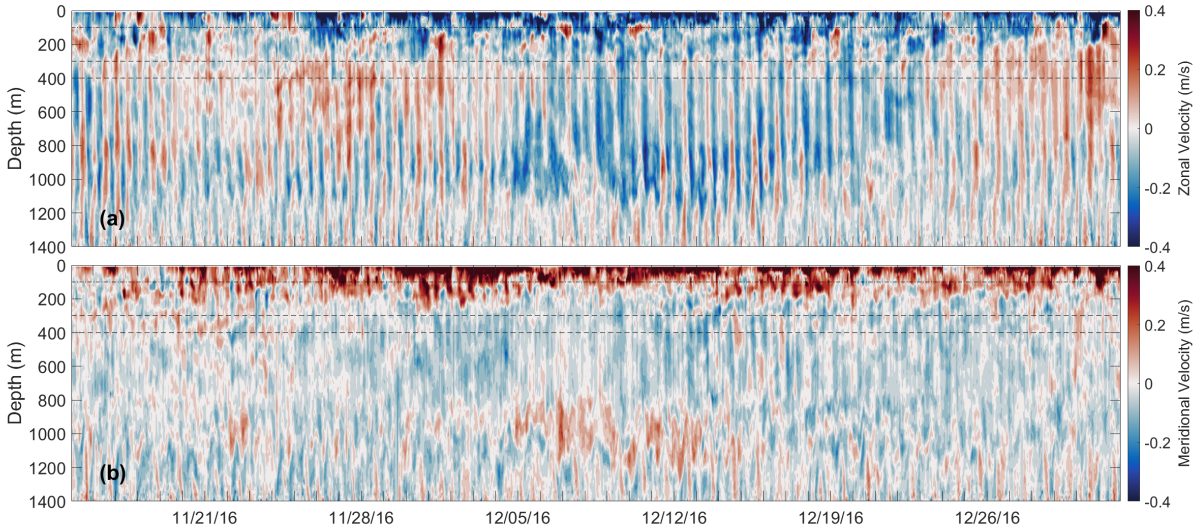

Figure 3.2: Example section of (a) zonal and (b) meridional velocity from 0-1400 m at F3 during a strong westward sub-inertial surface current event from November 15, 2016 to January 1, 2017 . Ticks are one-day intervals. Black dot-dash line in both panels indicates the base of the surface layer (0-100 m). Black dash lines indicate the subsurface layer (300-400 m). Strong tidal velocities retard the sub-inertial current and often lead to flow reversals, especially at depth where the sub-inertial current is weaker. Correlation values between velocity at different depths within each layer are strong ($R > 0.5$ and 0.8 in the surface and subsurface layers, respectively).

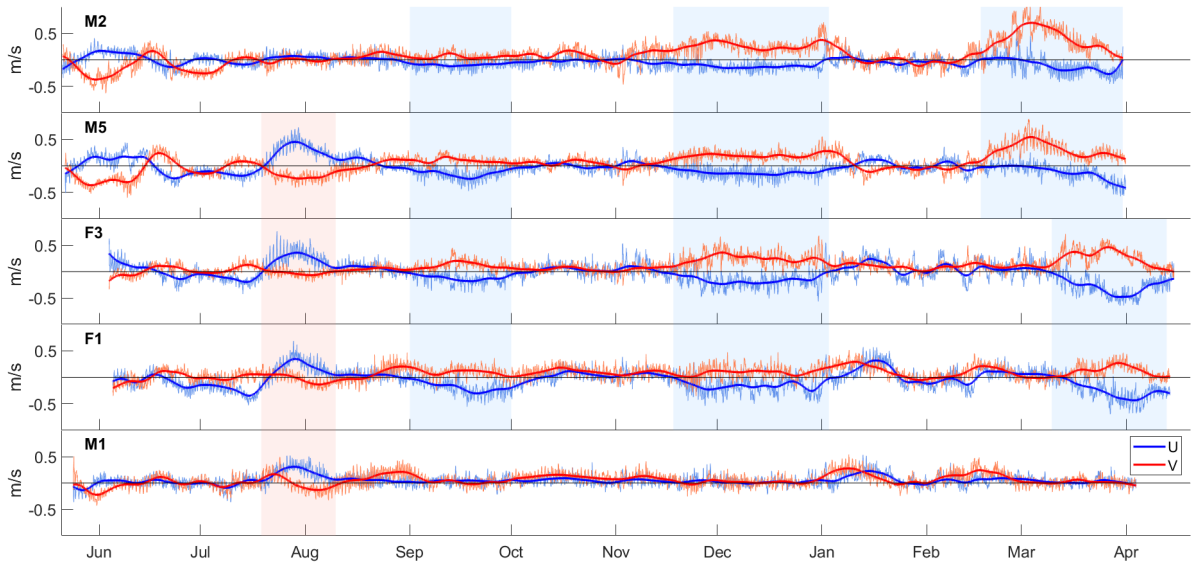

Figure 3.3: Surface (0-100 m depth-averaged) zonal (blue lines) and meridional (red lines) velocity timeseries at M2, M5, F3, F1 and M1 (counterclockwise around the reef). Thick lines are 10-day low-passed. Four major sub-inertial current events dominate the variance and show topographic blocking of large-scale flows: strong eastward flow in August (absent downstream at M2, marked with red boxes) and strong north-westward flow in September, December and March/April (absent downstream at M1, marked with blue boxes). Strong northward flow to the east of Velasco precedes the fourth westward event, appearing first at M2 and M5 before transitioning to north-westward flow. Significant high-frequency variability frequently leads to flow reversals.

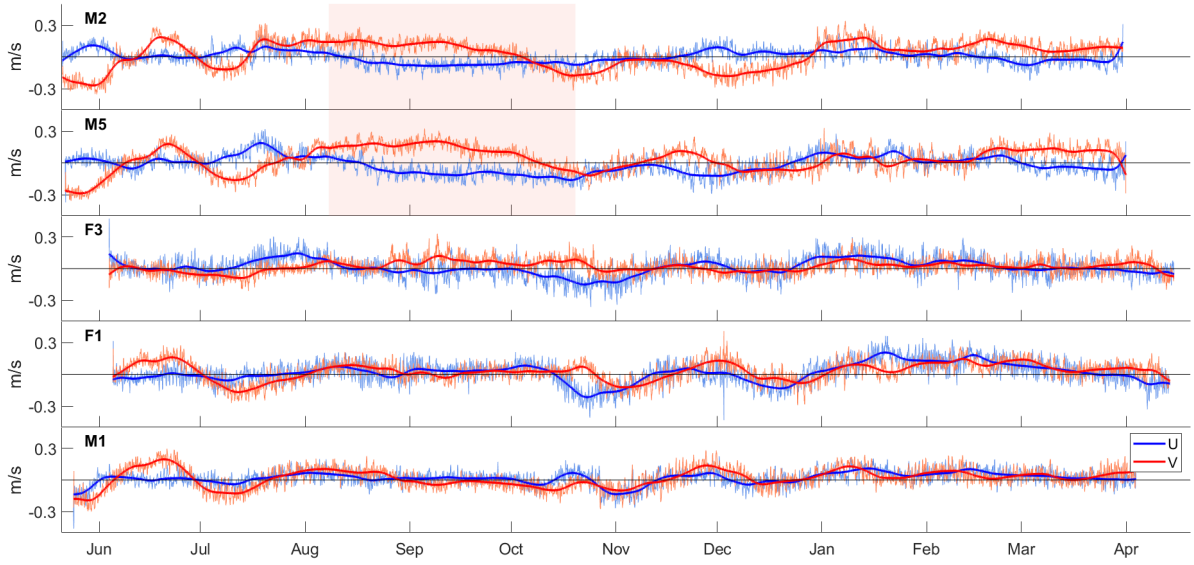

Figure 3.4: As in Fig. 3.3, but for the subsurface (300-400 m depth-averaged). One main sub-inertial north-westward current event is apparent east of Velasco at M2 and M5 in August and September (marked with red boxes), but otherwise high-frequency currents are often significantly stronger than the sub-inertial flow at depth.

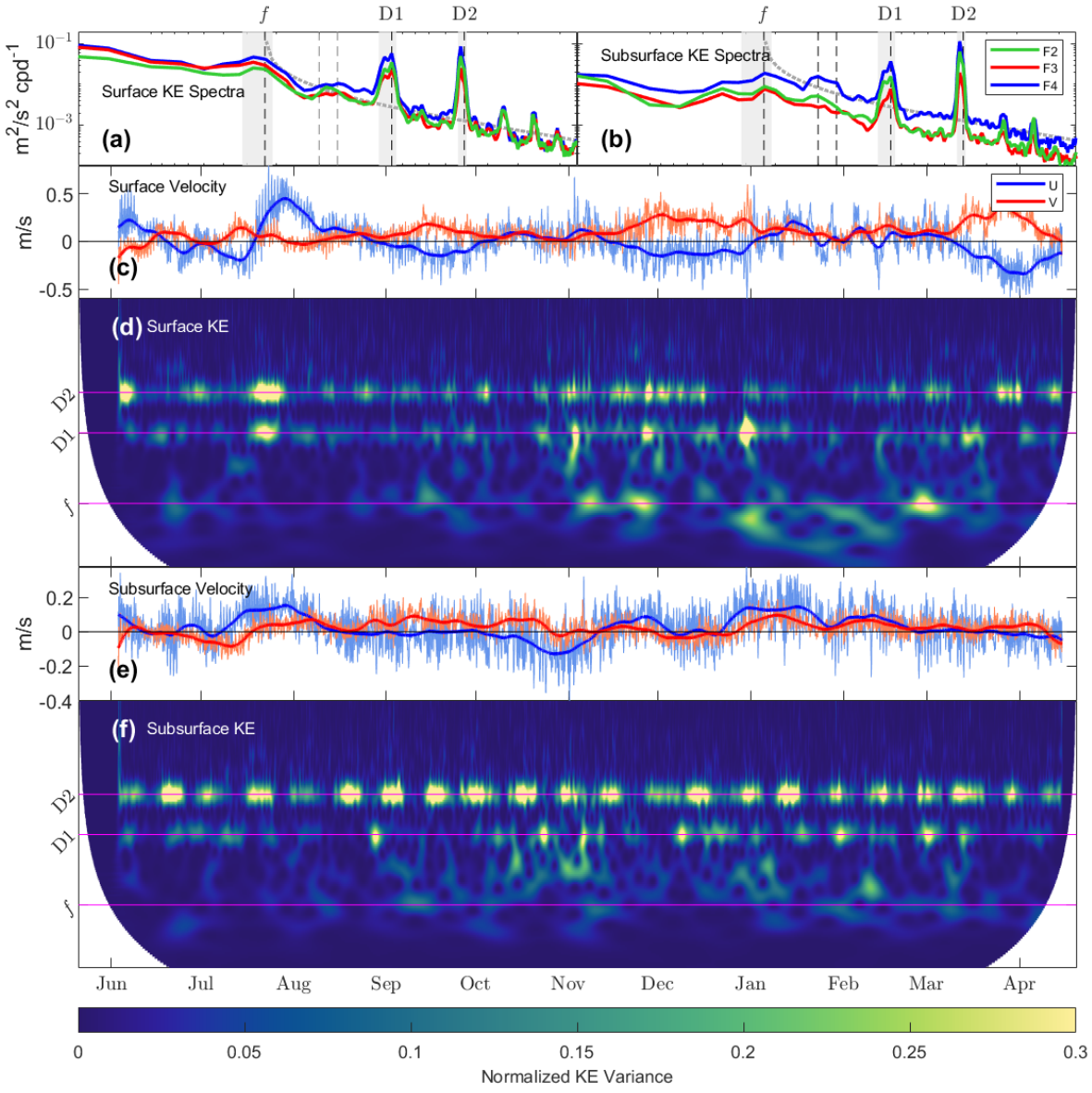

Figure 3.5: Surface (a) and subsurface (b) kinetic energy spectra at F2 (green), F3 (red) and F4 (blue) are red, with strong peaks in the inertial, diurnal and semi-diurnal bands. Dotted grey line in (a),(b) gives the Garrett-Munk internal wave spectrum for reference. Timeseries of array averaged surface velocity (c) and a corresponding scalogram of kinetic energy (d) reveal that energy in these bands is non-stationary in the energetic surface layer. Conversely, subsurface array averaged velocity (e) and corresponding kinetic energy scalogram (*f*) have steady tidal energy, modulated only by spring-neap variability.

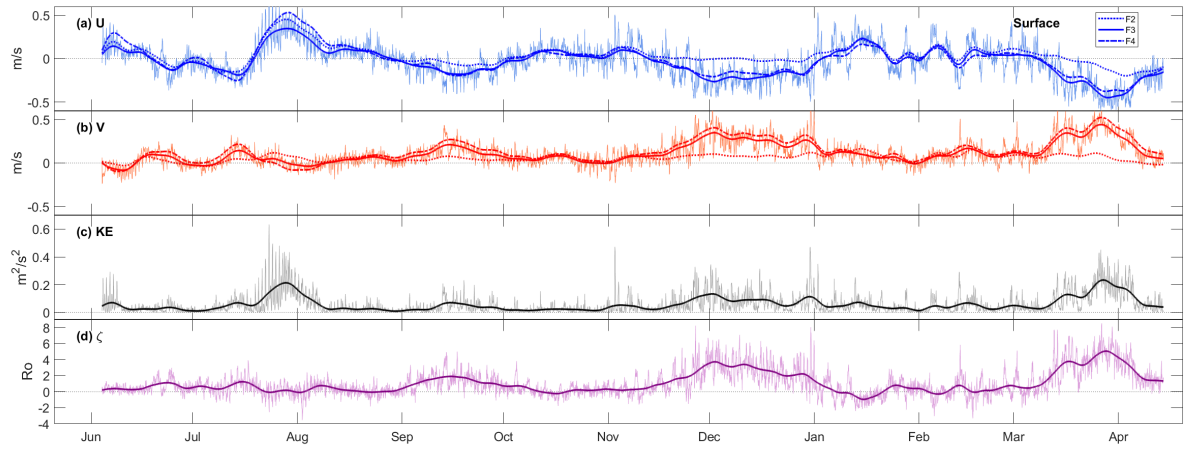

Figure 3.6: Timeseries of array-mean surface (a) zonal velocity, (b) meridional velocity, (c) kinetic energy and (d) vorticity. Velocity timeseries were reconstructed using EOFs (section 3.3.4). Bold lines are 10-day low-passes of the respective timeseries, except for (a),(b) which are 10-day low-passes at each of the three moorings in the array. Sub-inertial vorticity varies linearly with sub-inertial velocity during westward flow. A key result of this study is that high-frequency vorticity variance also increases during strong westward flow. Eastward flow does not have a strong vorticity signature.

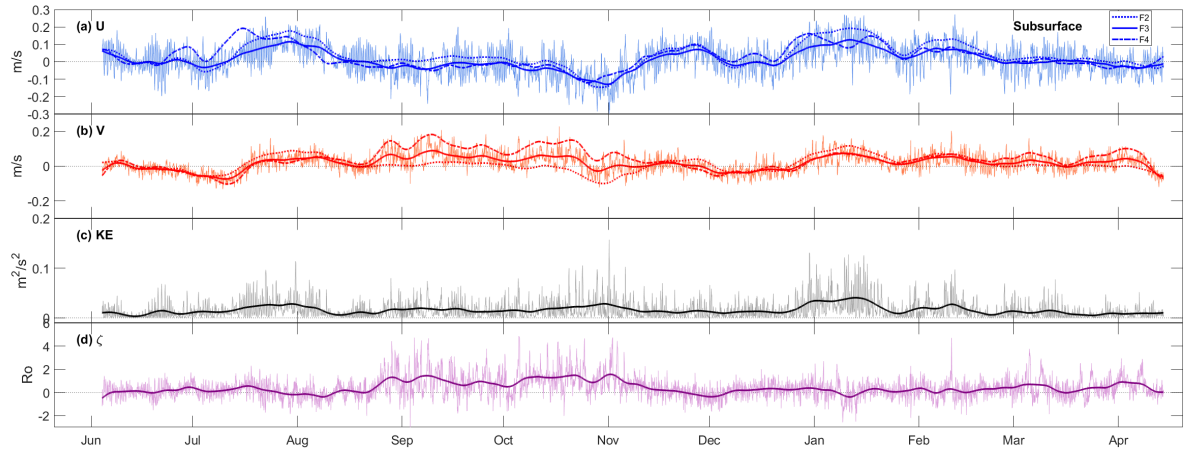

Figure 3.7: As in Fig. 3.6, but in the subsurface (300 – 400m). Note the changes in vertical axes from Fig. 3.6. Unlike surface velocities, at depth the current is often dominated by high-frequency variance. One sub-inertial even stands out with strong shear across the array evident in meridional velocity in September and October. Vorticity is steady and significantly weaker than at the surface, except during this sub-inertial event when it increases both in the sub-inertial band and at higher frequencies.

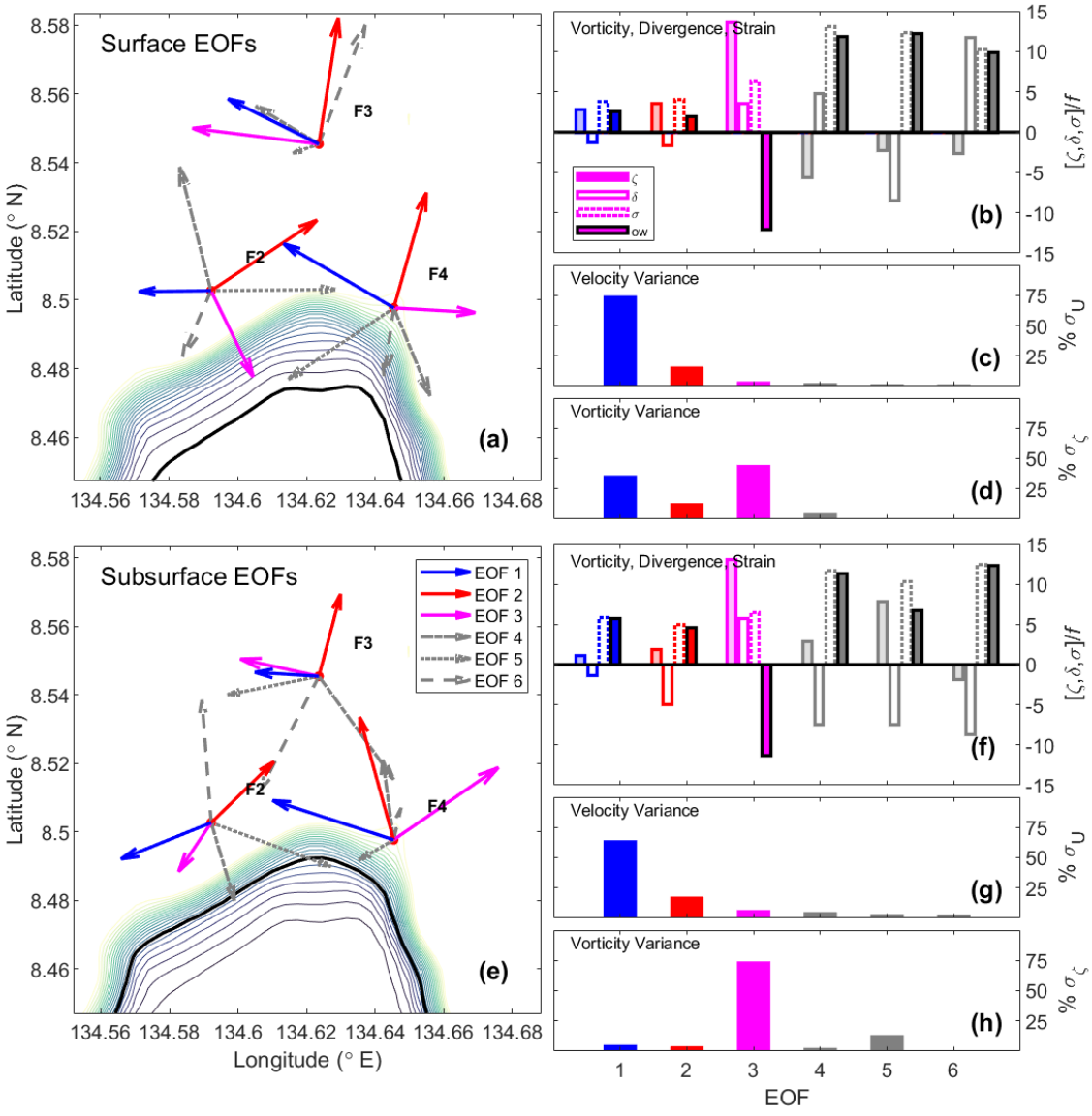

Figure 3.8: Empirical orthogonal functions of velocity in the (a) surface layer (0-100 m) and (b) subsurface layer (300-400 m). Colored contours in (a),(b) are 100 m interval isobaths from 0- to 1000-m and the black contour is the depth of the EOFs. Corresponding normalized magnitudes of vorticity, strain, divergence and OW value are plotted in (b),(e), while the percentage of the total variance described by each EOF is plotted in (c),(f). In both layers the two most energetic EOFs (red and blue lines and vectors, respectively) describe currents in phase with similar magnitude. The third EOF (magenta lines and vectors) describes vortex motion at the scale of the triangle. The three least energetic EOFs are characterized by strong relative divergence and strain. Subsequent vorticity timeseries are calculated using only the first three EOFs.

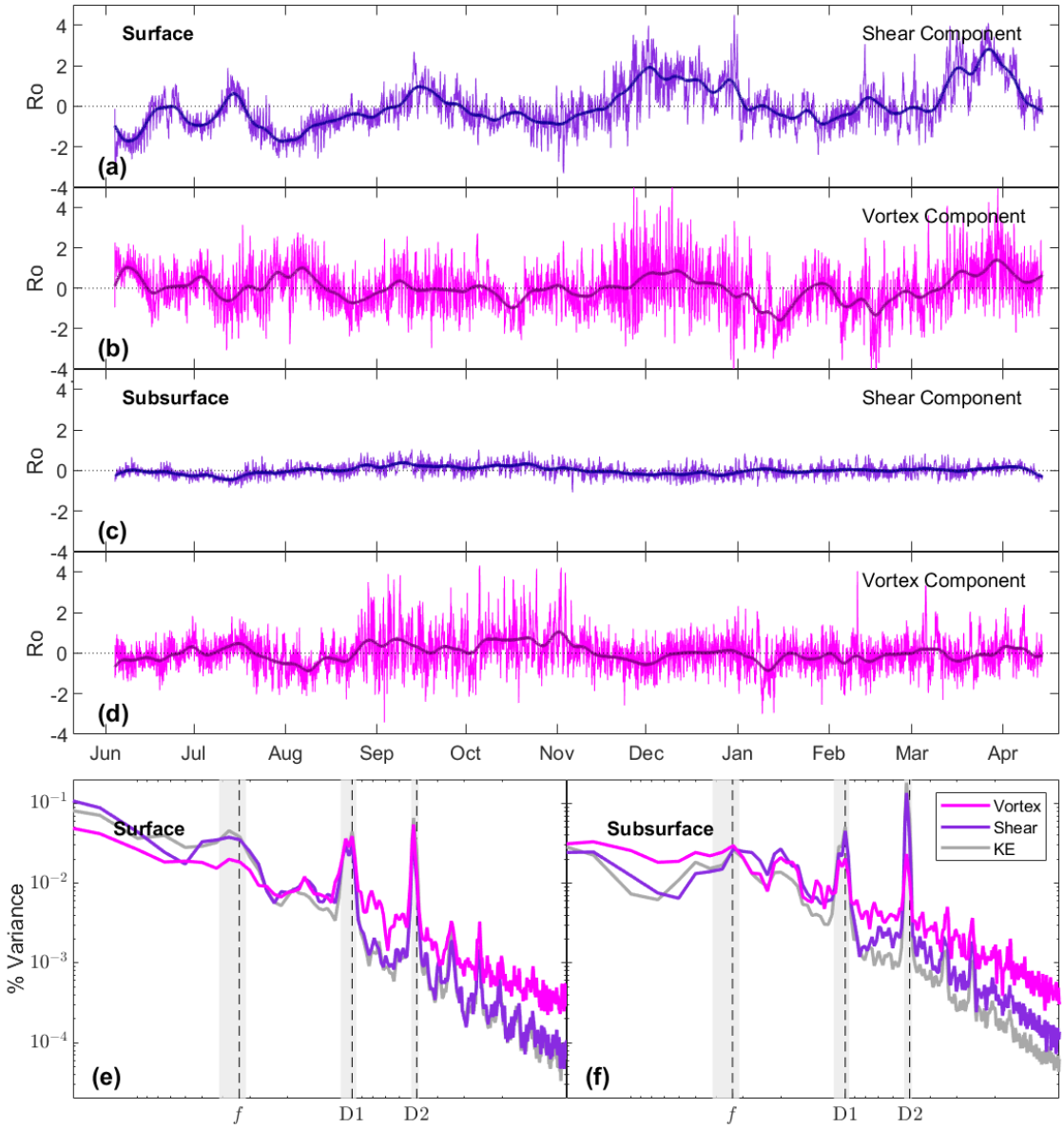

Figure 3.9: Timeseries of (a),(b) surface and (c),(d) subsurface vorticity calculated using velocity from (a),(c) EOFs characterized by lateral shear and (b),(d) EOFs characterized by eddy motion. Bold lines are 10-day low passes of each. Corresponding vorticity power spectral densities are plotted in (e) and (f), along with kinetic energy spectral densities in grey for comparison. The shear component at the surface is dominated by sub-inertial variability and steady high-frequency variability. The eddy component contains greater relative high-frequency variance which is non-stationary. In the subsurface layer, the shear component is weak, steady and dominated by tidal variance. The eddy component is responsible for a bulk of the vorticity as well as non-stationary vorticity variance.

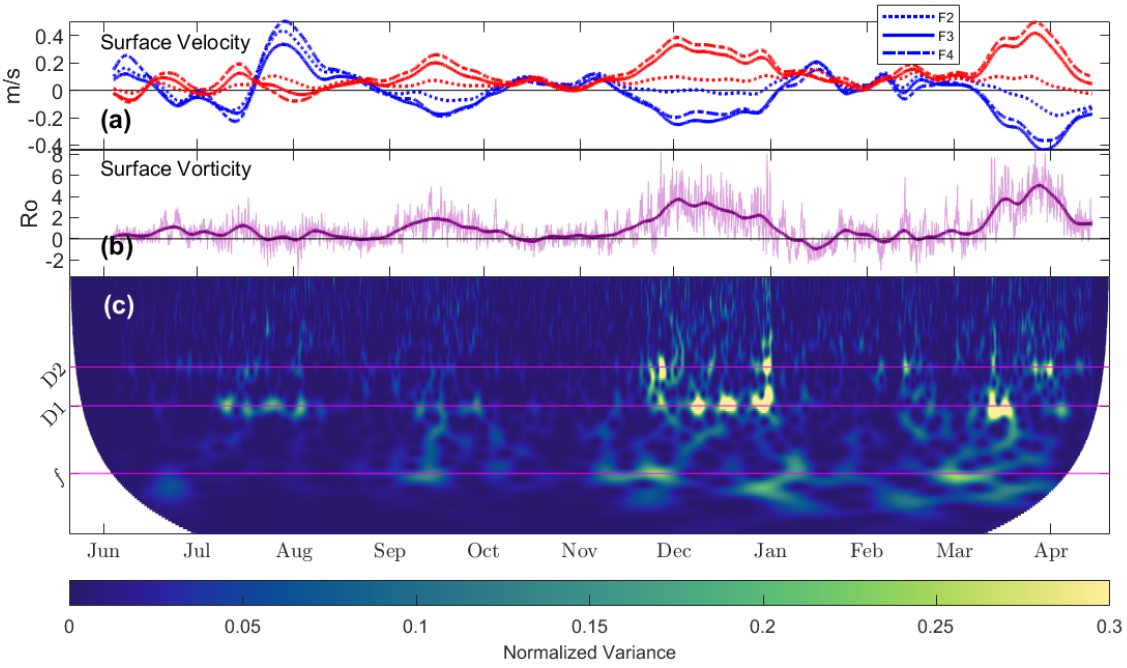

Figure 3.10: Timeseries of surface (a) sub-inertial velocity at all three moorings and (b) vorticity, along with (c) the scalogram of vorticity gives time variability of its frequency content. Bold lines are 10-day low passes of each timeseries. Scalograms are normalized by the total variance contained at frequencies higher than (10 days)$^{-1}$. High-frequency vorticity variance is highly episodic and strongly correlated with the sub-inertial flow. Increases in surface tidal variance occur during strong sub-inertial westward flow in December and March. Kinetic energy (Fig. 3.5d) in the tidal bands is comparatively stationary, and the strongest peaks do not coincide with those in vorticity.

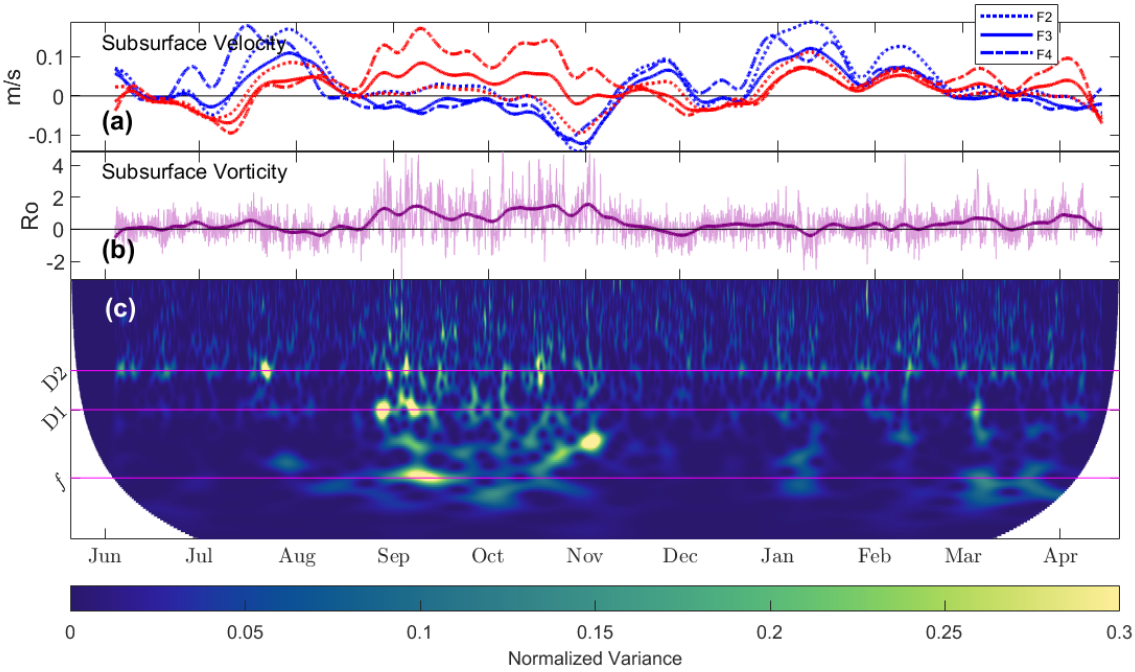

Figure 3.11: As in Fig. 3.10, but for the subsurface layer. High-frequency vorticity variance increases dramatically in September and October during a sub-inertial current event characterized by strong shear. This is dissimilar to kinetic energy at depth, which has a strong spring neap cycle (Fig. 3.5f).

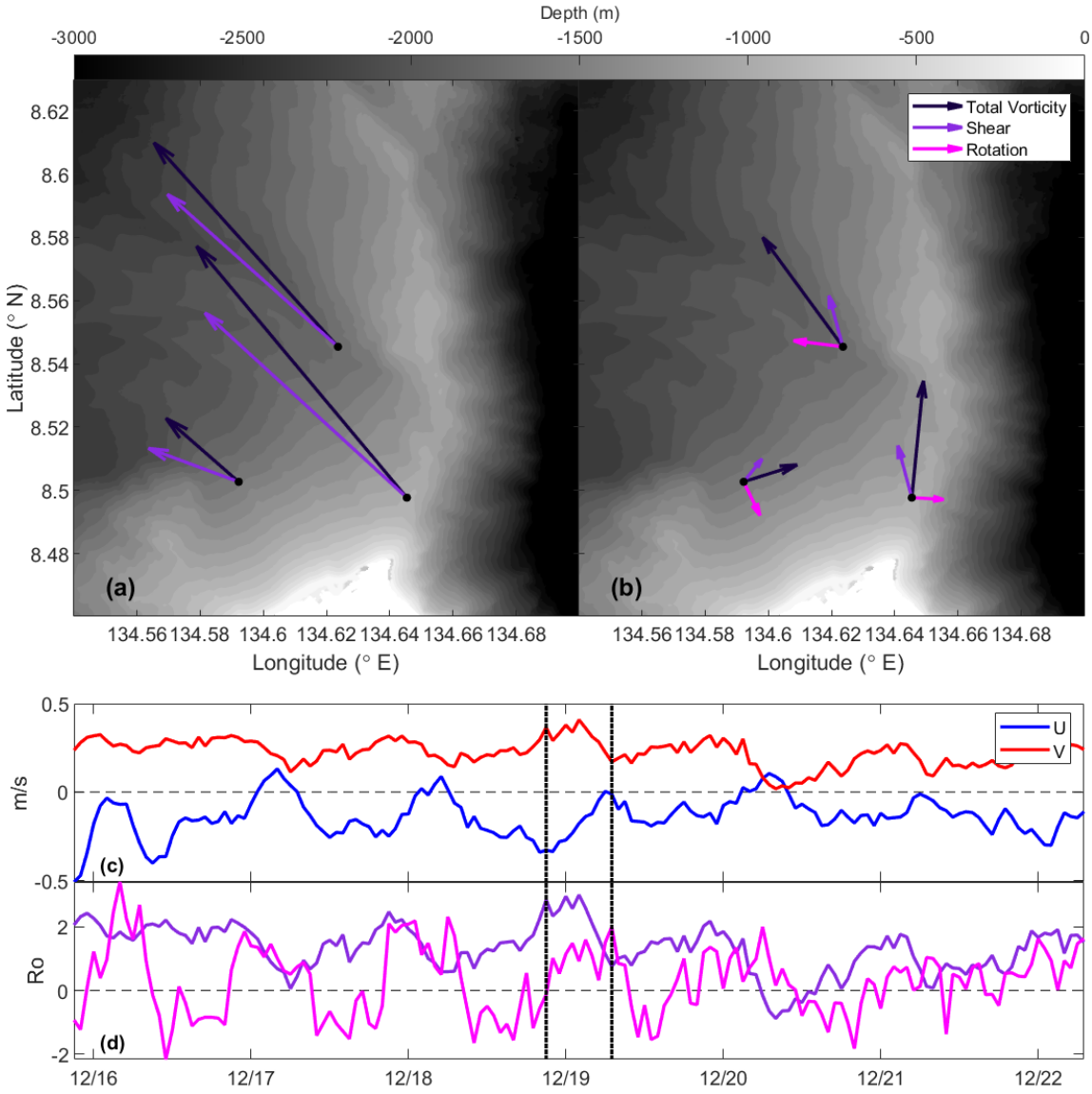

Figure 3.12: An example of surface velocity during (a) flood and (b) ebb tide during strong westward flow. Dark purple vectors in each panel are the total velocity. Purple vectors are the velocity due to the EOFs with lateral shear, and magenta vectors are velocity due to the EOF with vortex motion. A time-mean northwestward current contributes to the total velocity but is not plotted here for clarity. A 6-day window of (c) array-averaged velocity and (d) vorticity due to the shear and vortex EOFs provide context for the snapshots. Black dotted lines indicate the timing of the flood and ebb snapshots. During (a) flood tide, vorticity is due to the sheared component, but on the opposite phase of the tide (b) an eddy is released as the direction of the zonal component of the tide reverses close to the topography, cutting off the shear produced during flood tide. Note that in (a) the magenta vectors do not appear because the amplitude of the EOF with vortex motion is zero at that instance, as is indicated by the first back line in (d).

Chapter 4

Lagrangian Observations of the Palau Wake

In this study, two years of observations from Surface Velocity Program (SVP) drifters elucidate kinematic properties and downstream evolution of the wake generated by broadband flow past the Palau island chain. Between October 2016 and December 2018, 19 clusters of five SVP drifters were released from the northernmost end of the island with initial separation of 5 km. Out of these, 15 clusters were entrained in a wake to the west, reflecting time-mean westward flow past the northern end of the island. GPS positions were used to calculate downstream diffusivity, while currents derived from these positions were used to calculate vorticity via both velocity spatial gradient (least-squares fit) and timeseries methods. Drifter trajectories reveal significant variability in the wake structure. At times the drifters are entrained in energetic submesoscale eddies with peak relative vorticity up to $6f$. At others, the trajectories reveal island scale recirculation and large-scale free shear layers with vorticity O($0.1f$). Here f is the local Coriolis frequency. On average, relative vorticity in the westward wake is $1.5f$ initially, in good agreement with previous observations of vorticity in the near-field of Palau. Vorticity decreases $\propto t$, reaching $0.1f$ after $\sim$20 days. Similarly, on average cluster scale increases linearly in time,

which implies that vorticity is inversely related to scale. Upper and lower bounds for this growth are given by $t^{3/2}$ and $t^{1/2}$, respectively. We also find diffusivity is proportional to $k^{-4/3}$, where k is the inverse scale. These trends are predicted by a model of dispersion due to shear in one direction, plus stochastic dispersion in the orthogonal direction. We argue the observed time and scale dependencies of vorticity and diffusivity suggest the island-scale shear dominates dispersion and eddy growth in the wake of Palau.

4.1 Introduction

Vorticity wakes generated by flow past islands are significant to both physical and biological oceanography. Wake eddies are a source of drag and therefore momentum lost by the incident current, and they typically dominate downstream current variability (Caldeira et al., 2014). They impact biology by changing the concentration and location of nutrients (Andrade et al., 2013). Eddies may also act as a transport mechanism, moving isolated water masses and nutrients downstream of their generation site (Monismith et al., 2018). Yet substantial knowledge gaps persist due to the difficulty in obtaining high-resolution and sustained observations of what is typically an intermittent process. Two overarching open questions are (1) what are the scale and strength of wake eddies and (2) how do they evolve downstream? The observations in this study are part of a larger Office of Naval Research field campaign, Flow Encountering Abrupt Topography (FLEAT), designed to characterize the generation and properties of the Palau wake with a wide range of instruments and over a broad range of spatial and time scales (Johnston et al., 2019). Here, two years of current data from 100 surface drifters deployed into the Palau wake are used to characterize the vorticity, kinetic energy (KE) and dispersion associated with wake eddies.

Wake eddies are generated when incident currents flowing around an island meet an adverse pressure gradient on the downstream side. The current separates and vorticity generated along the coast is injected into the interior. Return flow forms in the lee to satisfy continuity

and island-scale wake eddies develop, continuously fed by the separated shear layer. When the incident flow is relatively steady, wake eddies grow until they reach island scale and are then advected downstream (Chang et al., 2013; Heywood et al., 1990). The vorticity of a wake eddy is determined primarily by its scale and the strength of the incident current. It is useful to discuss the vorticity of geophysical eddies in terms of their Rossby number, i.e. their ratio of relative to planetary vorticity (Ro = ζ/f, with $\zeta = \partial_x v - \partial_y u$). Additional variability is often present due to the complex nature of geophysical flows, but these basic principles undergird the generation of wake eddies.

Eddies in the ocean are reasonably well described as having a solid-body core which rotates at a fixed rate, surrounded by an irrotational outer region in which the velocity decays with distance (Chelton et al., 2011; Olson, 1991). Most mesoscale eddies are in quasi-geostrophic balance, meaning their momentum balance is between a pressure gradient force either away from or towards the center of the eddy and the Coriolis force in the opposing direction. By mesoscale we mean at the scale of the local Rossby radius of deformation or larger. More energetic submesoscale eddies are likely to be in cyclogeostrophic balance, where centrifugal acceleration and the Coriolis force balance the pressure gradient force. In either case, cyclonic/anticyclonic eddies rotate about low/high pressure regions. Although their kinetic energy is dominated by their azimuthal velocities, secondary circulation can develop in the form of upwelling/downwelling in the interior of cyclonic/anticyclonic eddies (Sangra et al., 2007).

The temporal evolution of wake eddies is not well observed, as their generation and downstream trajectories are difficult to predict a priori. It is a general certitude that the vorticity of isolated eddies decrease with time, but the specific processes responsible for this decay are difficult to surmise from sparse observations. Wake eddies have been tracked successfully using satellites, but this typically limits observations to mesoscale eddies. These eddies are stable on the order of months to years (Chelton et al., 2011). Submesoscale eddies typically have Ro$>$1, which means they are susceptible to rotational instabilities and likely decay much faster (Dong et al.,

2007). Some studies have tracked them using satellite images of chlorophyll, but it is difficult to derive their kinematics from these images alone (Andrade et al., 2013; Cheng et al., 2020). Drifters have been especially useful in understanding the statistical distributions of submesoscale eddies in major ocean basins (Dong et al., 2011; Li et al., 2011; Henaff et al., 2014)). However, chance encounters between drifters and eddies usually only last a few turnover timescales, and so information about the lifetime of individual eddies is not feasible. Furthermore, the error in vorticity estimated with a single drifter completing a few loops is high (Dong et al., 2011). The most detailed studies have combined observations from satellites with drifters to track eddies, however typically only one or two are sampled and their generation source is not often known (Alpers et al., 2013). To our knowledge, there have been no long term observational campaigns to track wake eddies with drifter clusters, ideal for computing vorticity, repeatedly deployed in the location they are generated.

In this study, clusters of surface drifters were repeatedly released in a location typically populated by wake eddies generated by flow past the archipelago Palau in the tropical North Pacific. Clusters were deployed over a two-year period at intervals of weeks-months, in a known submesoscale eddy generation site at the north end of the island (Wijesekera et al., 2020). Previous FLEAT studies have shown that vorticity is generated across a broad range of scales, but eddies are typically O(10km) and have Ro$>$1 close to the island (Zeiden et al., 2021; Rudnick et al., 2019; Merrifield et al., 2019). Here we use the drifters to calculate timeseries of vorticity in two ways: (1) by computing spatial gradients in the velocity field (least-squares method) and (2) by identifying peak frequencies in timeseries of velocity (via. wavelet analysis). The first calculation is done at each time-step using all drifters in a cluster, while the second is done on timeseries from individual drifters. Thus, they are truly independent methods of estimating vorticity. We will show that these methods give similar estimates of the vorticity for drifters entrained in wake eddies and use case studies to understand their differences. We also calculate diffusivity, and use this information in conjunction with the kinematics to argue large-scale shear controls the growth

of wake eddies downstream.

4.2 Data and Methods

4.2.1 Oceanographic Context

Palau is an archipelago located in the tropical North Pacific at 8 °N, 134.5 °E, roughly 1000 km due east of the Philippines. Although the archipelago is comprised of hundreds of small islands, the subsurface reef connecting them extends almost 200 km in the north-south direction and rises to 20 m at the rim (filled contour in Figure 4.1a and 4.1b). For the purposes of this study, we consider Palau a contiguous topographic obstacle (i.e., an island). Palau lies between two major surface intensified geostrophic currents; the North Equatorial current (NEC) and the North Equatorial Counter-Current (NECC) (Fig. 4.1a). Weaker undercurrents flow below the pycnocline in opposing directions, but we do not sample these currents in this study. Ocean Surface Current Analysis (OSCAR) Third Degree near-surface currents averaged over the drifter observational period (i.e., October 2016 – December 2018) show how Palau lies in a transition region between these two currents (see below for description of OSCAR data, section 4.2). At its northern and southern ends, the NEC and NECC flow westward and eastward, respectively. The NECC often recirculates to the north, connecting with the NEC east of Palau. This can bee seen in the band of northward currents between 6 and 9 °N, around 136 °E (Fig. 4.1a). The result is mean incident north-westward flow, especially at its northern end. At this latitude (8.5 °N) the NEC intensifies in the surface layer (above the mean pycnocline at about 200 m depth), with peak mean westward flow of $\sim$0.5 ms^{-1} at the surface. However, there is significant variability in the direction and speed of the incident current. The first baroclinic Rossby radius of deformation in this region is similar to the island scale (O(200 km)), so mesoscale eddies advected westward by the NEC strongly modulate the incident flow (Chelton et al., 1998; Qiu and Lukas, 1996). Timeseries of zonal and meridional velocity obtained by averaging OSCAR surface currents just north of Palau

(black box in Fig. 4.1a) demonstrates this variability (Fig. 4.1c). Incident currents range from near zero to 0.3 ms^{-1}. Downstream of the westward flow past Palau, the NEC bifurcates near the Philippine Sea and feeds the southward Mindanao Current (MC) (Schönau and Rudnick, 2017). The MC in turn connects with the NECC at $\sim$7 °N. The interannual variability of this regional circulation exceeds its annual variability, spurred by El Nino events and westward propagating Rossby waves (Qiu and Lukas, 1996). Drifter trajectories give a sense of this variability, with southward deflection occurring on the coast or as far east as 130 °E depending on these currents (Fig. 4.1b).

4.2.2 Dataset Description

In this study 19 clusters of surface drifters were released within 6 km of the tip of Velasco, a submerged reef $\sim$70 km long at the northernmost end of Palau. The incident westward flow has been shown to separate from the island at this location (MacKinnon et al., 2019; Wijesekera et al., 2020; Zeiden et al., 2021). Clusters were deployed at intervals ranging from weeks to months between October 2016 and December 2018 (denoted by thin black vertical lines in Fig. 4.1c). Each cluster consisted of 5 drifters, initially in a square configuration with a separation of 4 km. Drifters used in this study were Surface Velocity Program (SVP) drifters, which consist of a surface float connected to a Holey sock drogued at 15 m depth (Centurioni, 2018). SVP drifters have often been deployed in cluster formation to facilitate the calculation of spatial gradients (e.g Hormann et al., 2016). The drifter positions are reported via satellite using Iridium Short Burst Data (SBD) telemetry with a temporal resolution of 5 minutes. The timeseries presented in the study have been smoothed to a resolution of 1 hour using a moving Hanning window filter. Drifter lifetimes are up to 2 years, but data are only reported in this study for the first 60 days of each cluster deployment, as cluster scales reach the scale of the regional circulation as early as 20 days into the deployment (orange and red colors in the drifter trajectories in Fig. 4.1b). Velocities are calculated by finite-differencing the drifter positions in time. We supplement the drifter position

data with OSCAR surface currents. OSCAR data are provided by the Jet Propulsion Laboratory (JPL) Physical Oceanography Distributed Active Archive Center (POODAC) and developed by Earth and Space Research (ESR). Velocities combine geostrophic, Ekman and Stommel currents and do not include local acceleration and non-linearities (Bonjean and Lagerloef, 2002). Thus we use the OSCAR currents to understand the large-scale, quasi-geostrophic flow around Palau.

A goal of the FLEAT DRI is to characterize mean properties of the Palau wake. To that end we present averages of relative vorticity, kinetic energy, scale and diffusivity downstream using the full drifter dataset. To provide context for these averages, we first examine two case studies of drifter clusters entrained in eddies generated by westward flow past the island. The intention is to give examples of the structures which contribute to the mean vorticity and dispersion and understand their variance. The first case is cluster 5 (hereafter C5) which was released in November 2016 during strong north-westward flow around the island due to recirculating flow from the NECC. The wake can be seen in OSCAR surface currents averaged over the first 20 days of the deployment overlaid on corresponding kinetic energy and vorticity (Figure 4.2a and 4.2b). A region of weak flow extends $\sim$300 km downstream of the island, outlined by bands of high kinetic energy to the north and south. The drifter trajectories move in a cyclonic pattern coincident with a region of cyclonic vorticity extending west of the island (colored lines in Fig. 4.2). The second case is cluster 7 (C7) which was released in March 2017 under similar regional flow conditions, although the strength of the incident current was stronger. As a result, the wake extends to the northwest almost 600 km and the drifters were advected about twice as far downstream in the first 20 days compared to C5. The drifters in C7 also move in a cyclonic pattern coincident with a region of cyclonic vorticity extending downstream. A snapshot of sea-surface temperature (SST) over the first week of C7 from the Moderate Resolution Imaging Spectroradiometer (MODIS) on board NASA's Aqua satellite shows a strong temperature front extending northward along the wake edge, coincident with the drifter trajectories (Figure 4.3). To the northwest of the island, the strong cyclonic recirculating wake region corresponds to an SST

low. This is consistent with observations of cold-core mesoscale eddies with upwelling in their interiors (e.g Olson, 1991; Mittelstaedt, 1987; Martin and Richards, 2001).

4.2.3 Vorticity from Least-Squares Fit to Velocity

We employ two methods of estimating vorticity in this study. The first method involves the calculation of spatial gradients in velocity at each timestep using all drifters in a cluster. We first assume that velocity gradients at the scale of the cluster are linear, such that a model for the velocity of each drifter is given by

$$u_i = u_0 + \frac{\partial u_0}{\partial x}(x_i - \bar{x}) + \frac{\partial u_0}{\partial y}(y_i - \bar{y}) + u' \tag{4.1}$$

$$v_i = v_0 + \frac{\partial v_0}{\partial x}(x_i - \bar{x}) + \frac{\partial v_0}{\partial y}(y_i - \bar{y}) + v' \tag{4.2}$$

where the prime denotes the velocity due to turbulent fluctuations, and quantities with the subscript zero are assumed to vary only with time and not in space (Okubo and Ebbesmeyer, 1976; Molinari and Kirwan, 1975). Drifter positions (x_i) are with respect to their mean position ($\bar{x}$), such that $u_i = u_0$ at the center of the cluster. Turbulent velocities include any features which are unresolved by the drifter array, such as waves and finer scale eddies. The vorticity at each time step is given by $\zeta_0 = \partial v_0/\partial x - \partial u_0/\partial y$. If we further assume the drifters are entrained in an eddy, we may constrain the model to reflect solid-body rotation (Rudnick et al., 2015). In this case, the model becomes

$$u_i = u_0 + \frac{\zeta_0}{2}(y_i - \bar{y}) + u',\ v_i = v_0 + \frac{\zeta_0}{2}(x_i - \bar{x}) + v' \tag{4.3}$$

This model is also useful in the case of a simple sheared flow, although the estimate of the vorticity will be off by about a factor of 2. The solid-body fit provides an estimate of the eddy center as it moves through space, which in turn gives the distance of each drifter from the eddy

center. In the limit of shear flow, the eddy center will approach infinity, along with the drifter radial positions. In the discussion, we exploit this trait to identify an instance where a wake eddy becomes dominated by the ambient geostrophic shear (section 4.4).

In either case, the task is to solve the linear algebra problem $U = G_u X + E_u$ at each time step by minimizing the mean square of the misfit E_u. In both, U is the vector of observed zonal velocities $[u_i]$ and E is the vector of turbulent velocities $[u_i']$. In the plane-fit, X is the position matrix $[1\ x_i\ y_i]$ and G is the velocity model parameters $[u_0\ \partial_x u_0\ \partial_y u_0]'$. The solution is given by $G_u = (X'X)^{-1}X'U$, and a second identical equation is solved for the meridional component. In the solid-body-fit, one equation is solved with X given by $[1\ 0\ -y_i; 0\ 1\ x_i]$ and G by $[u_0\ v_0\ \zeta_0/2]'$. Figures 4.4a and 4.5a show results from both fits for C5 and C7, respectively. The plane-fit is plotted in blue, and the solid-body fit is plotted in magenta. Also plotted is the Okubo-Weiss (OW) parameter, defined as $OW^2 = \sigma^2 - \zeta^2$ (Okubo, 1970; Weiss, 1991). The OW is a measure of the relative strength of strain and vorticity (grey lines). Here the strain is given by $\sigma^2 = (\partial_x u + \partial_y v)^2 + (\partial_y u - \partial_x v)^2$. The sign of the OW value determines whether streamlines in the flow spiral (negative) or form nodes/saddles (positive). Thus regions of negative OW are often used to detect the presence of eddies in satellite altimetry and numerical models. In both cases, the two estimates of vorticity are in good agreement and the OW value is negative, validating our assumption that the drifters are entrained in wake eddies in approximately solid body rotation. There is greater high-frequency variance in the plane-fit estimate of vorticity (spectra not shown), which suggests that the solid body constraint acts as a filter for other high-frequency currents such as tides and inertial oscillations which do not fit the model. This effect becomes increasingly apparent as the strength of the vorticity decreases with time. Further details of these vorticity timeseries are discussed in section 4.3.1.

4.2.4 Angular Frequency from Rotary Wavelet Transformations of Velocity

The second method exploits the relationship between vorticity and angular frequency for drifters entrained in eddies with solid-body rotation, $\zeta_0 = 2\omega_0$, where ω_0 is the angular frequency. An individual drifter orbiting an eddy will have peaks in kinetic energy variance at the angular frequency of the eddy. We may expect this frequency to change with time as the drifter radial position changes and/or the kinematic properties of the eddy evolve. By performing a wavelet transformation of the complex velocity timeseries, $u + iv$, we can estimate this frequency as well its sense of rotation (anticyclonic or cyclonic). This method has been used in previous drifter studies to algorithmically identify eddies from individual drifter velocity timeseries (Lilly and Perez-Brunius, 2020). The wavelet transformation in this study follows Todd (2012). In short, the method consists of convolving a function localized in both time and frequency space with the velocity timeseries. Here we use a Morlet wavelet which is a sinusoid modulated by a Gaussian envelope, $\psi(x') = e^{i2\pi k' x'} e^{(-x')^2/2}$. The parameter *k'* controls the number of oscillations contained in each wavelet and scaling the argument *x'* changes its width (scale). By adjusting *k'* and *x'* we obtain an estimate of the time dependent energy at any desired frequency. Performing the wavelet transform of velocity over a range of wavelet scales gives the kinetic energy scalogram. The scalograms presented in this manuscript have been normalized such that integrating them returns the total variance of the original velocity timeseries. Because the vorticity generated by westward flow past Palau is cyclonic, we expect peaks in positive frequency. In section 4.3 we first give an example of the full rotary wavelet scalogram from one of the drifters in C7, and then the cyclonic component only for all drifters in the two case studies. We then present an average scalogram taken over all drifter clusters which are entrained in the westward wake.

4.2.5 Scale and Diffusivity

The change in scale of a drifter cluster with time is a direct reflection of horizontal diffusivity in the ocean (LaCasce, 2008). Here we define the cluster scale to be the mean distance of each drifter from the cluster center of mass at each time step,

$$L = \frac{1}{N}\sum_{i=1}^{N}[(x_i - \bar{x})^2 + (y_i - \bar{y})^2]^{1/2} \tag{4.4}$$

where N is the total number of drifters and x (y) is the drifter position in the zonal (meridional) direction. If the drifters were to inscribe a circle, evenly spaced, $L(t)$ would be equivalent to the circle radius. The relative diffusivity, κ is the rate of change of the squared scale with time,

$$\kappa(t) = \frac{1}{2}\frac{d}{dt}L^2(t) \tag{4.5}$$

i.e. the change in the cluster area with time (Vallis, 2006). Diffusivity is typically presented in terms of scale, as many theories give a prediction for $\kappa(k)$, where k is wavenumber. To compare with these predictions, we also compute pseudo diffusivity wavenumber spectra by binning $\kappa(t)$ by inverse scale, $k(t) = 1/L(t)$.

As noted in section 4.2.3, the model of solid-body rotation used in the least-squares fit provides an estimate of the location of the eddy center in addition to the vorticity. With this we may in turn estimate a mean radial distance of the drifters, $R(t)$. In the case of drifters evenly distributed around an ideal eddy at a fixed radius, the mean drifter position is collocated with the eddy center and $R(t)$ is equivalent to $L(t)$. In the limit of unidirectional shear, the 'eddy center' becomes nonphysically distant and $R(t) \to \infty \gg L(t)$.

4.3 Results

Here we present estimates of vorticity ($\zeta = \partial_x v - \partial_y u$) from drifter clusters entrained in the Palau wake. We first examine the two case studies introduced in section 4.2 in detail, C5 and C7. Both were released during strong westward flow past Palau and entrained into cyclonic eddies which persisted for many eddy turnover timescales (Fig. 4.2). They are therefore good candidates to compare the two methods of estimating vorticity discussed in section 4.2 (least-squares fitting and wavelet transformation). We follow with averages of vorticity, kinetic energy ($u^2 + v^2$) and scale ($L(t)$ and $R(t)$) over all clusters, whether or not an eddy was present, which were advected westward after release. In total this was 15 out of 19 clusters. We also present an average drifter velocity scalogram taken over these clusters, as well as vorticity and diffusivity binned by wavenumber (inverse cluster scale).

In this section we discuss both vorticity and angular frequency ($\omega = u_\theta / r$, where u_θ is the azimuthal eddy velocity). In the case of solid body rotation, $\zeta = 2\omega$. To help delineate between the two variables, we refer to vorticity in terms of the Rossby number, i.e. $\zeta/f \rightarrow$ Ro = C, while referring to angular frequency as a fraction of f, i.e. ω = Cf. Here C is a constant which gives the relative magnitude of either angular frequency or vorticity to the earth's rotation.

4.3.1 Vorticity Timeseries

The vorticity of eddies generated by strong westward flow past the northern end of Palau is cyclonic, initially super-inertial and decreases with time (Fig. 4.4a and 4.5a). This may be due to changes in the kinematic properties of the eddies or in the radial position of the drifters with respect to the eddy center. There are characteristics of vorticity, kinetic energy and scale common to both C5 and C7. After initial growth periods of 1 and 2 days, vorticity reaches peak values of Ro $\sim$4 and 6 for C5 and C7, respectively. In both cases, vorticity then decreases until reaching Ro = 2 about a week later (day 5 for C5, day 8 for C7). At this time, vorticity drops abruptly below

Ro = 1 and remains sub-inertial for the rest of the timeseries. There are concurrent drops in the kinetic energy (KE) of the eddy (Fig. 4.4b and 4.5b). Prior to the peak in vorticity, estimates of the drifter radial positions ($R(t)$) are unrealistically large, exceeding 100 km (Fig. 4.4c and 4.5c). However, $R(t)$ approaches the cluster scale ($L(t)$) around the time the vorticity peaks. After, both the $L(t)$ and $R(t)$ increase roughly linearly in time ($L \propto t$ plotted with black dashed lines in Fig. 4.4c and 4.5c).

There are a few notable differences in the vorticity, kinetic energy and scale timeseries of C5 and C7. During the initial super-inertial vorticity phase, C5 kinetic energy increases while vorticity decreases. Both drop abruptly on day 5. The cluster scale and mean drifter radial position increase steadily with no abrupt changes, except a short spike about 1 day after the drops in KE and vorticity. In contrast, the super-inertial vorticity and concurrent kinetic energy of C7 is more variable. There is an initial peak in both around 1.5 days, followed by steep drops (from Ro = 6 to 2, and KE = 0.35 to 0.1 m^2s^{-2}). Vorticity and kinetic energy increase sharply again around day 3, although they do not regain their initial values. Between days 4 and 8 while vorticity decreases steadily, KE also decreases. The abrupt drop in vorticity and KE on day 8 is accompanied by an abrupt increase in mean drifter radial position to unrealistic values (hundreds of km). The significance of these differences to the dynamics of each eddy are explored in section 4.4.

Briefly, we note that the initial growth in vorticity in both cases from near zero to peak values likely reflects the time it takes for drifters to become fully entrained in an eddy. Before they are distributed around the eddy center, the estimate of vorticity provided by the drifters is likely to be an underestimate, due to small velocity differences. A roll-up timescale on the order of 1-2 days is consistent with a rotation period a few times less than the local inertial period, here 3.3 days. The eddy scale given by the fit is also unrealistically high during this roll-up period, in both cases over 100 km (pink lines in Fig. 4.4c and 4.5c). The vorticity peaks when the eddy scale decreases to the scale of the drifter cluster, indicating the drifters have become fully entrained. The trends in vorticity, kinetic energy and scale which occur after this time are discussed further

in section 4.4.

4.3.2 Velocity Scalograms

Angular frequency obtained by performing a wavelet transform on complex drifter velocity provides strong confirmation of the vorticity estimated via the least-squares methods. This comparison is not typically feasible in drifter studies, because it requires the entrainment of at least three drifters in a single eddy for at least a few eddy turnover periods. Also, the predominance of cyclonic rotation caused by westward flow makes it easy to distinguish between internal waves and eddies when their vorticity is greater than f. Velocity hodographs of internal waves are clockwise (anticyclonic) in the northern hemisphere, with ellipticity that increases with frequency (Kundu and Cohen, 1990). Thus, this dataset is uniquely suited to compare the two methods.

First, a rotary wavelet scalogram from a single drifter in C7 gives an example of the asymmetry between cyclonic and anticyclonic energy induced by the presence of wake eddies (Figure 4.6). The strongest peak in KE appears in the super-inertial, sub-tidal band of cyclonic rotation in the first 10 days. This peak occurs at a period of $\sim$30 hours, or a frequency of $\sim 3f$. If we take this frequency to represent the angular frequency of the eddy which the drifter is entrained in, this corresponds to vorticity of Ro $\sim$6 (because vorticity is twice the angular frequency in the case of solid-body rotation). Thus, the estimate of vorticity provided by this single drifter is a factor of two higher than the estimate given by the least-squares fit to velocity of all drifters at each time step (Fig. 4.5a). Around day 9 the peak drops to sub-inertial frequencies and continues to decrease for the rest of the record. After day 10, KE is dominated by super-inertial anticyclonic rotation with strong peaks in the tidal bands, likely a reflection of ambient internal waves. Super-inertial cyclonic energy is comparatively weak, although the peak in cyclonic rotation persists.

Cyclonic scalograms from all five drifters in C7 compared directly with the least-squares estimate of vorticity reveal a significant amount of variability in the angular frequency given by

each (Figure 4.7a-e). The vorticity has been divided by two to give the corresponding angular frequency (pink lines in Fig. 4.7). All five drifters exhibit strong cyclonic peaks in the first 10 days in the sub-tidal, super-inertial frequency band. The decay of the peak frequency matches the trend in angular frequency from the fit, especially as seen by drifter 5 (Fig. 4.7e). The fit tends to underestimate the peak frequency, which differs by a factor of about 3 between the different drifters. In order of decreasing frequency, drifters 5, 2 and 4 give angular frequencies higher than the least-squares estimate. Drifter 1 gives the same estimate, and drifter 3 gives a lower estimate. The resulting mean peak angular frequency is broad, extending between the diurnal and inertial frequencies. The least-squares estimate of (1/2) vorticity follows its lower bound in time.

Estimates of eddy angular frequency given by cyclonic scalograms from drifters in C5 are less variable and agree well with the least-squares estimate of vorticity (Figure 4.8). There is a strong peak at $\sim 1.3f$ during the first five days of the deployment, corresponding to a vorticity of Ro ~ 2.6 during that time. The peak frequency drops below f around day 5 and continues to decay with time. The cluster-mean peak sub-inertial frequency from day 10 to day 30 is a factor of two higher than given by the solid-body constrained least-squares fit vorticity (Fig. 4.8f). This suggests that at later times there is an additional source of vorticity at the drifter scale which is not modeled well by solid-body rotation.

4.3.3 Average Wake Vorticity

In this section, we discuss average timeseries of vorticity, kinetic energy and scale obtained from drifter clusters advected westward. Out of the 19 clusters released at the north end of Palau, 15 were advected westward. Of these, seven were entrained in cyclonic wake eddies. The other eight were entrained in cyclonic shear layers extending west from the island. We identify shear layers from clusters where (1) the drifters do not rotate about their center of mass as they are advected west and (2) the eddy center given by the least-squares fit to the solid-body model is unrealistically far at all times and highly variable. Three of the eddies were initially super-inertial

(C5, C7, C13). Three were sub-inertial at all times (C9, C14, C21), and one was super-inertial only in the first day (C12, Ro $\sim$ 4). Four shear layers were weakly super-inertial in the first day (C8, C11, C16, C19 with Ro $\sim$2), but their observed vorticity dropped to sub-inertial values after. The other four shear layers were sub-inertial at all times (C4, C17, C18, C10). In two cases, one or two drifters were ejected from the cluster after a few days (C4, C10).

On average, vorticity is initially super-inertial and decays as $\zeta \propto t^{-1}$ (black line, 4.9a). This average was taken over all drifter clusters entrained in the westward wake, i.e. including both wake eddies and shear layers. Corresponding variance is plotted in gray. Cluster scale increases linearly with time, suggesting this trend is related to the vorticity decrease in time (Fig. 4.9c). Here we do not plot mean radial distances of the drifters, because this estimate becomes nonphysical in the limit of shear. Kinetic energy has no clear time dependence, ranging between 0.02 and 0.1m^{2}s^{-2} with mean value of 0.034 m^{2}s^{-2} (Fig 4.9c). This corresponds to a mean azimuthal velocity of 0.18 ms^{-1}. A pseudo enstrophy (ζ^2) wavenumber spectrum obtained by binning vorticity by inverse cluster scale confirms the inverse relationship between vorticity and scale (Figure 4.10). A best-fit line to the probability density gives a slope which corresponds to $\zeta^2 \propto k^2$.

Average rotary scalograms over the westward-advected clusters show that asymmetry between cyclonic and anticyclonic energy persists in the mean (Figure 4.11). The strongest peak in cyclonic rotation occurs within the first few days at an angular frequency of $\sim 3f$, which corresponds to a vorticity of Ro = 6. However, the peak is broad and skewed towards lower frequencies. Strong cyclonic energy is seen up to periods just slightly longer than the local inertial period. The angular frequency of the peak decreases approximately inversely with time. Although the peak angular frequency from this mean scalogram is about three times greater than that corresponding to the mean vorticity from the least-squares methods, the timeseries follows the lower bound for the first 20 days (pink line overlaid in Fig. 4.11). However, this comparison is misleading due to the bias towards energetic super-inertial eddies and shear.

4.3.4 Drifter Dispersion

Drifters are particularly well suited to calculate dispersion in the ocean, as this calculation requires no assumptions about the underlying physics. The limitation is the number of drifters, and we must keep in mind the intentional bias produced by releasing the drifters in a known eddy formation region. Nonetheless, the dependence of cluster scale on time can tell us something about the dynamics of the wake. As shown previously, the increase in drifter scale is linear with time on average. Plotting timeseries of cluster scale in log-log space reveals that at early times (less than one day) growth is exponential rather than linear (Figure 4.12b). Upper and lower bounds for times greater than one day are given by $L \propto t^{3/2}$ and $L \propto t^{1/2}$ (pink and green lines in Fig 4.12, respectively). Finally, we calculate diffusivity from each cluster (i.e., the rate of change of squared cluster scale with time) and bin the observations in diffusivity-wavenumber space to estimate the diffusivity wavenumber spectrum (Figure 4.13). Here the wavenumber is given by the inverse cluster scale, $k = 1/L$. There is a clear slope to the spectrum, estimated to be $\kappa \propto k^{4/3}$ from a least-squares fit line to the probability density function. We will discuss the significance of these dependencies on the wake dynamics in the next section.

4.4 Discussion

In this manuscript we have presented observations of the Palau wake obtained from 19 clusters of five drifters released from the northern end of Palau, a known wake eddy generation site (MacKinnon et al., 2019; Wijesekera et al., 2020; Zeiden et al., 2021). Fifteen of these clusters were advected westward after their initial deployment, reflecting time-mean westward flow past the island (Fig. 4.1). By fitting a model of solid-body rotation to the drifter velocities at each time step, we obtain timeseries of vorticity due to both eddies and free shear layers in the wake. We also compute rotary kinetic energy scalograms via. wavelet transformations to velocity timeseries from individual drifters entrained in wake eddies. Estimates of vorticity from the two

methods agree well. On average, wake vorticity is initially super-inertial and decreases inversely with time (Fig. 4.9). Kinetic energy is comparatively constant. Cluster scale increases linearly in time, which suggests that vorticity is inversely proportional to scale. This is confirmed with an enstrophy wavenumber spectrum showing $\zeta \propto k^2$ (Fig. 4.10). A similar diffusivity wavenumber spectrum shows a clear $k^{-4/3}$ slope (Fig. 4.13). Two case studies of drifter clusters entrained in wake eddies (C5 and C7) both exhibit initial periods of strong super-inertial (Ro > 1) vorticity followed by an abrupt drop to sub-inertial (Ro < 1) vorticity after approximately one week.

In this section, we use the observations from case studies C5 and C7 to estimate the scale of super-inertial eddies. We compare the observed vorticity and kinetic energy as the clusters increase in scale to the profiles predicted by a simple model of an eddy, a solid body core with an irrotational outer region (i.e. a Rankine Vortex; Kundu and Cohen, 1990). We show that the drop in vorticity (below Ro = 1) in C5 is due to drifters exiting the eddy core, but in C7 this event is due to the eddy interacting with large-scale anticyclonic shear. We then discuss the average scale of all clusters at later times and argue dispersion in the wake is dominated by large-scale shear. Finally, we use OSCAR surface currents to relate the observed wake vorticity to the flow around the island and describe conditions which lead to the generation of wake eddies.

4.4.1 Eddy Scale

We can estimate initial eddy scales for three of the super-inertial eddies from their concurrent timeseries of vorticity, kinetic energy, mean drifter radial position and cluster scale. Before exploring those observations, we make a few notes about the simple model of an eddy. Here we use the Rankine vortex, a simple mathematical model of an eddy in a viscous fluid (Kundu and Cohen, 1990) (Figure 4.14). The eddy is in solid-body rotation up to a fixed radius (R_0), beyond which the vorticity goes to zero and the azimuthal velocity decreases like r^{-1} (i.e. an irrotational vortex). The resulting radial profiles of azimuthal velocity, vorticity and (2x) angular frequency have discontinuities in their second derivatives at the eddy radius (blue lines in Fig.

4.14a,b). The dashed blue line in Fig. 4.14b shows that although vorticity goes to zero outside the core, the angular frequency is nonzero. These discontinuities are likely smoothed by viscosity in the case of a real eddy. A simple model of the smoothing effect of viscosity on the eddy profile is given by a line vortex which decays in time due to friction (Kundu and Cohen, 1990). The comparison of these two models suggests the solid-body model likely over-predicts the velocity and vorticity in the vicinity of the eddy radius. However, considering the smoothing effects of friction it is likely that the increase in velocity with radial distance is slightly less than linear and vorticity decreases with increasing distance from the eddy center.

We previously noted an abrupt drop in vorticity from super- to sub-inertial values on day 5 for C5 (Fig. 4.4a). There is a concurrent drop in KE, while both the mean drifter radial distance and cluster scale increase steadily. Prior to the drop, vorticity decreases while kinetic energy increases. This suggests that the drifters are moving outwards from the eddy center but are still within the eddy core. Our simple model of an eddy suggests kinetic energy peaks at the edge of the solid-body core. The mean drifter radial position and cluster scale are both $\sim$20 km at this time. Recall both the cluster scale and mean drifter radial position are akin to radii. Therefore, it is likely the eddy diameter is $\sim$40 km. We can estimate a radial velocity from the time it takes the drifters to reach the eddy edge, $\sim$5 days. This gives $U_r \sim 0.05$ ms^{-1}, an order of magnitude weaker than the azimuthal velocity. The drop in KE on day 5 of $\sim$0.2 ms^{-1} is sufficient to explain the change in vorticity of Ro $\sim$2, at a radius of $\sim$20 km. Another super-inertial wake eddy, (C13) has similar timeseries characteristics to C5. We estimate the scale of that eddy to also be $\sim$40 km. In that case, the drop in vorticity and KE occurs around day 7, so the corresponding radial velocity is $U_r \sim$0.03 ms^{-1}. The significance of positive radial velocities is discussed in the following section.

There is a similar concurrent drop in the vorticity and kinetic energy timeseries of C7, but key differences suggest this event is not the result of drifters exiting the eddy core (Fig. 4.5). At the same time, the mean drifter radial positions increase suddenly from 25 to 1000 km (Fig. 4.5c).

Further, kinetic energy slowly decreases before this time. We explore this event further in the following section, but these characteristics are inconsistent with the model used above. There is another sharp drop in both KE and vorticity which may instead signal drifters reaching the eddy edge around day 2, almost immediately after being entrained. As noted previously, there is significant variance in the peak angular frequency of the drifters in the first week (Fig. 4.7). The highest estimate is given by drifter 5, then 2, 4, 1 and the lowest by 3. Assuming the mean drifter position is a reasonable estimate of the eddy center, their mean radial distances are 8, 9, 12, 16 and 20 km respectively. This suggests differences in angular frequency are due to variation in their radial position, with the inner drifters having higher angular frequency than the outer drifters. Variance in angular frequency would be high for drifters orbiting around the eddy edge, which suggests a core radius of $\sim$13 km. This is also the scale of the cluster at the time of the peak in KE on day 1. We confirm this interpretation with model scalograms computed from drifters exiting an eddy core at an arbitrary velocity (Fig. 4.14c,d). Drifters inside the core overestimate the vorticity obtained from the plane fit, while drifters outside give an underestimate. In this case it is not feasible to estimate a radial velocity from the observations, since the drifters were likely deployed close to the eddy edge.

Timeseries of vorticity, KE and scale estimated from drifters entrained in the sub-inertial wake eddies do not enable the same estimate of eddy scale. In those cases, the estimate of the mean drifter radial positions are unrealistically high, suggesting that the scale of the cluster is much smaller than the eddies they are entrained in. There are no sudden kinematic shifts which signal drifters move beyond their eddy cores. It is likely these eddies are a few times larger than the super-inertial eddies described above, but they are likely limited by the scale of the island (O(100km)). The 10-40 km scale estimate for super-inertial eddies is consistent with observations from previous FLEAT studies (Rudnick et al., 2019; Merrifield et al., 2019; Zeiden et al., 2019).

4.4.2 Dynamic balance

The high Rossby numbers observed with C5, C7 and C13 suggest the balance of these eddies is likely to be cyclogeostrophic (rather than geostrophic) to first order. We confirm this using our observations to scale the horizontal momentum equations. Following (Shakespeare, 2016), the f-plane, hydrostatic Boussinesq momentum and continuity equations in cylindrical coordinates are given by

$$\frac{\partial u_r}{\partial t} + u_r\frac{\partial u_r}{\partial r} - \frac{u_\theta^2}{r} + w\frac{\partial u_r}{\partial z} - fu_\theta = -\frac{1}{\rho_0}\frac{\partial p}{\partial r} \tag{4.6}$$

$$\frac{\partial u_\theta}{\partial t} + u_r\frac{\partial u_\theta}{\partial r} + \frac{u_\theta u_r}{r} + w\frac{\partial u_\theta}{\partial z} + fu_r = 0 \tag{4.7}$$

$$\frac{1}{r}\frac{\partial (ru_r)}{\partial r} + \frac{\partial w}{\partial z} = 0 \tag{4.8}$$

Here we have assumed azimuthal symmetry, i.e. $\partial_\theta = 0$. We scale the variables as $u_\theta = Uu_\theta^*$, $r = Rr^*$, $t = (R/U)t^*$ and $z = Hz^*$, where U is the azimuthal eddy velocity, R is the eddy radius, and H is the depth of the surface layer. From our estimates in the previous section $u_r = (U/10)u_r^*$. We then obtain a scaling for the vertical velocity using the continuity equation, $w = (U/10)(H/R)w^*$. The pressure gradient close to the surface is a result of the sea-surface anomaly generated by the eddy, η. Thus we take the appropriate pressure scaling to be $p = \rho_0 g\eta p^*$. The scaled momentum equations are then

$$\frac{1}{10}\frac{U^2}{R}[\frac{\partial u_r}{\partial t}]^* + \frac{1}{100}\frac{U^2}{R}[u_r\frac{\partial u_r}{\partial r}]^* - \frac{U^2}{R}[\frac{u_\theta^2}{r}]^* + \frac{1}{100}\frac{U^2}{R}[w\frac{\partial u_r}{\partial z}]^* - fU[fu_\theta]^* = -\frac{g\eta}{r}[\frac{1}{\rho_0}\frac{\partial p}{\partial r}]^* \tag{4.9}$$

$$\frac{U^2}{R}[\frac{\partial u_\theta}{\partial t}]^* + \frac{1}{10}\frac{U^2}{R}[u_r\frac{\partial u_\theta}{\partial r}]^* + \frac{1}{10}\frac{U^2}{R}[\frac{u_\theta u_r}{r}]^* + \frac{1}{10}\frac{U^2}{R}[w\frac{\partial u_\theta}{\partial z}]^* + \frac{1}{10}fU[fu_r]^* = 0 \tag{4.10}$$

The key factor distinguishing between cyclogeostrophic and geostrophic balance is the relative strength of the centrifugal term and Coriolis term, i.e. here between U^2/R and fU. Using observations from C5, $U \sim 0.5$ ms^{-1}, $R \sim 2\text{x}10^4$ m, $f = 2\text{x}10^{-5}$ s^{-1} and $g = 10$ ms^{-2}. This gives $U^2/R = 1.25 \times 10^{-5}$, $fU = 1 \times 10^{-5}$ suggesting the balance is indeed cyclogeostrophic. The first order balance then must be

$$-\frac{u_\theta^2}{r} - fu_\theta = -\frac{1}{\rho_0}\frac{\partial p}{\partial r} \tag{4.11}$$

We do not measure sea-surface displacement in this study, but previous studies of mesoscale eddies have observed values ranging from a few to tens of cm (Yang et al., 2013). Because our eddies are submesoscale, we take a lower-end estimate to be $\eta = 5\text{x}10^{-2}$ m. This gives $g\eta/r = 2.5 \times 10^{-5}$, approximately equal to the left hand side terms.

We have observed secondary circulation in the form of a positive radial velocity. The second order balance (i.e. terms proportional to $(1/10)(U^2/R)$) is

$$u_r\frac{\partial u_\theta}{\partial r} + \frac{u_\theta u_r}{r} + w\frac{\partial u_\theta}{\partial z} + fu_r = 0 \tag{4.12}$$

Isolating the radial velocity, and recognizing that relative vorticity is given by $\zeta = \partial_r u_\theta/\partial r + u_\theta/r$, we have

$$u_r = \frac{-w\frac{\partial u_\theta}{\partial z}}{\zeta + f} \tag{4.13}$$

The denominator is positive in the case of cyclonic eddies, which means either (but not both) w or $\partial_z u_\theta$ must be negative. Cyclonic eddies in cyclogeostrophic balance are typically cold-core due to upwelling ($w > 0$) in their interiors (Sangra et al., 2007). Referring back to the snapshot of SST during the first 10 days of the C7 deployment, we note the relatively low temperature concurrent west of the island, coincident with cyclonic vorticity (Fig. 4.3). It seems likely the submesoscale eddy is similarly cold-core. This implies that the azimuthal eddy velocity is likely sub-surface intensified, commonly observed in cyclonic eddies (e.g Sangra et al., 2007).

4.4.3 Downstream Dispersion and Eddy Evolution

Downstream of Palau, wake vorticity is due to eddies as well as strong, large-scale shear layers extending westward from the island (example shown in Figure 4.17). On average, vorticity is initially super-inertial, i.e. Ro ≥ 1 within 1-2 days of initial deployment (Fig. 4.9). The free shear layers are often super-inertial at early times sampled by the drifters, and thus the vorticity variance is not simply related to differences in vorticity between wake eddies and wake shear layers. This is to be expected, as eddy formation is an intermittent process seeded by the shear generated by flow against the island. We have also shown that drifters exit the eddy cores within $\sim$1 week, concurrent with drops in the vorticity from super-inertial to sub-inertial values. Beyond the core, vorticity is inversely related to scale and KE is approximately constant (Fig. 4.9). This is inconsistent with drifters simply exiting the eddy over time, which would result in KE decreasing with increasing distance from the eddy center. In both simple models of eddy vorticity and velocity discussed above, KE and vorticity should decrease quadratically with scale (Fig. 4.14). Despite these inconsistencies, beyond the core the drifters continue to orbit cyclonically around the wake eddies as their scale separation increases (see trajectories in Fig. 4.2). These observations suggest that the eddies themselves are evolving with time.

We have shown that in addition to the mean linear growth in cluster scale with time, upper and lower bounds are given by $L \propto t^{1/2}$ and $t^{3/2}$ (Fig. 4.12). Okubo (1968) described a model of dispersion where a background linear shear is superimposed with a stochastic process in the direction orthogonal to shear. It was shown that the scale in the along and cross-shear direction increase as $t^{3/2}$ and $t^{1/2}$. The total area thus increases as t^2. This corresponds to a linear scale growth, consistent with the mean in our observations. The slope of diffusivity as a function of wavenumber observed is also consistent with shear dispersion, although $\kappa \propto L^{-4/3}$ reflects the maximum displacement (in the along-shear direction), rather than the mean scale growth. These observations suggest large-scale shear controls dispersion in the wake, and likely the growth of eddies. A classic paper by Brown and Roshko (1974) demonstrated that the growth of coherent

structures in a shear layer is on average linear in time, in part due to entrainment of ambient laminar fluid into the eddy. Entrainment of external fluid into eddies is regularly observed, visible in concentrated surfectants and chlorophyll (Munk et al., 2000). A parameter which gauges the ability of eddies to exchange fluid with the exterior ocean is the ratio of their translation speed to their azimuthal velocities (Chelton et al., 2011). If this ratio is less than one, exchange is likely to occur. A PDF of the two velocities for all observed eddies indicates that on average this parameter falls below unity, with a mean value of 0.6 (Figure 4.15). Therefore, it seems likely the Palau wake eddies entrain external fluid as they are advected downstream, growing in scale as they do so. The external shear would also act as a source of KE, explaining the constant KE with scale observed.

There is significant variance in the geostrophic currents and occasionally wake eddies may also interact with mesoscale meanders advected into the region. An example is seen when the vorticity observed by C7 drops abruptly from super-inertial to sub-inertial values (day 9, Fig. 4.5a). As previously noted, the mean drifter radial position increases sharply to a nonphysical 1000 km at the same time the vorticity becomes weakly anticyclonic. The location of the (nonphysical) eddy center during this period is to the north-east of the cluster, where OSCAR surface currents indicate the mesoscale shear is anticyclonic (Fig. 4.2d and 4.3b). It seems likely the drifters are being strained by this shear. Around day 10, the drifters resume their cyclonic rotation at a lower frequency and larger radius. It is unclear whether they are still entrained in the original eddy or have been entrained in a different cyclonic wake eddy.

4.4.4 Relationship to Incident Flow

A reasonable goal of any island wake study is to relate known incident currents to properties of the wake. In this study we are specifically concerned with vorticity and eddy generation. OSCAR surface currents averaged in three regional boxes at the southern end, east-coast and northern end of Palau give the flow around the island at the time of each cluster

deployment (Figure 4.16a-d). We compare these currents with the initial vorticity of each cluster, taken to be the mean over the first 5 days. We chose this interval to match the temporal resolution of the surface currents. This also has the effect of separating super-inertial eddies from the super-inertial shear layers. The vorticity of the shear layers drops below Ro = 1 after one day. Thus the five strongest vorticity values are due to wake eddies.

Periods of strong vorticity and eddy generation are characterized by weak north-westward flow on the eastern side of the island, and subsequent north-westward and south-westward flow around the northern and southern ends, respectively. This suggests the incident flow is coherent across the meridional extent of Palau, and forced to accelerate around both ends. In contrast, periods of weak vorticity and no eddy generation are characterized by much stronger currents past both the northern and southern ends, but in opposing directions. Flow is eastward to the south and westward to the north. Currents just east of the island are weak and variable. To visualize these patterns, the flows producing the strongest and weakest wake vorticity are shown in Fig. 4.16 (right panels). The strongest wake eddy observed was generated by recirculation from the NECC, which is $\sim$200 km south of Palau. The incident current is a north-westward jet which flows around both ends of the island. An island-scale anticyclonic wake eddy can be seen west of Palau. In the second case, westward flow only eclipses the northern end of Palau. The NECC is more northward, flowing eastward past the southern end. On the eastern side of the island currents are weak, and there is an island scale region of cyclonic circulation. In this scenario there is no coherent flow past the island.

These patterns of flow appear to be characteristic of the mean in both cases. This is confirmed with surface currents averaged over flows which generated either wake eddies or shear layers (Figure 4.17a,c and b,d respectively). Eddies are generated when the incident current is north-westward, diverges around 8N, and flows eastward around both ends of the island. This flow blocking necessarily creates a pressure gradient across the island, which leads to flow separation at either end. Twin regions of cyclonic and anticyclonic vorticity develop in the lee. Thus wake

vorticity is generated by the westward flow impinging on the island. In contrast, the observed free shear layer is due to regional-scale cyclonic circulation moving around the island. Flow is not blocked, so no pressure differential is created and no appreciable additional vorticity generated. In a study of the interannual current variability around Palau, Heron et al. (2006) observe this same intense cyclonic circulation and attribute it to an annual zonal elongation of the Mindanao Eddy in the first half of the year. This is consistent with our observations, as shear layers were only sampled between January and June. Out of the seven wake eddies observed, five were generated in the second half of the year, when the NECC is to the south and the ME sits far west of the island.

In sum, the conditions leading to the generation of wake eddies in the lee of Palau are coherent westward flow around both ends of the island. The position of the current with respect to the island has a first order influence on the development of an island scale wake and the strength of vorticity downstream. The generation of wake eddies requires flow blocking and separation. Due to strong variance in the regional circulation, it seems likely that wake eddies are preferentially generated when the NECC moves south in the second half of the year.

4.5 Summary

In this study we have presented observations from clusters of drifters released over a two-year period at the northern end of the island Palau, where the incident large-scale flow separates from the island. These clusters were often entrained in cyclonic wake eddies, and at other times advected downstream in cyclonic large-scale shear layers. We calculated vorticity from the drifters' velocity in two ways: (1) by computing spatial gradients in the velocity field and (2) by identifying peak frequencies in timeseries of velocity. Eddies were often super-inertial, i.e. with $\mathrm{Ro} > 1$, and O(10) km in scale. They are likely in cyclogeostrophic balance, with a secondary circulation consisting of upwelling in their interiors and a weak positive radial velocity

at the surface. This velocity caused drifters to exit their cores on the order of 1 week. Weaker, sub-inertial eddies were larger, up to O(100km). Vorticity in the shear layers was sub-inertial. Averaged over all clusters advected into the Palau wake, vorticity is inversely dependent on cluster scale, which in turn increased linearly with time ($L \propto t$). In contrast, kinetic energy is not dependent on scale or time. Upper and lower bounds for the cluster scale growth were given by $L \propto t^{3/2}$ and $t^{1/2}$, and diffusivity increases with scale $\kappa \propto L^{4/3}$. These observations suggest that shear dynamics dominate dispersion in the wake of Palau, including the growth of wake eddies downstream. OSCAR surface currents reveal that while wake eddies are the result of flow blocking when currents are directly incident on the island, the observed shear layers were part of a regional-scale cyclonic circulation around Palau and thus their vorticity was not generated by flow past the island. It is likely wake eddies are preferentially generated in the second half of the year, due to annual changes in the regional flow around Palau.

4.6 Acknowledgments

This work was funded by Office of Naval Research under Grants N00014-15-1-2286, N00014-17-1-2517 and the National Oceanic and Atmospheric Administration under Grant NA15OAR4320071. Thank you to the engineers of the Lagrangian Drifter group at the Scripps Institution of Oceanography who were instrumental in the development and preparation of the drifters. We are very grateful to Pat and Lori Colin from the Coral Reef Research Foundation in Palau for the deployment of numerous drifters and their support with the local community.

Chapter 4, in full, consists of material that is being prepared for submission for publication in the Journal of Physical Oceanography, Zeiden, K.L., D.L. Rudnick, J.A. MacKinnon, V. Hormann and L. Centurioni (In Preparation) Lagrangian Observations of the Palau Wake. The dissertation author was the primary investigator and author of this paper.

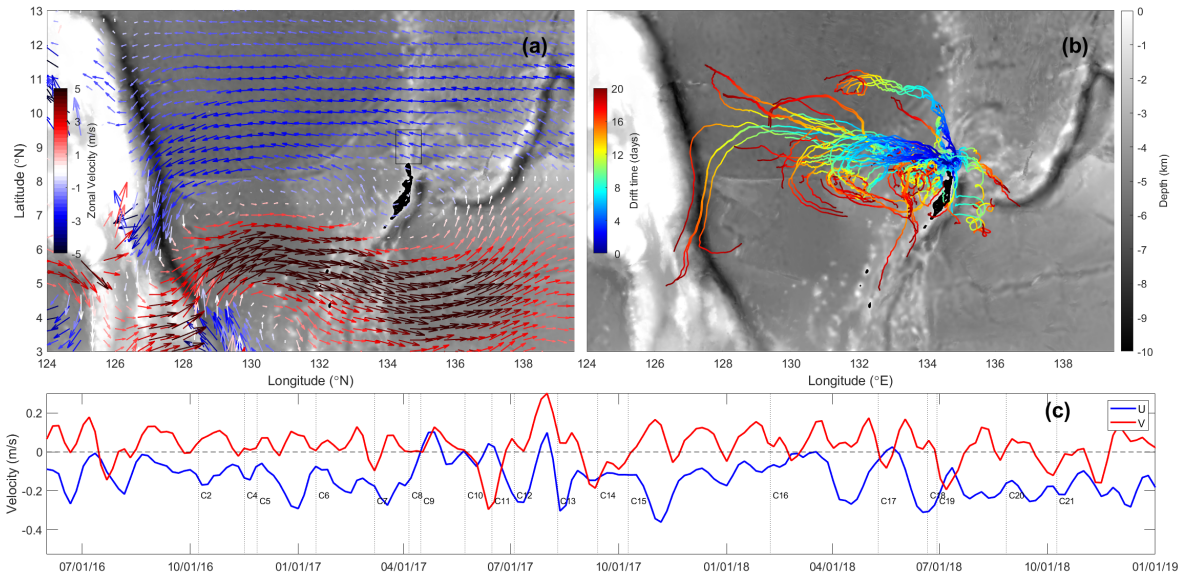

Figure 4.1: Regional bathymetry overlaid with (a) mean OSCAR surface currents over the observational period (October 2016 - December 2018) and (b) drifter trajectories over the first 20 days of each release period. Currents are $1/3°$ resolution. Quivers in (a) are colored by zonal velocity magnitude, with red/blue indicating eastward/westward. Drifter trajectories are colored by time, referenced to their initial release. Current conditions during each release are plotted in (c) by averaging OSCAR surface currents in a region just north of Palau (black box in (a)). To the north of Palau the NEC flows westward, while to the south the NECC flows eastward. Drifters were deployed in a diamond grid pattern at the northern tip of Palau, and were advected westward by the NEC on average.

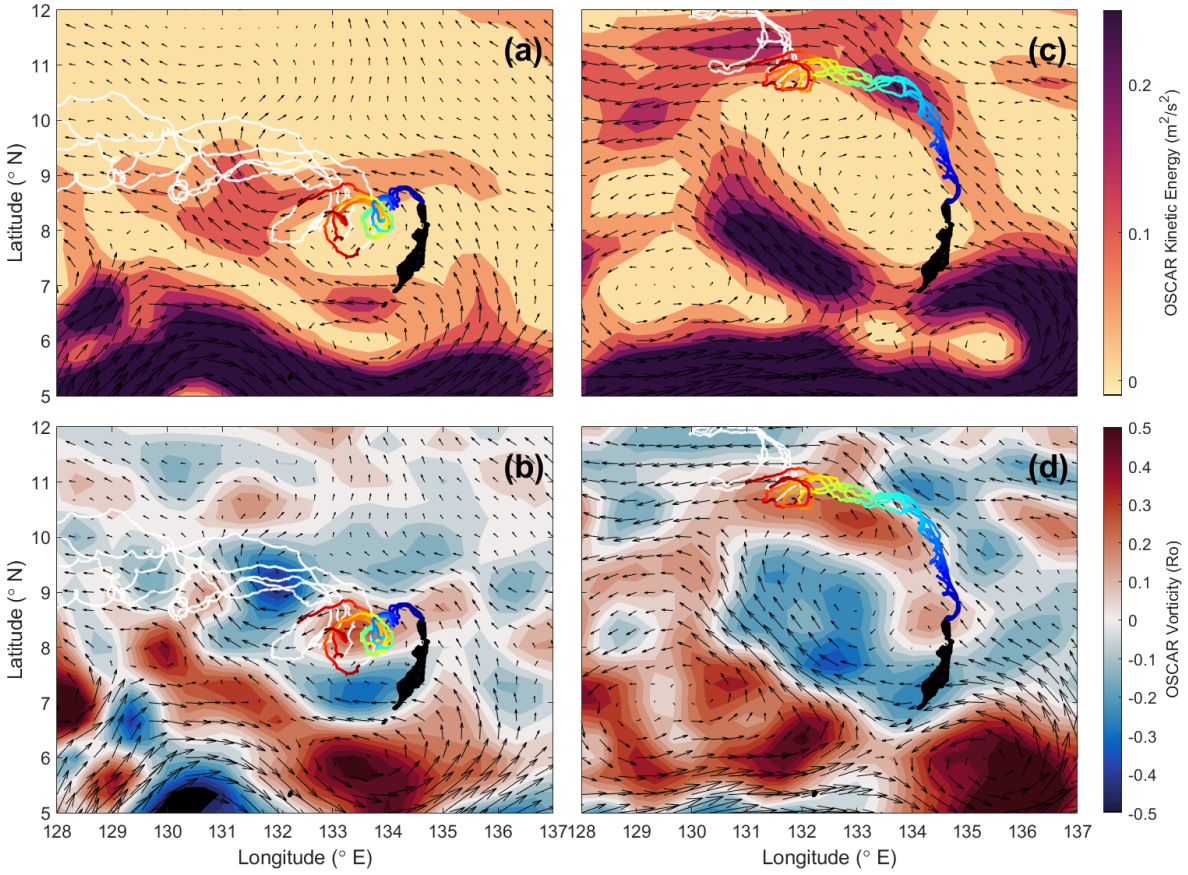

Figure 4.2: Mean OSCAR surface currents averaged over the first 20 deployment days of (a,b) C7 (March 2017) and (c,d) C5 (November 2016). Contoured value in (a,c) is horizontal kinetic energy. Contoured value in (b,d) is vorticity normalized by the local Coriolis frequency. Overlaid in (a,b) are the drifter trajectories for the first 20 days (colored lines). The colorbar corresponding to these trajectories is the same as in Fig. 1. The Palau wake is evident during both periods in weak downstream KE, and anticyclonic (cyclonic) vorticity to the west of the southern (northern) ends of the island. Stronger incident currents during the release of C7 lead to a wake that is almost twice as long as during C5.

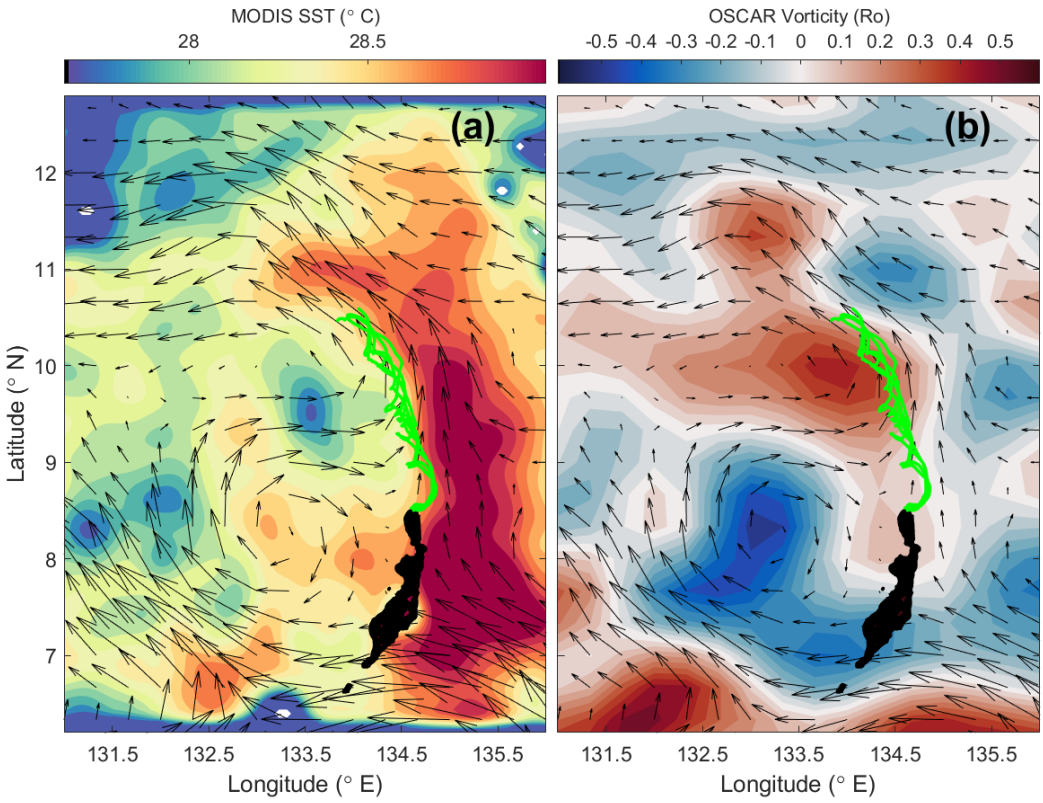

Figure 4.3: (a) MODIS sea-surface temperature averaged over the first 8 days of C7 and (b) vorticity from OSCAR surface currents averaged over the same period. Black quivers in both are corresponding OSCAR velocity vectors, and green lines are the trajectories of the drifters. Warm surface water is advected towards the island and accelerated around it's northern end, providing a clear outline of the wake region. To the north-west of the island, a region of cyclonic circulation is coincident with cooler surface temperature.

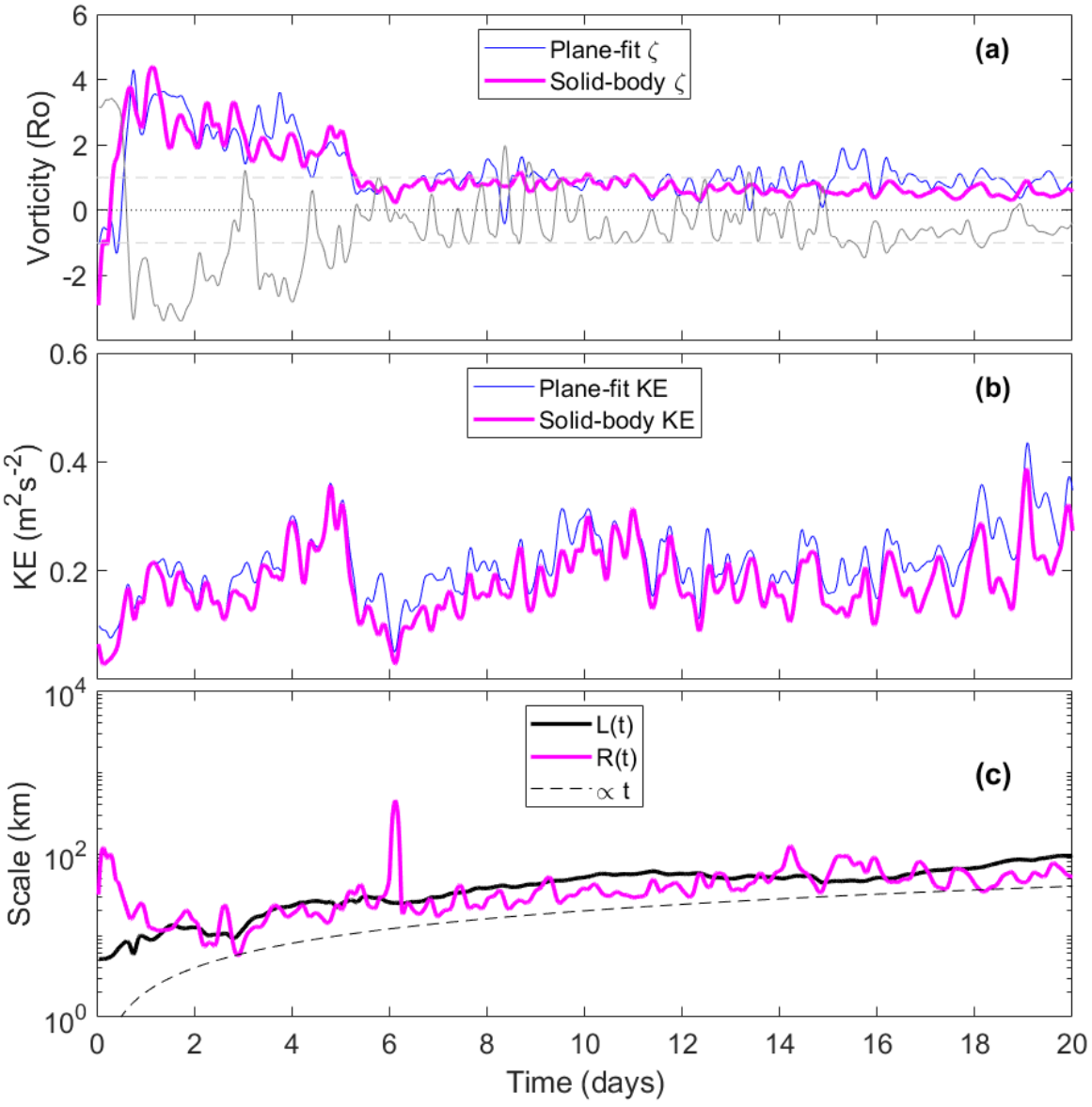

Figure 4.4: Vorticity, KE and scale for C5. (a) Vorticity is estimated using two least-squares fits to the velocity data: (1) fitting a plane to the velocity of each drifter at each time step (blue lines) and (2) fitting solid-body rotation (magenta lines). Grey line in (a) is the Okubo-Weiss (OW) value obtained from the plane-fit. Kinetic energy (b) is the mean squared velocity obtained from the fit, which gives the eddy azimuthal velocity in the case of solid-body rotation. In (c) the mean drifter radial distance with respect to the estimated eddy center (magenta) is compared to the cluster scale (black line). Dashed black line in (c) gives scale growth $\propto t$ for comparison.

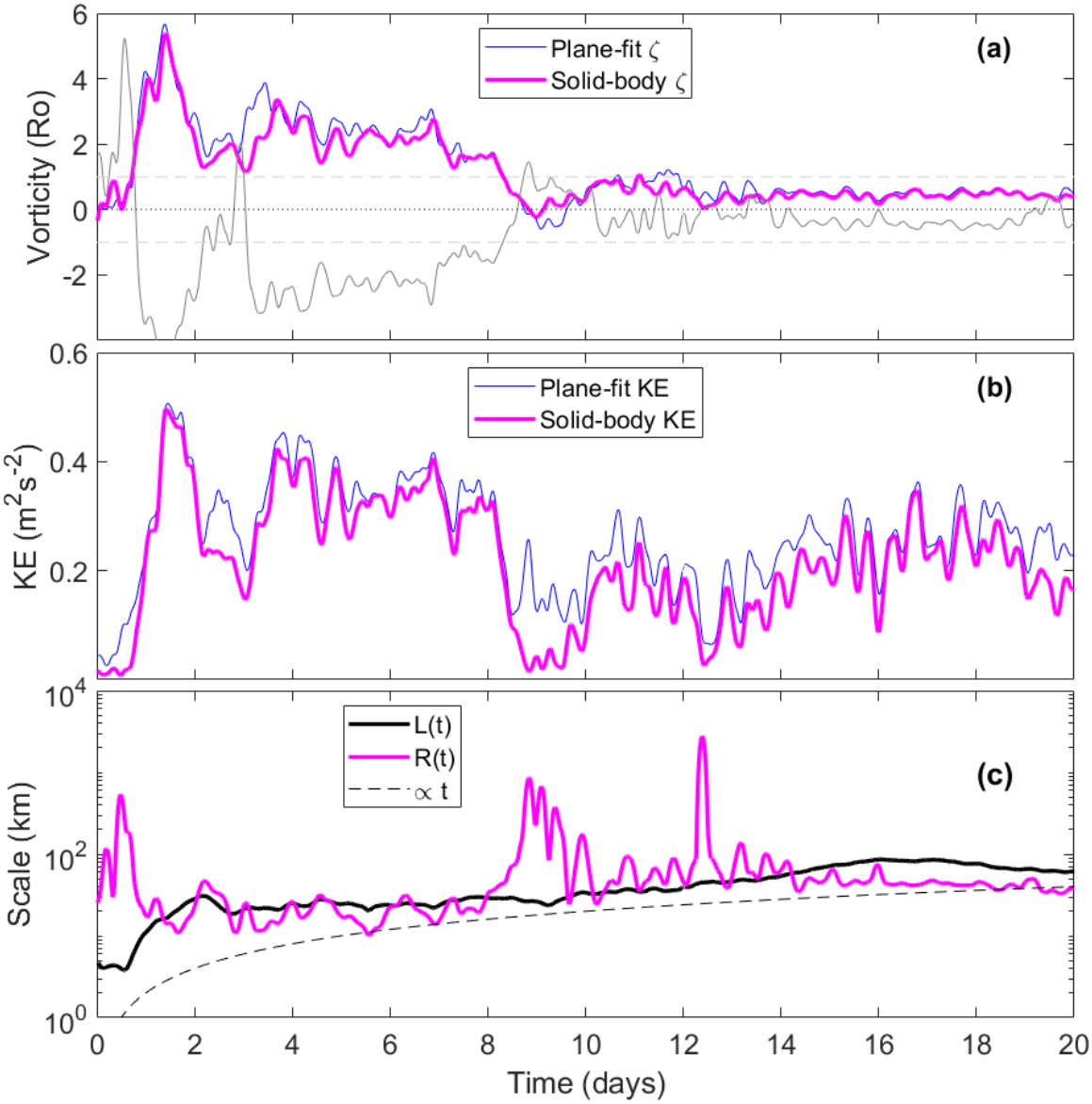

Figure 4.5: As in Fig. 4, but for C7.

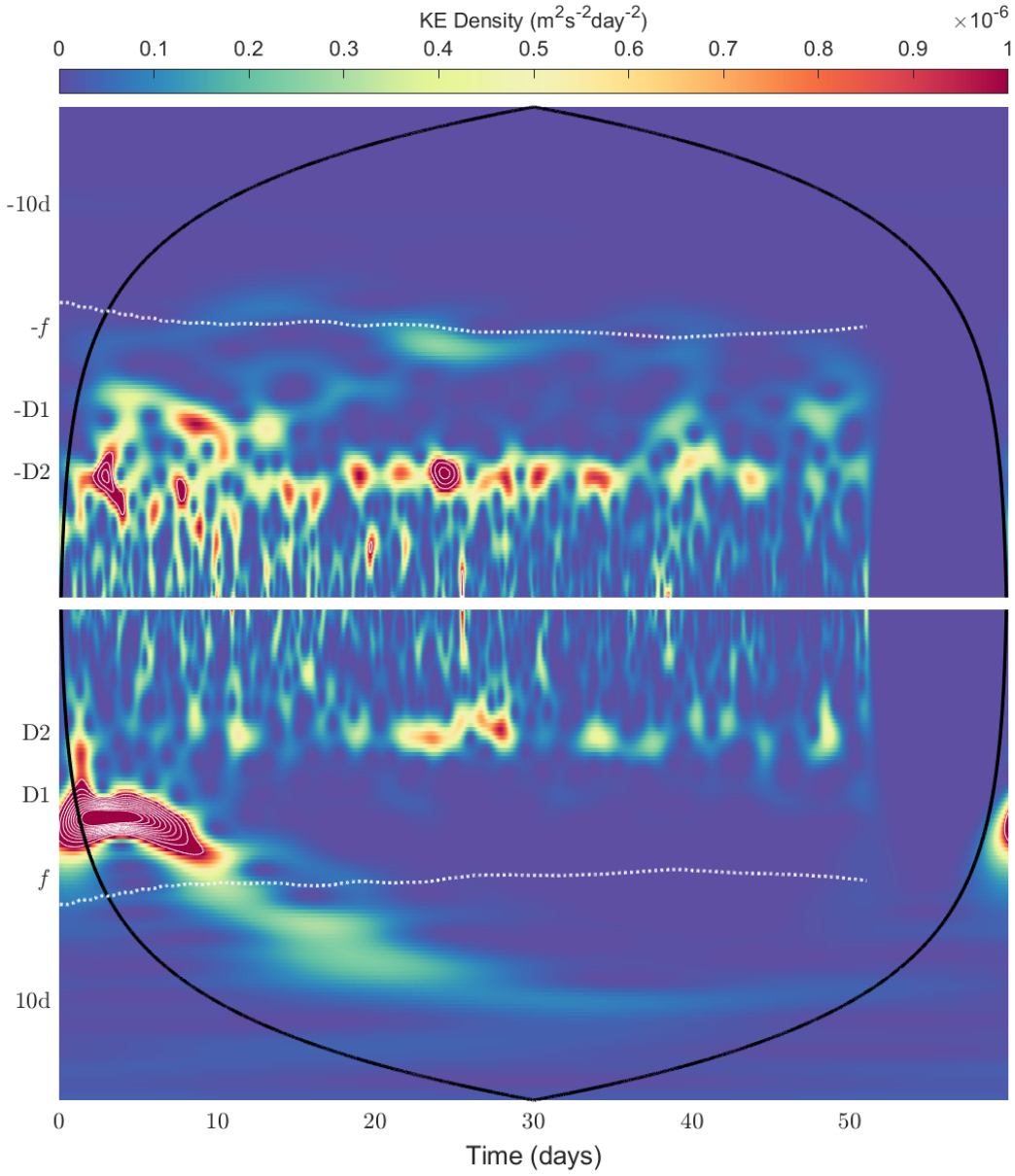

Figure 4.6: Example rotary wavelet scalogram for Drifter 5 in C7, showing (a) anticyclonic rotation and (b) cyclonic rotation. White dotted lines indicate the local Coriolis frequency, which changes as the drifter moves north or south. Black lines indicate the region possibly contaminated by edge effects. Vertical axis labels D1 and D2 indicate the diurnal and semi-diurnal tidal periods, respectively. Anticyclonic rotation is dominated by strong peaks in the semi-diurnal band, and there are no energetic peaks at frequencies lower than the inertial frequency. Cyclonic rotation is dominated by a strong super-inertial peak which decays with time, and moves to lower frequencies.

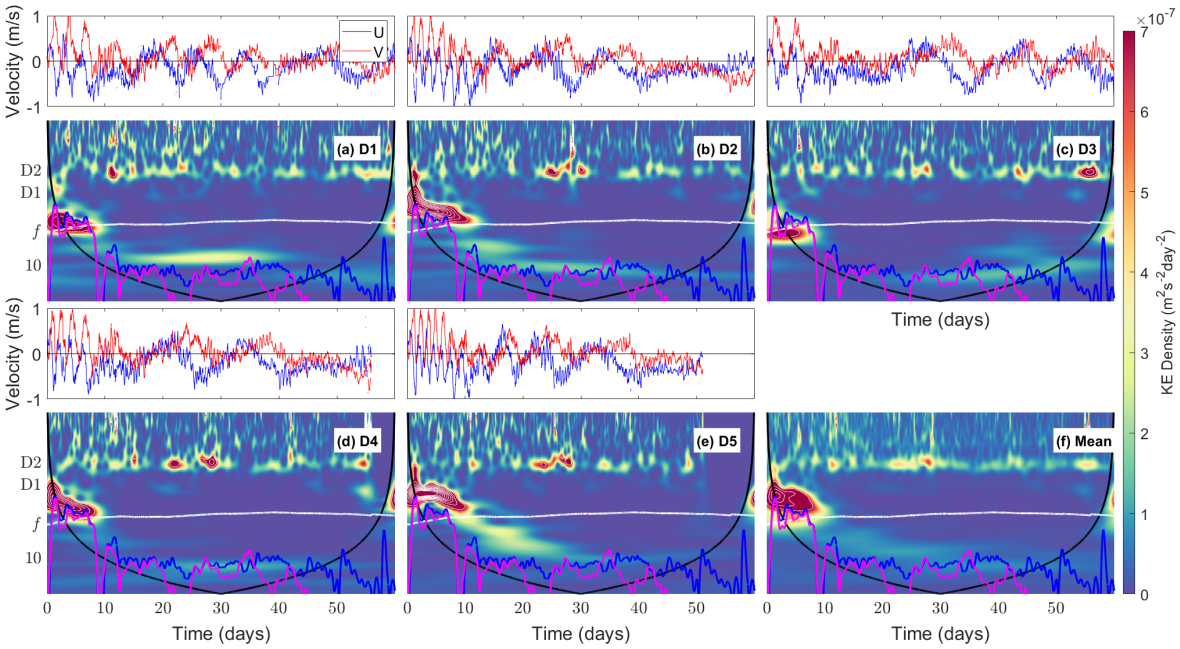

Figure 4.7: Cyclonic rotary wavelets for (a-e) all drifters in C7 as well as (f) their average. Plotting scheme is the same as in Fig. 4. Rotational period (i.e. half the vorticity) estimate for C7 from the plane-fit (blue lines) and solid-body fit (magenta line) are overlaid in each. Strong cyclonic rotation occurs at initial periods which range between the diurnal and inertial period. On average, the initial rotational period is super-inertial and the trend compares well with estimates from the plane-fit to all drifters

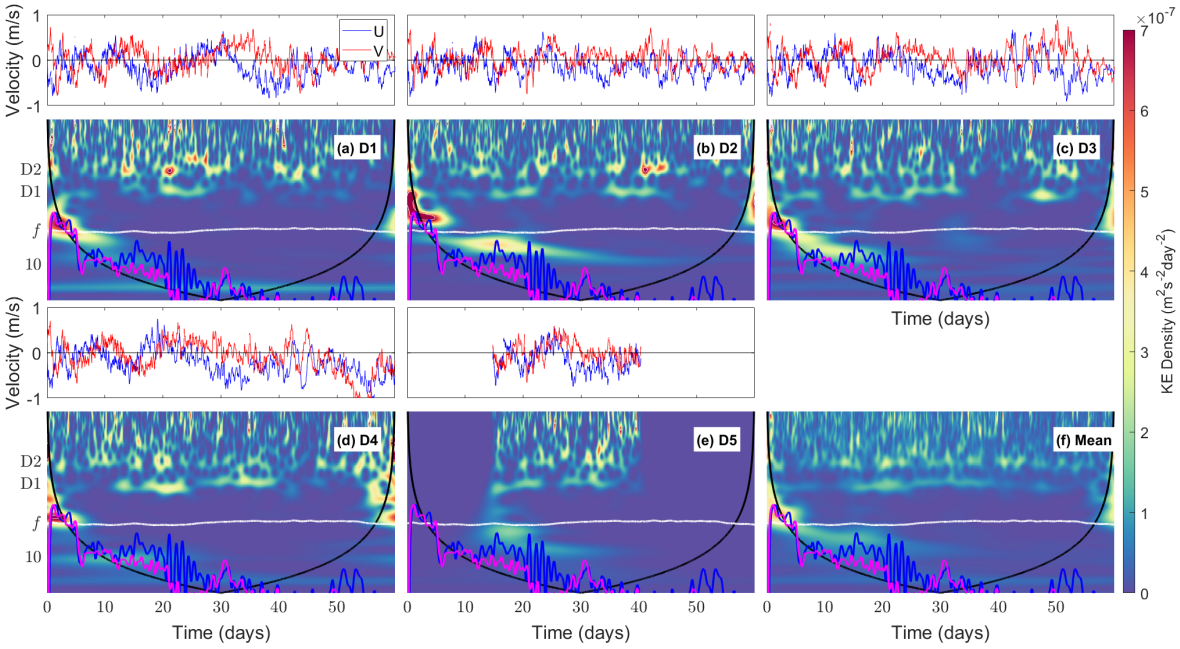

Figure 4.8: As in Fig. 5, but for C5. The fifth drifter did not record data for the first 10 days and final 20 days. Initial vorticity for all drifters is just slightly super-inertial. The variance in initial rotational period is less than for C7.

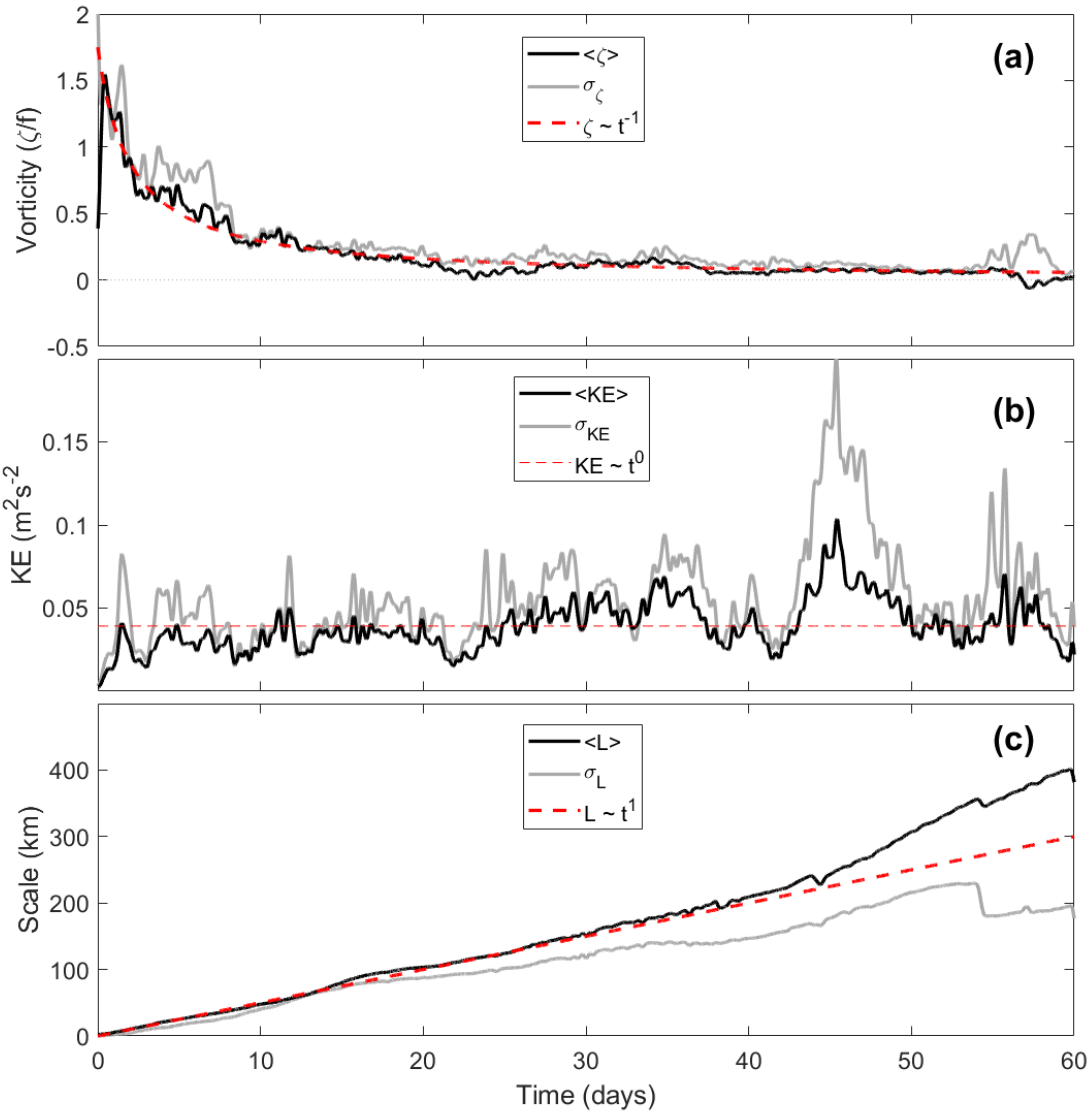

Figure 4.9: Averages of (a) vorticity, (b) kinetic energy and (c) cluster scale taken over all drifter clusters which were advected westward. Grey lines in all are standard deviation. Red dashed lines are (a) vorticity inversely related to time (t), (b) kinetic energy constant in time, and (c) scale increasing linearly with time for comparison.

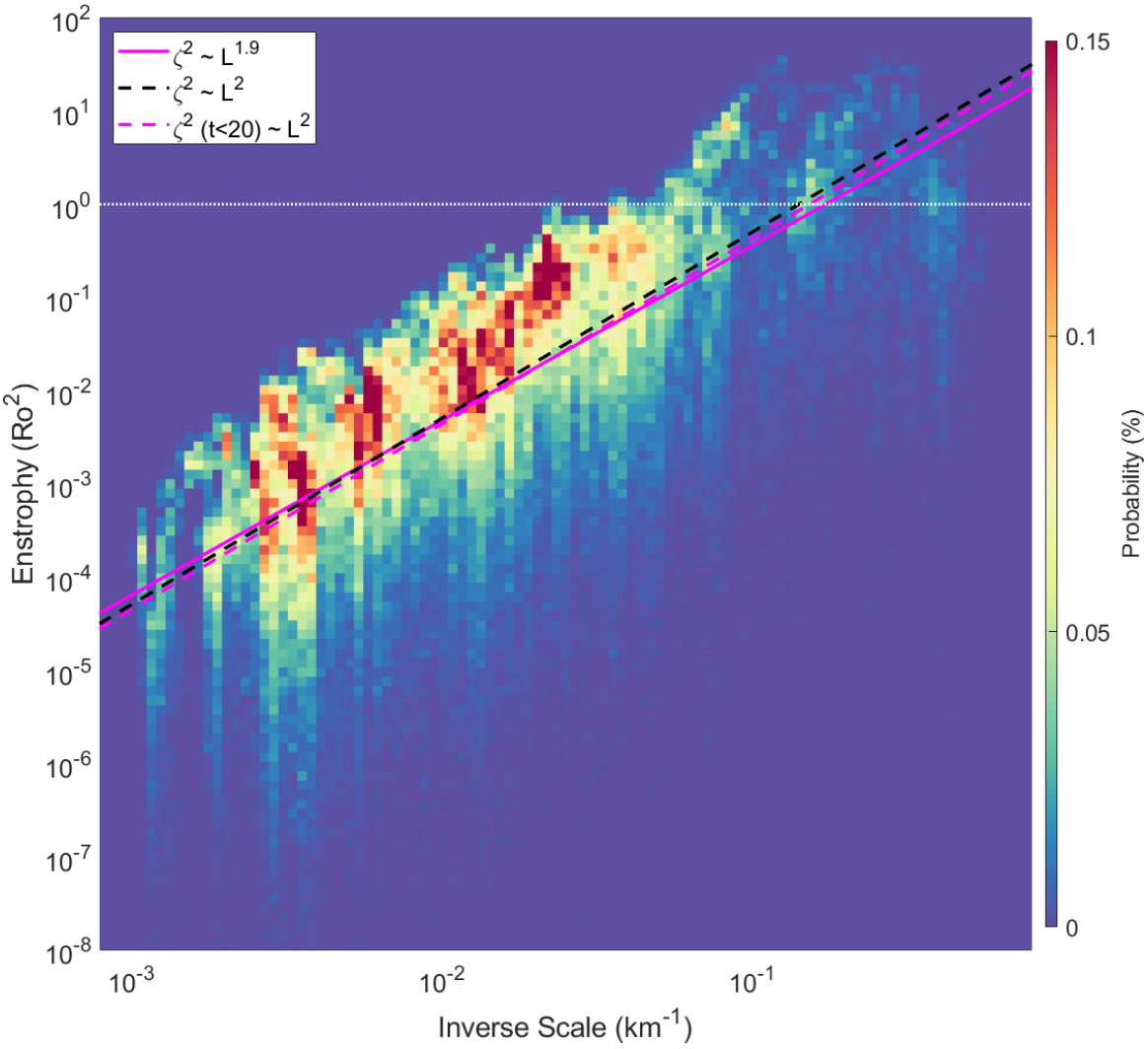

Figure 4.10: Enstrophy (vorticity squared) from all westward clusters binned by wavenumber (inverse scale). A least-squares fit trend to the data gives a power law of $\zeta \propto k^{1.9}$ (pink line). Restricting the fit to data collected in the first 20 days of each deployment gives $\zeta \propto k^{2}$. The white dashed line indicates Ro = 1.

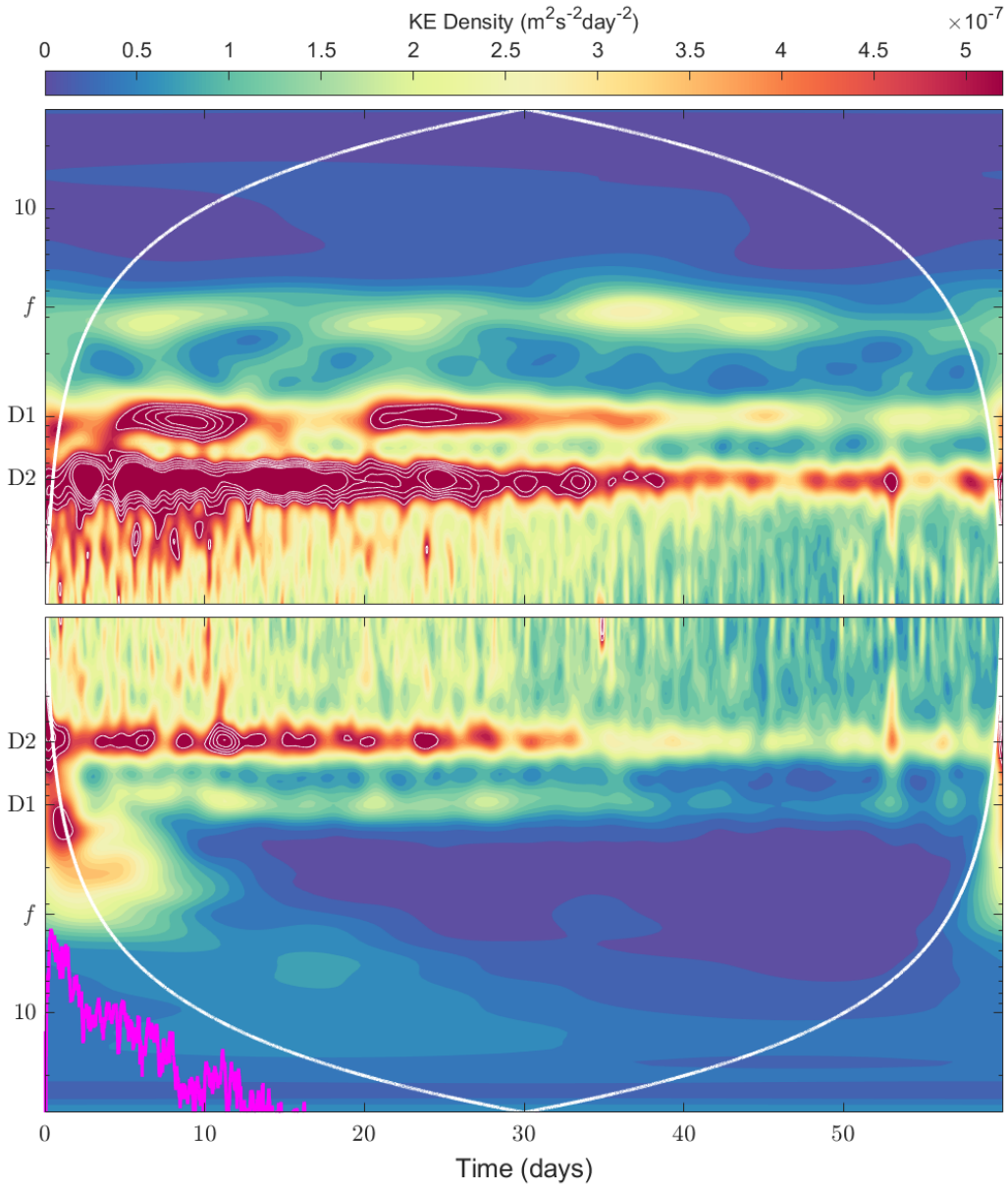

Figure 4.11: As in Fig. 6, but averaged over every drifter cluster which was initially advected westward. The average (1/2) vorticity obtained via. least-squares fit to the model of solid-body rotation is plotted in magenta. The scalogram shows on average, there is a strong initial peak in rotational period of about 2.5 days which decays inversely with time. The vorticity follows the lower bound of this peak in time. This is a reflection of the greater energy of super-inertial eddies, which dominate the mean scalogram.

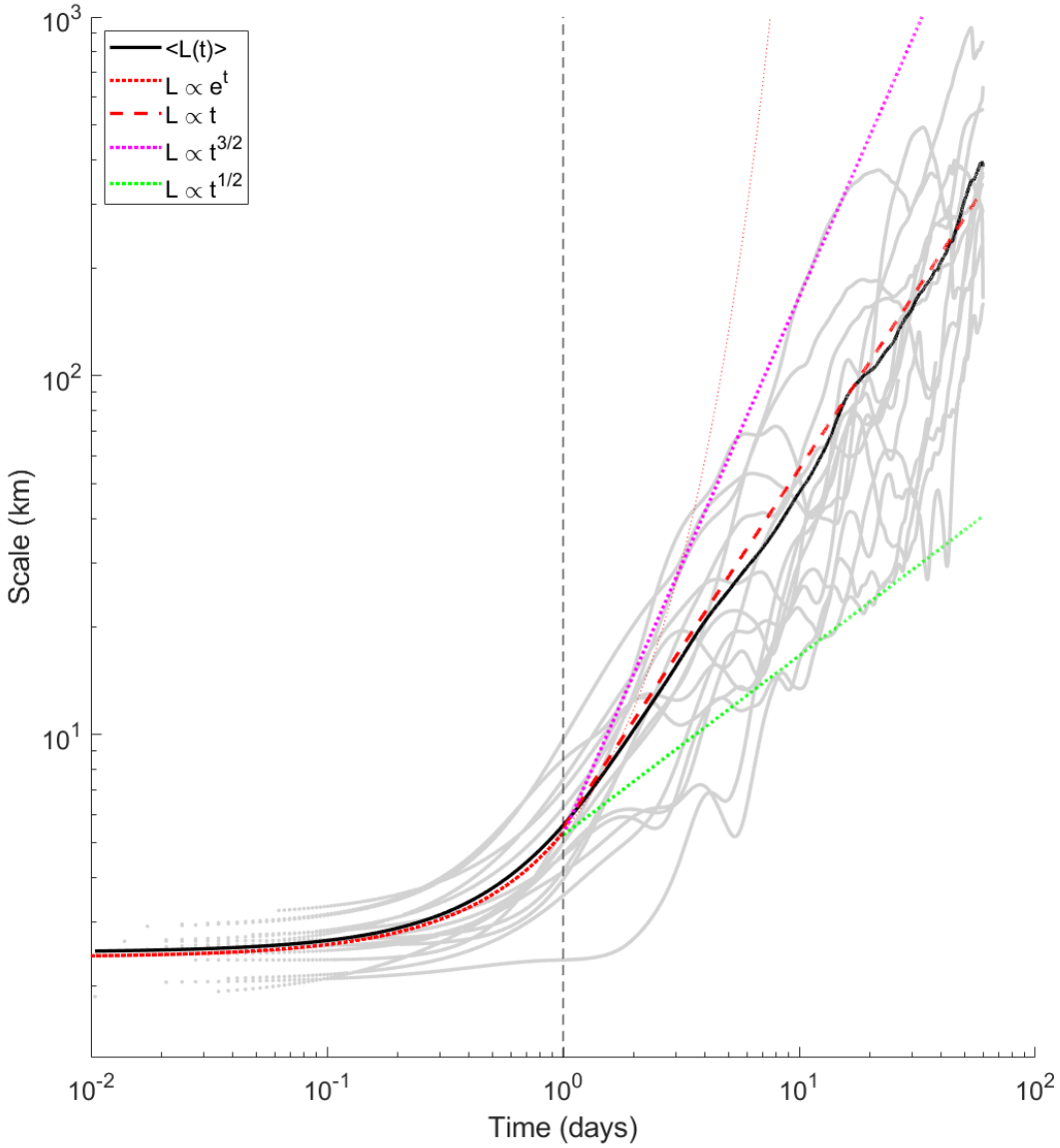

Figure 4.12: Cluster scale $L(t)$ for each cluster advected westward. Averages over all clusters are overlaid in black as well as theoretical curves for initial exponential growth over the first day (red dotted lines) and linear growth at times greater than a day (red dashed line). Linear scale growth is consistent with along-stream shear dispersion combined with cross-stream stochastic dispersion (LaCase 2008). Upper and lower bounds are given by theoretical curves for shear dispersion ($t^{3/2}$, pink dotted line) and stochastic dispersion ($t^{1/2}$, green dotted line).

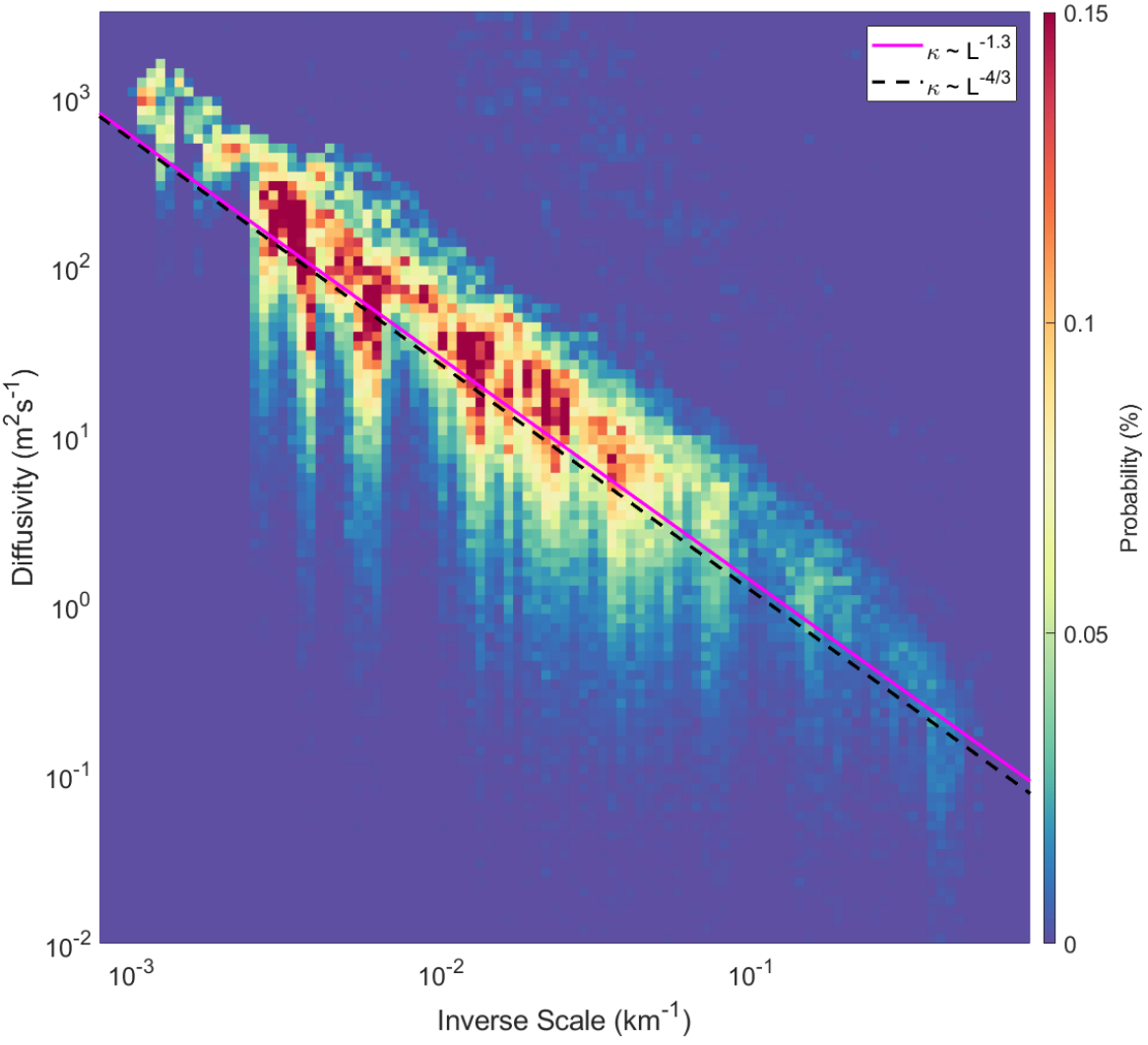

Figure 4.13: Diffusivity (rate-of-change of L^2) from all westward clusters binned by wavenumber ($k = L^{-1}$). A least-squares fit trend to the data gives a power law of $\kappa \propto k^{-1.3}$ (pink line). Theoretical curve for shear dispersion $\kappa \propto k^{-4/3}$ plotted in black.

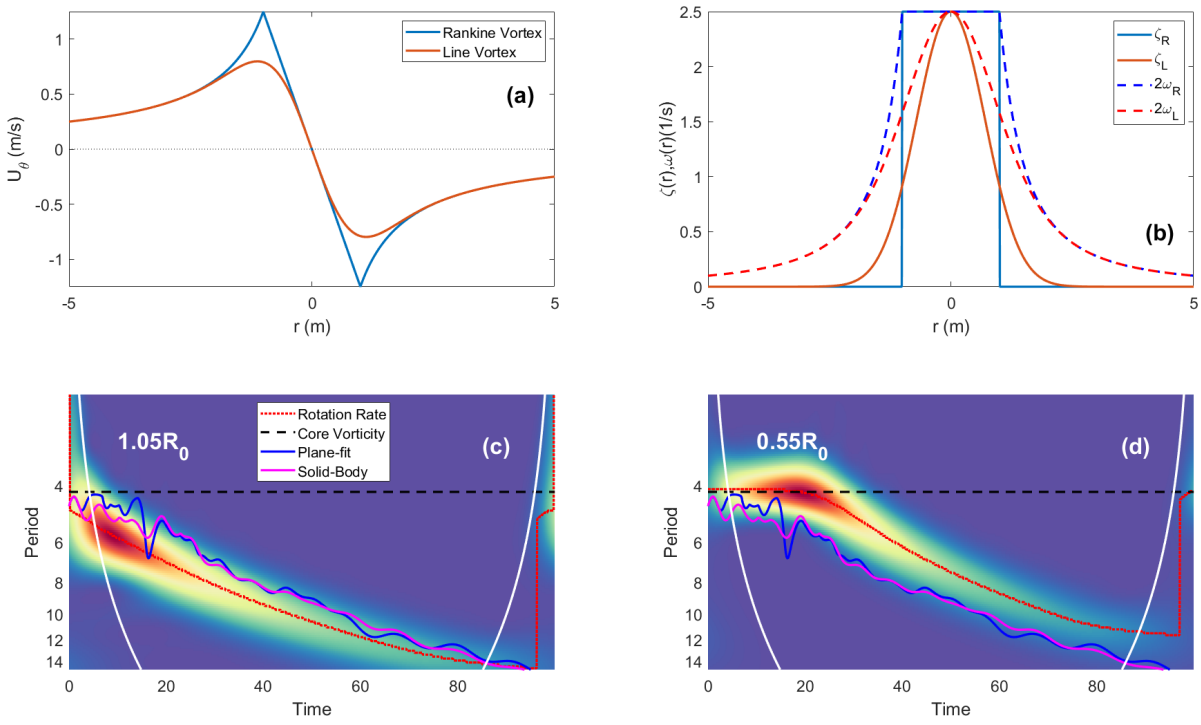

Figure 4.14: (a) Azimuthal velocity for two eddy models, a Rankine vortex (solid body plus irrotational core) (blue line), and a line vortex smoothed by friction (red line). (b) Corresponding vorticity (solid lines) and angular frequency (dashed lines) for each model. (c,d) Model kinetic energy scalograms from two drifters moving outwards from a Rankine vortex due to an arbitrary positive radial velocity. One was deployed (c) outside the vortex core and the other (d) inside. Black dashed line in each is the core rotation rate and the red dotted line is the rotation rate at the drifter position. The pink and blue lines in each are rotation rate obtained from a least-squares plane-fit (blue) and solid-body fit (pink) to a cluster of 5 synthetic drifters.

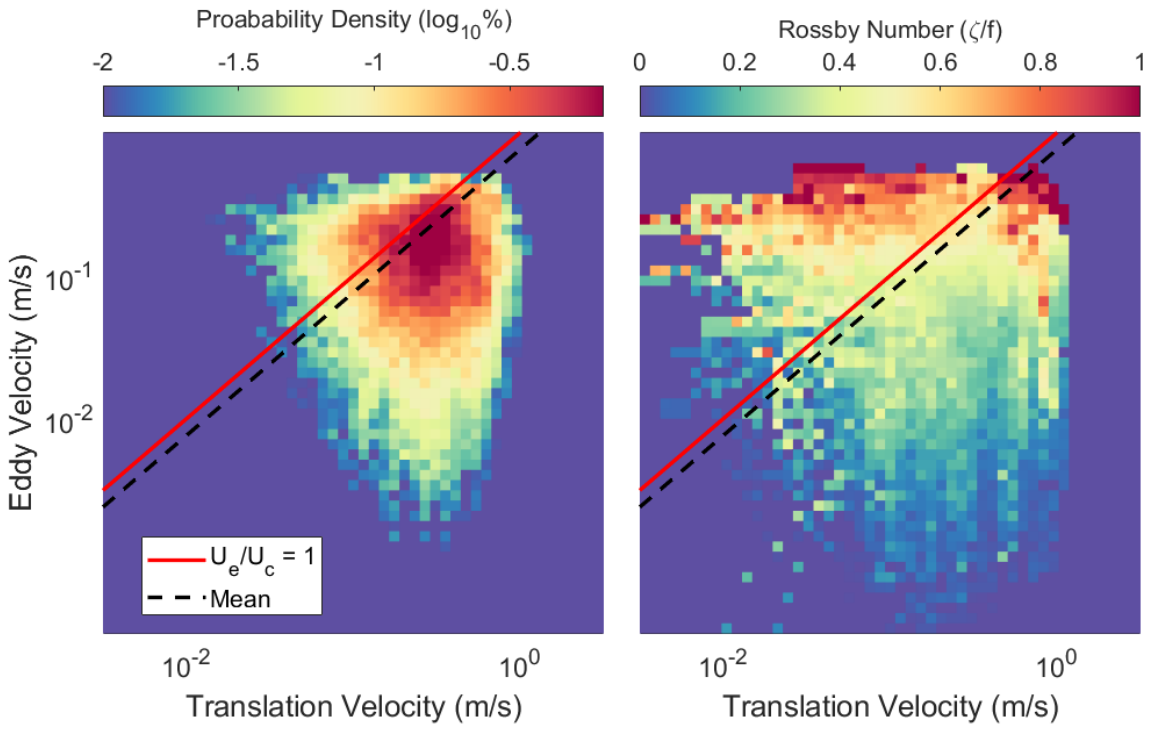

Figure 4.15: (a) Probability density function of number of observations binned by eddy azimuthal velocity (U_e) and translation speed (U_c). The ratio of these values gives a non-linearity parameter which indicates whether eddies are likely to exchange fluid with the exterior region (yes if $U_e/U_c < 1$). (b) The same, but with vorticity as the binned variable.

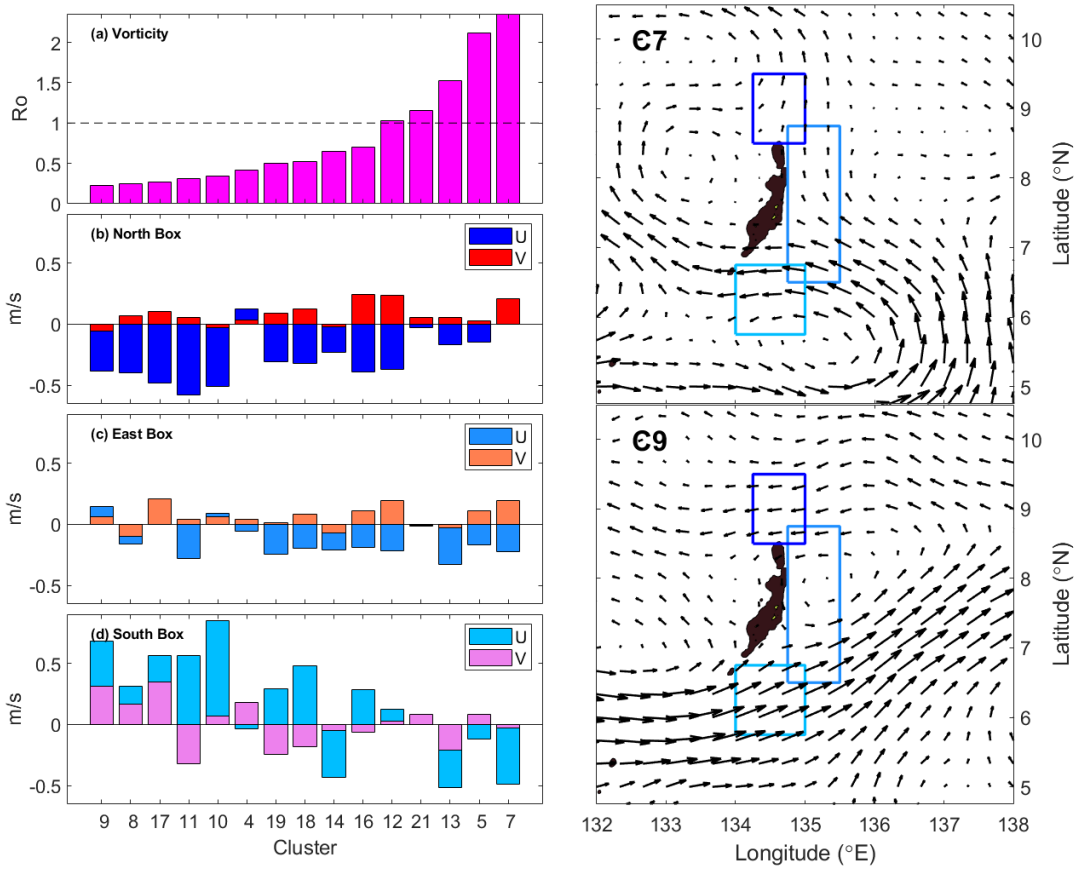

Figure 4.16: (a) Initial wake vorticity (0-5 days) for each cluster advected westward, (b) initial OSCAR surface currents at the north end, (c) east side and (d) south end of Palau during each release. Currents are averaged in the regions indicated with boxes in the quiver plots on the right. These quiver plots show the surface currents which generated the weakest (C9) and strongest (C7) wake vorticity.

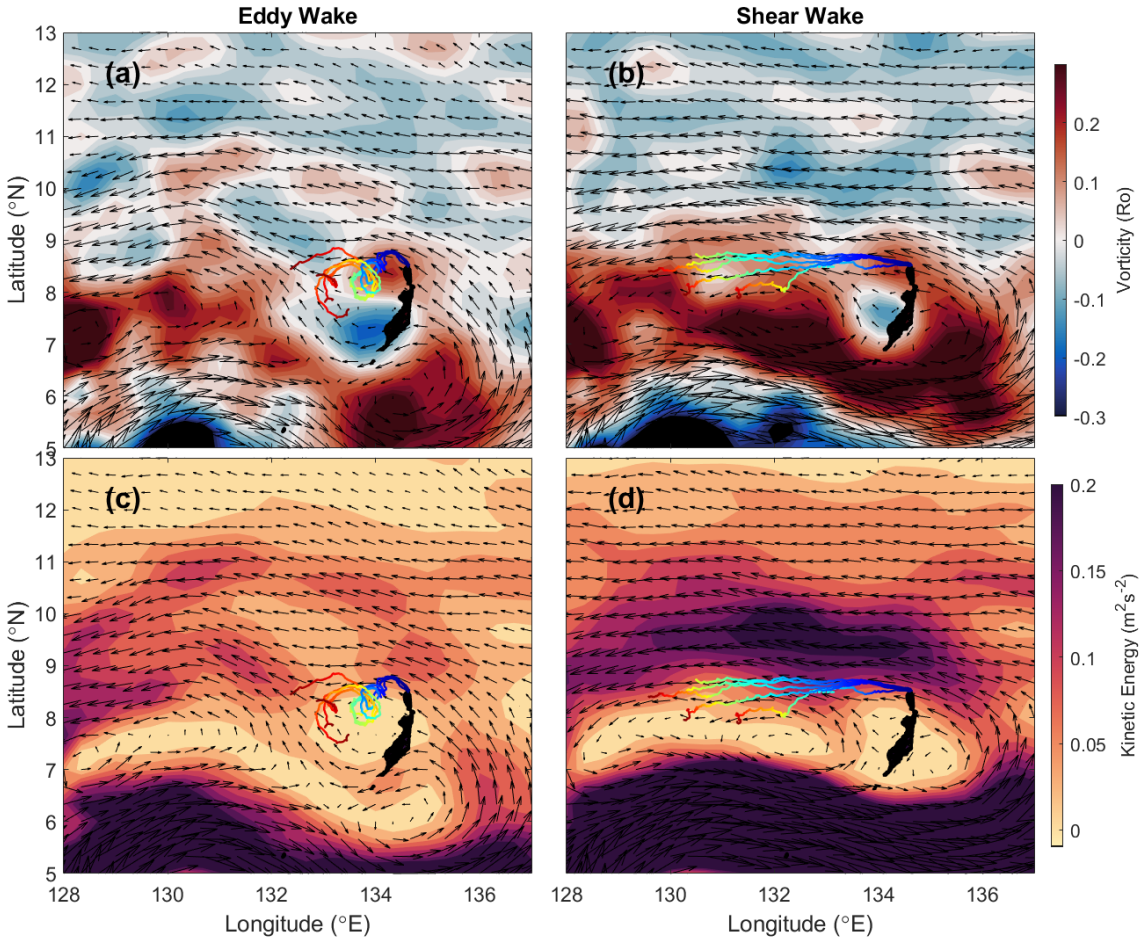

Figure 4.17: OSCAR Surface currents averaged over the first 20 deployment days of each drifter cluster entrained into (a,c) wake eddies and (b,d) free shear layers. Vorticity is contoured in (a,b), and kinetic energy in (c,d). Black quivers overlaid on all are corresponding surface current vectors.

Chapter 5

Conclusion

The work in this dissertation combines observations from underwater gliders, moorings, Lagrangian surface drifters and satellite data to characterize the wake generated by broadband flow past Palau, a $\sim$ 200 km long, steep-sided island in the deep tropical North Pacific Ocean. Our focus is the generation of vorticity and development of wake eddies around the north end of the island. Here, current variability is high due to complex regional geostrophic currents, energetic tides and strong inertial events. The wide range of sampling resolutions of each instrument is leveraged to understand the impact of this variability on the wake.

First, the low-frequency wake is characterized using gliders which sampled along two parallel 140-km meridional sections 40 km upstream and downstream of the island for more than two years. The data were objectively mapped to a regular grid in time and space with 10-m vertical, 30-km horizontal and 14-day temporal resolution. At smaller scales ($<$ 10 km), an array of moorings deployed at the north end of the island captured vorticity in the surface layer as it was injected into the interior for 11 months, with hourly resolution. Empirical Orthogonal Functions helped to isolate coherent structures in the flow, including submesoscale wake eddies. Finally, trajectories from 19 clusters of five surface drifters deployed in the same location as this array over two years captured the evolution of wake eddies and shear layers downstream. A simple

model of solid-body rotation helped to isolate the vorticity due to each and estimate the scale of wake eddies and their growth.

Together these observations suggest the Palau wake is generated when regional geostrophic currents are topographically blocked and forced to accelerate around the island. Cyclonic recirculation develops in the lee due to this offshore flow, and eddies form which are fed by vorticity generated within the boundary layer. Anticyclonic vorticity generated by strong flow through a narrow, deep channel across the island limits the length scale of the north wake to $\sim$ 80 km. Averaged over two years, wake vorticity at this scale reaches $0.3f$ near the surface, where flow is strongest. Here f is the local Coriolis frequency. This average likely contains contributions from submesoscale eddies O(10 km) as well as island-scale recirculation. Near the separation point, vorticity can exceed $\sim 6f$ during strong westward flow when strong submesoscale eddies are generated. The magnitude of wake vorticity is primarily driven by the low-frequency geostrophic current. However, the formation frequency of these wake eddies is strongly modulated by energetic tides and inertial oscillations. Thus, eddies likely do not shed at the natural Strouhal frequency of the island, as often assumed in wake studies. Close to the island, wake eddies have peak vorticity up to $8f$, scales between 10-40 km, and are in cyclogeostrophic balance. Downstream, eddies are entrained in island-scale meridional shear which controls their growth.

This thesis work characterized the vorticity around Palau at scales from 5-100 km, primarily in the intensified surface flow (0-100 m depth). Questions remain about the vorticity at finer scales, as well as the depth dependence of the wake. Concurrent studies have shown O(1 km) wake eddies generated around small topographic features with vorticity up to $50f$ (MacKinnon et al., 2019; Johnston et al., 2019). The relationship of these eddies to the submesoscale wake is unclear. Two plausible hypotheses are (1) they are unstable and decay, contributing to local diapycnal mixing, and (2) they propagate downstream, interacting with the submesoscale wake. Ongoing work with concurrent microstructure observations will help elucidate the stability of these eddies close to the topography (B. Wynne-Cattanach and A. Simpson, personal communication).

High-resolution numerical models of the flow around Palau may be useful in understanding their evolution downstream (Simmons et al., 2019). These eddies are strongly tilted in the vertical due to the sloping topography. Similar depth dependence was observed in this work. The island-scale recirculation is vertically tilted, and vorticity is weaker at depth (Chapters 1 and 2). It is likely that the subsurface wake differs substantially downstream, disconnected from the surface flow (Perfect et al., 2018). Subsurface observations far downstream of Palau are limited, so numerical models may be the best avenue to explore this variability further. However additional analysis of existing observations (glider surveys, moored ADCPs around the north end) can provide further insights into the depth-dependence of vorticity in the near-field.

References

Alpers, W., Brandt, P., Lazar, A., Dagorne, D., Sow, B., Faye, S., Hansen, M., Rubino, A., Poulain, P.-M., and Brehmer, P. (2013). A small-scale oceanic eddy off the coast of West Africa studied by multi-sensor satellite and surface drifter data. *Remote Sensing of Environment*, 129:132–143.

Andrade, I., Sangra, P., Hormazabal, S., and Correa-Ramirez, M. (2013). Island mass effect in the Juan Fernandez Archipelago (33°S), Southeastern Pacific. *Deep-Sea Research II*, 84:86–99.

Andres, M., Musgrave, R., Rudnick, D., Zeiden, K., Peacock, T., and Park, J.-H. (2020). On the predictability of sea surface height around Palau. *Journal of Physical Oceanography*, 50:3267–3294.

Aristegui, J. and Montero, M. F. (2005). Temporal and spatial changes in plankton respiration and biomass in the Canary Islands region: the effect of mesoscale variability. *Journal of Marine Systems*, 54:65–82.

Aristegui, J., Sangra, P., Hernandez-Leon, S., Canton, M., Hernandez-Guerra, A., and Kerling, J. (1994). Island induced eddies in the Canary islands. *Deep-Sea Research*, 41:1509–1525.

Barkley, R. A. (1972). Johnston Atoll's wake. *Journal of Marine Research*, 30:201–216.

Bearman, P. (1969). On vortex shedding from a circular cylinder in the critical Reynolds number regime. *Journal of Fluid Mechanics*, 37:577–585.

Bearman, P. (1984). Vortex shedding from oscillating bluff bodies. *Annual Review of Fluid Mechanics*, 16:195–222.

Blasius, H. (1908). The boundary layers in fluids with little friction. *Zeitschrift fur Mathematik und Physik*, 56:1–37.

Bonjean, F. and Lagerloef, G. (2002). Diagnostic model and analysis of the surface currents in the tropical Pacific Ocean. *Journal of Physical Oceanography*, 32:2938 – 2954.

Bowman, M., Dietrich, D., and Lin, C. (1996). Observations and modeling of mesoscale ocean circulation near a small island. *Coastal and Estuarine Studies*, 51:18–35.

Boyer, D. and Davies, P. (1982). Flow past a circular cylinder on a beta-plane. *Philosophical Transactions of the Royal Society of London A*, 306:533–556.

Bretherton, F., Davis, R., and Fandry, C. (1976). A technique for objective analysis and design of oceanographic experiments applied to MODE-73. *Deep-Sea Research*, 23:559–582.

Brown, G. and Roshko, A. (1974). On density effects and large structures in turbulent mixing layers. *Journal of Fluid Mechanics*, 64:775–816.

Caldeira, R. and Sangra, P. (2012a). Complex geophysical wake flows. *Ocean Dynamics*, 62:683–700.

Caldeira, R., Stenger, A., Couvelard, X., Araujo, I., Testor, P., and Lorenzo, A. (2014). Evolution of an oceanic anticyclone in the lee of Madeira Island: in situ and remote sensing survey. *Journal of Geophysical Research: Oceans*, 119:1195–1216.

Caldeira, R. M. A. and Sangra, P. (2012b). Complex geophysical wake flows: Madeira Archipelago case study. *Ocean Dynamics*, 62:683—700.

Caldiera, R., Marchesiello, P., Nezlin, N., DiGiacomo, P., and McWilliams, J. (2005). Island wakes in the Southern California bight. *Journal of Geophysical Research*, 110:C11012.

Callendar, W., Klymak, J., and Foreman, M. (2011). Tidal generation of large sub-mesoscale eddy dipoles. *Ocean Science*, 7:487–502.

Centurioni, L. (2018). *Observing the Oceans in Real Time*, chapter Drifter Technology and Impacts for Sea Surface Temperature, Sea-Level Pressure, and Ocean Circulation Studies. Springer, Cham.

Chang, M., Jan, S., Liu, C., and Cheng, Y. (2019). Observations of island wakes at high Rossby numbers: evolution of submesoscale vortices and free shear layers. *Journal of Physical Oceanography*, 49:2997–3016.

Chang, M., Tang, T., Ho, C., and Chao, S. (2013). Kuroshio-induced wake in the lee of Green Island off Taiwan. *Journal of Geophysical Research*, 118:1508–1519.

Chelton, D., DeSzoeke, R., and Schlax, M. (1998). Geographic variability of the first baroclinic Rossby radius of deformation. *Journal of Physical Oceanography*, 28:433–460.

Chelton, D., Schlax, M., and Samelson, R. (2011). Global observations of nonlinear mesoscale eddies. *Progress in Oceanography*, 91:167–216.

Cheng, Y., M.H.Chang, Ko, D., Jan, S., Andres, M., Kirincich, A., Yang, Y., and Tai, J. (2020). Submesoscale eddy and frontal instabilities in the Kuroshio interaction with a cape south of Taiwan. *Journal of Geophysical Research: Oceans*, 124.

D'Addezio, J., Jacobs, G., Yaremchuk, M., and Souopgui, I. (2020). Submesoscale eddy vertical covariances and dynamical constraints from high-resolution numerical simulations. *Journal of Physical Oceanography*, 4:1087–1115.

Davies, P., Besley, P., and Boyer, D. (1990). An experimental study of flow past a triangular cape in a linearly stratified fluid. *Dynamics of Atmospheres and Oceans*, 14:497–528.

Davies-Jones, R. (1993). Useful formulas for computing divergence, vorticity and their errors from three or more stations. *Monthly Weather Review*, 121:713–725.

Delandmeter, P., Lambrechts, J., Marmorino, G., Legat, V., Wolanski, E., Remacle, J.-F., Chen, W., and Deleersnijder, E. (2017). Submesoscale tidal eddies in the wake of coral islands and reefs: satellite data and numerical modelling. *Ocean Dynamics*, 67:897–913.

Dickey, T., Nencioli, F., Kuwahara, V., Leonard, C., Black, W., Rii, Y., Bidigare, R., and Zhang, Q. (2008). Physical and bio-optical observations of cyclones west of the island of Hawai'i. *Deep Sea Research II*, 55:1195–1217.

Dong, C., Liu, Y., Lumpkin, R., Lankhorst, M., Chen, D., McWilliams, J., and Guan, Y. (2011). A scheme to indentify loops from trajectories of oceanic surface drifters: an application to the Kuroshio Extension region. *Journal of Atmospheric and Oceanic Technology*, 28:1167 – 1176.

Dong, C. and McWilliams, J. (2007). A numerical study of island wakes in the Southern California Bight. *Continental Shelf Research*, 27:1233–1248.

Dong, C., McWilliams, J., and Shchepetkin, A. (2007). Island wakes in deep water. *Journal of Physical Oceanography*, 37:962–981.

ESR (2009). OSCAR third degree resolution ocean surface currents. Ver. 1. PO.DAAC. Dataset accessed 2018-08-22 at.

Farmer, D., Pawlowicz, R., and Jiang, R. (2002). Tilting separation flows: a mechanism for intense vertical mixing in the coastal ocean. *Dynamics of Atmospheres and Oceans*, 36:43–58.

Fischer, A., Weller, R., Rudnick, D., Eriksen, C., Lee, C., Brink, K., Fox, C., and Leben, R. (2002). Mesoscale eddies, coastal upwelling, and the upper-ocean heat budget in the Arabian Sea. *Deep-Sea Research II*, 49:2231–2264.

Henaff, M. L., Kourafalou, V., Dussurget, R., and Lumpkin, R. (2014). Cyclonic activity in the eastern Gulf of Mexico: characterization from along-track altimetry and in situ drifter trajectories. *Progress in Oceanography*, 120:120–138.

Herandez-Leon, S. (1991). Accumulation of mesozooplankton in a wake area as a causative mechanism of the "island-mass effect". *Marine Biology*, 109:141–147.

Heron, S., Metzger, E., and Skirving, W. (2006). Seasonal variations of the ocean surface circulation in the vicinity of Palau. *Journal of Oceanography*, 62:413–426.

Heywood, K., Barton, E., and Simpson, J. (1990). The effects of flow disturbance by an oceanic island. *Journal of Marine Research*, 48:55–73.

Heywood, K., Stevens, D., and Bigg, G. (1996). Eddy formation behind the tropical island of Aldabra. *Deep-Sea Research I*, 43:555–578.

Hormann, V., Centurioni, L., Mahadevan, A., Essink, S., D'Asaro, E., and Kumar, B. (2016). Variability of near-surface circulation and sea surface salinity observed from Lagrangian drifters in the Northern Bay of Bengal during the waning 2015 Southwest Monsoon. *Oceanography*, 29:124–133.

Hsin, Y. and Qiu, B. (2012). Seasonal fluctuations of the surface North Equatorial Countercurrent (NECC) across the Pacific basin. *Journal of Geophysical Research*, 117:C06001.

Hsu, P., Chang, M., Lin, C., Huang, S., and Ho, C. (2017). Investigation of the island-induced ocean vortex train of the Kuroshio Current using satellite imagery. *Remote Sensing of Environment*, 193:54–64.

Jimenez, B., Sangra, P., and Mason, E. (2008). A numerical study of the relative importance of wind and topographic forcing on oceanic eddy shedding by tall, deep water islands. *Ocean Modelling*, 22:146 – 157.

Johnston, T., MacKinnon, J., Colin, P., Jr., P. H., Lermusiaux, P., Lucas, A., Merrifield, M., Merrifield, S., Mirabito, C., Nash, J., Ou, C., Siegelman, M., Terrill, E., and Waterhouse, A. (2019). Energy and momentum lost to wake eddies and lee waves generated by the North Equatorial Current and tidal flows at Peleliu, Palau. *Oceanography*, 32(4):110–125.

Kashino, Y., Espana, N., Syamsudin, F., Richards, K., Jensen, T., Dutrieux, P., and Ishida, A. (2008). Observations of the North Equatorial Current, Mindanao Current, and Kuroshio Current system during the 2006/07 El Niño and 2007/08 La Niño. *Journal of Oceanography*, 65:325–333.

Kundu, P. and Cohen, I. (1990). *Fluid Mechanics 4th Ed.* Elsevier, San Diego, California.

LaCasce, J. (2008). Statistics from Lagrangian observations. *Progress in Oceanography*, 77:1–29.

Ledwell, J. R., Watson, A. J., and Law, C. S. (1998). Mixing of a tracer in the pycnocline. *Journal of Geophysical Research*, 103:21499–21529.

Li, J., Zhang, R., and Jin, B. (2011). Eddy characteristics in the northern South China Sea as inferred from Lagrangian drifter data. *Ocean Science*, 7:661–669.

Lilly, J. and Perez-Brunius, P. (2020). Extracting statistically significant eddy signals from large Lagrangian datasets using wavelet ridge analysis, with application to the Gulf of Mexico. *Nonlinear Processes in Geophysics*.

Lilly, J., Scott, R., and Olhede, S. (2011). Extracting waves and vortices from Lagrangian trajectories. *Geophysical Research Letters*, 38.

Lim, Y. (2017). The 2015/16 El Niño event in context of the MERRA-2 reanalysis: A comparison of the Tropical Pacific with 1982/83 and 1997/98. *Journal of Climate*, 30:4819–4842.

MacKinnon, J., Alford, M., Voet, G., Zeiden, K., Johnston, T., and Siegelman, M. (2019). Eddy wake generation from broadband currents near Palau. *Journal of Geophysical Research Oceans*, 124:4891–4903.

Martin, A. and Richards, K. J. (2001). Mechanisms for vertical nutrient transport within a North Atlantic mesoscale eddy. *Deep-Sea Research II*, 48:757–773.

Merrifield, S., Colin, P., Cook, T., Garcia-Moreno, C., MacKinnon, J., Otero, M., Schramek, T., Siegelman, M., Simmons, H., and Terrill, E. (2019). Island wakes observed from high-frequency current mapping radar. *Oceanography*, 32:92–101.

Mittelstaedt, E. (1987). Cyclonic cold-core eddy in the eastern North Atlantic. i. physical description. *Marine Ecology*, 39:145–152.

Molemaker, M., McWilliams, J., and Dewar, W. (2015). Submesoscale instability and generation of mesoscale anticyclones near a separation of the California Undercurrent. *Journal of Physical Oceanography*, 45:614–629.

Molinari, R. and Kirwan, A. (1975). Calculations of differential kinematic properties from lagrangian observations in the Western Caribbean Sea. *Journal of Physical Oceanography*, 5:483 – 491.

Monismith, S., Barkdull, M., Nunome, Y., and Mitarai, S. (2018). Transport between Palau and the Eastern Coral Triangle. *Geophysical Research Letters*, 45:4974–4981.

Munk, W., Armi, L., Fischer, K., and Zachariasen, F. (2000). Spirals on the sea. *Proceedings of the Royal Society of London A*, 456:1217–1280.

Musgrave, R., Flierl, G., and Peacock, T. (2018). The generation of Rossby waves and wake eddies by small islands. *Journal of Marine Research*, 46:1137–1155.

Neill, S. and Elliott, A. (2004). Observations and simulations of an unsteady island wake in the Firth of Forth, Scotland. *Ocean Dynamics*, 54:324–332.

Okubo, A. (1970). Horizontal dispersion of floatable particles in the vicinity of velocity singularities such as convergences. *Deep-sea Research*, 17:445–454.

Okubo, A. and Ebbesmeyer, C. (1976). Determination of vorticity, divergence, and deformation rates from analysis of drogue observations. *Deep-Sea Research*, 23:349–352.

Olson, D. (1991). Rings in the ocean. *Annual Review of Earth and Planetary Science*, 19:281–311.

Pattiaratchi, C., James, A., and Collins, M. (1986). Island wakes and headland eddies: A comparison between remotely sensed data and laboratory studies. *Journal of Geophysical Research*, 92:783–794.

Pawlak, G., MacCready, P., Edwards, K., and McCabe, R. (2003). Observations on the evolution of tidal vorticity at a stratified deep water headland. *Geophysical Research Letters*, 30.

Perfect, B., Kumar, N., and Riley, J. (2018). Vortex structures in the wake of an idealized seamount in rotating, stratified flow. *Geophysical Research Letters*, 45.

Pinkel, R. (1984). Doppler sonar observations of internal waves: The wavenumber-frequency spectrum. *Journal of Physical Oceanography*, 14:1249–1270.

Qiu, B. and Lukas, R. (1996). Seasonal and interannual variability of the North Equatorial Current, the Mindanao Current, and the Kuroshio along the Pacific western boundary. *Journal of Geophysical Research*, 101:12315–12330.

Qiu, B., Rudnick, D. L., Chen, S., and Kashino, Y. (2013). Quasi-stationary North Equatorial Undercurrent jets across the tropical North Pacific Ocean. *Geophysical Research Letters*, 40:1–5.

Rainville, L. and Pinkel, R. (2005). Propagation of low-mode internal waves through the ocean. *Journal of Physical Oceanography*, 36:1220–1236.

Roshko, A. (1954). On the development of turbulent wakes from vortex streets. Report 1191, National Advisory Committee for Aeronautics.

Rudnick, D. (2001). On the skewness of vorticity in the upper ocean. *Geophysical Research Letters*, 28:2045–2048.

Rudnick, D. and Davis, R. (1988). Frontogenesis in mixed layers. *Journal of Physical Oceanography*, 18:434–457.

Rudnick, D., Gopalakrishnan, G., and Cornuelle, B. (2015). Cyclonic eddies in the Gulf of Mexico: observations by underwater gliders and simulations by numerical model. *Journal of Physical Oceanography*, 45:313 – 326.

Rudnick, D., J.T.Sherman, and Wu, A. (2018). Depth-average velocity from Spray underwater gliders. *Journal of Atmospheric and Oceanic Technology*, 35:1665–1673.

Rudnick, D. and Weller, R. (1993). Observations of superiniertial and near-inertial wind driven flow. *Journal of Physical Oceanography*, 23:2351–2359.

Rudnick, D., Zeiden, K., Ou, C., Johnston, T., MacKinnon, J., Alford, M., and Voet, G. (2019). Understanding vorticity caused by flow passing an island. *Oceanography*, 32:66–73.

Rudnick, D. L. and Cole, S. T. (2011). On sampling the ocean using underwater gliders. *Journal of Geophysical Research: Oceans*, 116:C08010.

Sangra, P., Auladell, M., Marrero-Diaz, A., Pelegri, J., Fraile-Nuez, E., Rodriguez-Santana, A., Martin, J., Mason, E., and Hernandez-Guerra, A. (2007). On the nature of oceanic eddies shed by the Island of Gran Canaria. *Deep-Sea Research I*, 54:687–709.

Schönau, M. and Rudnick, D. (2015). Glider observations of the North Equatorial Current in the western Tropical Pacific. *Journal of Geophysical Research: Oceans*, 120:3586–3605.

Schönau, M. and Rudnick, D. (2017). Mindanao Current and Undercurrent: thermohaline structure and transport from repeat glider observations. *Journal of Physical Oceanography*, 47:2055–2075.

Shakespeare, C. (2016). Curved density fronts: Cyclogeostrophic adjustment and frontogenesis. *Journal of Physical Oceanography*, 46:3193–3207.

Shcherbina, A. Y., D'Asaro, E. A., Lee, C. M., Klymak, J. M., Molemaker, M. J., and McWilliams, J. C. (2013). Statistics of vertical vorticity, divergence, and strain in a developed submesoscale turbulence field. *Geophysical Research Letters*, 40:4706–4711.

Sherman, J., Davis, R. E., Owens, W. B., and Valdes, J. (2001). The autonomous underwater glider "Spray". *IEEE Journal of Oceanic Engineering*, 26:437–446.

Signell, R. and Geyer, W. (1991). Transient eddy formation around headlands. *Journal of Geophysical Research*, 96:2561–2575.

Simmons, H., Powell, B., Merrifield, S., Zedler, S., and Colin, P. (2019). Dynamical downscaling of equatorial flow response to Palau. *Oceanography*, 32:84–91.

Smith, W. and Sandwell, D. (1997). Global seafloor topography from satellite altimetry and ship depth soundings: evidence for stochastic reheating of the oceanic lithosphere. *Science*, 277:1956–1962.

Teague, W., Hwang, P., Jacobs, G., Book, J., and Perkins, H. (2005). Transport variability across the Korea/Tsushima Strait and the Tsushima Island wake. *Deep-sea Research II*, 52:1784–1801.

Teague, W., Jacobs, G., Perkins, H., and Book, J. (2002). Low-frequency current observations in the Korea/Tsushima Strait. *Journal of Physical Oceanography*, 32:1621–1641.

Teinturier, S., Stegner, A., Didelle, H., and Viboud, S. (2010). Small-scale instabilities of an island wake flow in a rotating shallow-water layer. *Dynamics of Atmospheres and Oceans*, 49:1–24.

Todd, R., Rudnick, D., Sherman, J., Owens, W., and George, L. (2017). Absolute velocity estimates from autonomous underwater gliders equipped with doppler current profilers. *Journal of Atmospheric and Oceanic Technology*, 34:309–333.

Vallis, G. (2006). *Atmospheric and oceanic fluid dynamics*. Cambridge University Press, Cambridge, UK.

Voet, G., Alford, M., and MacKinnon, J. (2020). Topographic form drag on tides and low-frequency flow: observations of nonlinear lee waves over a tall submarine ridge near Palau. *Journal of Physical Oceanography*, 50:1489–1507.

von Karman, T. (1912). On the mechanism of resistance produced by moving body in liquid (in German). *Nachrichtungen des Gelleschaft Wissenschaft, Goettingen*, pages 509–517.

Walker, J. B. A. and Stewartson, K. (1972). The flow past a circular cylinder in a rotating frame. *Zeitschrift fur Angewandte Mathematik und Physik*, 23:745 – 752.

Weiss, J. (1991). The dynamics of enstrophy transfer in two-dimensional hydrodynamics. *Physica D*, 48:273–294.

White, W. (1973). An oceanic wake in the equatorial undercurrent downstream from the Galapagos archipelago. *Journal of Physical Oceanography*, 3:156–161.

Whitt, D. B. and Thomas, L. N. (2012). Near-inertial waves in strongly baroclinic currents. *Journal of Physical Oceanography*, 43:706–725.

Wijesekera, H., Wesson, J., Wang, D., Teague, W., and Hallock, Z. (2020). Obesrvations of flow separation and mixing around the Northern Palau Island/ridge. *Journal of Physical Oceanography*, pages 2529–2559.

Wolanski, E., Colin, P., Naithani, J., Deleersnijder, E., and Golbuu, Y. (2004). Large amplitude, leaky, island-generated, internal waves around Palau, Micronesia. *Estuarine, Coastal and Shelf Science*, 60:705–716.

Wolanski, E., Imberger, J., and Heron, M. (1984). Island wakes in shallow coastal waters. *Journal of Geophysical Research*, 89:10553–10569.

Xie, S. P., Liu, W. T., Liu, Q., and Nonaka, M. (2001). Far-reaching effects of the Hawaiian islands on the Pacific ocean-atmosphere system. *Science*, 292:2057– 2060.

Yang, G., Wang, F., Li, Y., and Lin, P. (2013). Mesoscale eddies in the northwestern subtropical Pacific Ocean: statistical characteristics and three-dimensional structures. *Journal of Geophysical Research*, 118:1906–1925.

Zdravkovich, M. (2000). *Flow Around Circular Cylinders*. Oxford University Press, Oxford, New York.

Zeiden, K., MacKinnon, J., Alford, M., Rudnick, D., Voet, G., and Wijesekera, H. (2021). Broadband submesoscale vorticity generated by flow around an island. *Journal of Physical Oceanography*.

Zeiden, K., Rudnick, D., and MacKinnon, J. (2019). Glider observations of a mesoscale oceanic island wake. *Journal of Physical Oceanography*, 49:2217 – 2235.

Zhao, J., Li, Y., and Wang, F. (2013). Dynamical responses of the west Pacific North Equatorial Countercurrent (NECC) system to El Niño events. *Journal of Geophysical Research: Oceans*, 118:2828–2844.

Zheng, Q., Lin, H., Meng, J., Hu, X., Song, Y., Zhang, Y., and Li, C. (2008). Sub-mesoscale ocean vortex trains in the Luzon Strait. *Journal of Geophysical Research*, 113.